

# Occupation dynamics of self-assembled quantum dots and deep level traps

INAUGURAL-DISSERTATION

zur Erlangung des Doktorgrades der  
Mathematisch-Naturwissenschaftlichen Fakultät der  
Heinrich-Heine-Universität Düsseldorf

vorgelegt von:

**Lukas Leonard Berg**

aus Köln

Düsseldorf, Juli 2024

aus dem Institut für Experimentelle Physik der kondensierten Materie der  
Heinrich-Heine-Universität Düsseldorf

Gedruckt mit der Genehmigung der  
Mathematisch-Naturwissenschaftlichen Fakultät der  
Heinrich-Heine-Universität Düsseldorf

*Berichtersteller:*

1. Prof. Dr. Thomas Heinzl
2. Prof. Dr. Jürgen Horbach

Tag der mündlichen Prüfung: 29.08.2024

# Abstract

This thesis focuses on the occupation dynamics of self-assembled quantum dots (SAQDs) and deep level traps. SAQDs are nanoscale crystalline structures with dimensions small enough to exhibit only a discrete density of states for charge carriers. Embedded in a host crystal, these energetic states can lie within the forbidden bandgap. The free charge carriers of the crystal can interact with these discrete states, they can be captured, stored and emitted. Placing these SAQDs in a Schottky junction allows for observation of their occupation by the junction's capacitance and for precise control over the electric field and charge carrier density at the SAQDs position. Capacitance transient spectroscopy was used in this thesis to isolate the electron capture and emission rates.

Within this thesis three research projects were conducted. The first project investigates the capture of electrons into SAQDs that are far from their reservoirs ( $> 100$  nm). Capture rates were extracted from the capacitance transients as a function of the electric field, the temperature and the applied magnetic field. The studies identified the back contact of the Schottky junction as the dominant electron source. A model was developed to describe electron diffusion from the back contact to the SAQDs position. Capture by tunneling is possible for small barriers, as identified experimentally. Furthermore, the extracted capture and emission rates were used to model the hysteretic capacitance voltage characteristics quantitatively. In the second project an electrostatic coupling between two layers of SAQDs at a distance of 200 nm is observed. The coupling manifests itself by a modulation of the capture and emission rates of one layer based on the electric field generated by the respective other layer. A model based on rate equations explains the observations quantitatively.

Defects in the crystal lattice of a semiconductor can also modify their surrounding potential to discrete energetic states within the bandgap, the deep level traps. The third project introduces the deep level transient photocapacitance spectroscopy, a novel technique for extracting parameters of deep level traps from their temperature dependent photocapacitance transients. The oxygen vacancy in rutile titanium dioxide acted as a platform, a rolled-up nanomembrane, used as electrode, allowed a high illumination rate.

# Zusammenfassung

Diese Arbeit befasst sich mit der Besetzungsdynamik von selbstorganisierten Quantenpunkten (SAQDs) und tiefen Störstellen. SAQDs sind kristalline Strukturen mit Abmessungen typischerweise im Nanometerbereich, die klein genug sind um nur diskrete Zustandsdichten für freie Ladungsträger aufzuweisen. Eingebettet in einen Wirtskristall können diese energetischen Zustände innerhalb der sonst verbotenen Bandlücke liegen. Die freien Ladungsträger des Kristalls können mit diesen diskreten Zuständen interagieren, sie können eingefangen, gespeichert und wieder emittiert werden. Die Platzierung dieser SAQDs in einer Schottky-Diode ermöglicht die Beobachtung ihrer Besetzung durch die Kapazität der Diode sowie die präzise Kontrolle des elektrischen Feldes und der Dichte der freien Ladungsträgerdichte am Ort der SAQDs. Kapazitive Transientenspektroskopie wurde in dieser Arbeit verwendet, um die Einfang- und Emissionsraten von Elektronen in oder aus den SAQDs oder tiefen Störstellen zu isolieren.

Im Rahmen dieser Arbeit wurden drei Forschungsprojekte durchgeführt. Das erste Projekt untersucht den Einfang von Elektronen in SAQDs, welche weit von ihrem Reservoir entfernt sind ( $> 100$  nm). Die Einfangtransienten wurden aus den Kapazitätstransienten als Funktion des elektrischen Feldes, der Temperatur und des angelegten Magnetfeldes extrahiert. Die Untersuchungen ergaben, dass der Rückkontakt der Schottky-Diode die dominierende Elektronenquelle ist. Es wurde ein Modell entwickelt, welches den Einfang über Elektronendiffusion aus dem Rückkontakt zur SAQDs Position beschreibt. Der Einfang über Tunneln ist bei kleinen Barrieren möglich, wie experimentell gezeigt wurde. Darüber hinaus wurden die extrahierten Einfang- und Emissionsraten verwendet um die hysteretischen Kapazitätseigenschaften in Abhängigkeit der Spannung quantitativ zu modellieren.

Im zweiten Projekt wird eine elektrostatische Kopplung zwischen zwei SAQDs-Schichten in einem Abstand von 200 nm beobachtet. Die Kopplung äußert sich in einer Modulation der Einfang- und Emissionsraten einer Schicht in Abhängigkeit vom elektrischen Feld, welches durch die Ladung in der jeweils anderen Schicht erzeugt wird. Ein auf Ratengleichungen basierendes Modell beschreibt die Beobachtungen quantitativ.

Defekte im Kristallgitter eines Halbleiters können auch ebenfalls das Potential in ihrer Umgebung so verändern dass sie diskrete Zustände innerhalb der Bandlücke, den tiefen Störstellen, aufweisen. Das dritte Projekt stellt die "deep level transient photocapacitance spectroscopy" vor, eine neue Methode um Parameter von tiefen Störstellen aus ihren temperaturabhängigen Photokapazitätstransienten zu extrahieren. Die Sauerstoff-Fehlstelle in rutilem Titandioxid diente als Plattform, eine aufgerollte Nanomembran wurde als Elektrode verwendet um eine hohe Beleuchtungsrate zu gewährleisten.



# Eidesstattliche Versicherung

Ich versichere an Eides Statt, dass die Dissertation von mir selbständig und ohne unzulässige fremde Hilfe unter Beachtung der „Grundsätze zur Sicherung guter wissenschaftlicher Praxis an der Heinrich-Heine-Universität Düsseldorf“ erstellt worden ist.

---

Ort, Datum

---

Lukas Leonard Berg



---

# Contents

<b>Introduction</b>	<b>1</b>
<b>1. Fundamental concepts</b>	<b>5</b>
1.1. Self-assembled quantum dots . . . . .	5
1.1.1. Growth . . . . .	6
1.1.2. Energy spectra . . . . .	8
1.2. Crystal defects . . . . .	11
1.2.1. Point defects . . . . .	11
1.2.2. Oxygen vacancy of titanium dioxide . . . . .	13
1.3. Charge carrier dynamics . . . . .	14
1.3.1. Capture . . . . .	14
1.3.2. Thermal emission . . . . .	15
1.3.3. Tunnel emission . . . . .	16
1.3.4. Thermally activated tunneling . . . . .	17
1.3.5. Optical emission . . . . .	17
1.4. Schottky junction . . . . .	18
1.4.1. Current voltage characteristics . . . . .	20
1.4.2. Capacitance voltage characteristics . . . . .	20
1.4.3. Capacitance transients . . . . .	21
<b>2. Experimental techniques</b>	<b>23</b>
2.1. Capacitance transients recording . . . . .	23
2.2. Samples . . . . .	25
2.2.1. Single layer SAQDs sample . . . . .	25
2.2.2. Double layer SAQDs sample . . . . .	27
2.2.3. Titanium dioxide sample . . . . .	28
2.3. Sample preparation . . . . .	30
2.4. Cryogenic setup . . . . .	31
2.4.1. Linkam HFS 600 cryostat . . . . .	31
2.4.2. Liquid nitrogen bath . . . . .	33
2.4.3. Dilution refrigerator . . . . .	33
<b>3. Deep level transient spectroscopy</b>	<b>35</b>
3.1. Work principle . . . . .	36
3.2. Boxcar weighting function . . . . .	36
3.3. Lock-in weighting function . . . . .	37

---

<b>4. Capture dynamics of self-assembled quantum dots far from equilibrium</b>	<b>39</b>
4.1. Paper I . . . . .	40
4.2. Paper II . . . . .	53
<b>5. Electrostatic inter-layer coupling between self-assembled quantum dots</b>	<b>67</b>
5.1. Paper III . . . . .	68
<b>6. Deep level transient photocapacitance spectroscopy</b>	<b>81</b>
6.1. Paper IV . . . . .	82
<b>7. Conclusion and outlook</b>	<b>95</b>
<b>A. Growth protocol for sample #14691</b>	<b>97</b>
<b>B. Growth protocol for sample #15070</b>	<b>99</b>
<b>Bibliography</b>	<b>103</b>
<b>Danksagung</b>	<b>115</b>

---

---

# Introduction

Self-assembled quantum dots (SAQDs) are material structures capable of localising free charge carriers into zero dimensional energetic states [1, 2]. Formed through epitaxial growth by combining suitable materials, these quantum dots have dimensions of the order of the de-Broglie wavelength, giving rise to discrete energetic states. Despite containing thousands of atoms and a confinement potential of different shape compared to a singular atom, SAQDs possess an atomic-like energetic spectrum, earning them the designation *artificial atoms*, despite smaller energetic spacings [3, 4]. In fundamental research the similarities are exploited for experiments under unattainable conditions with real atoms [5–7]. In applications SAQDs have proven valuable in the optoelectronic fields of light emitting diodes (LEDs) [8] and lasers [9]. The quantum properties of the SAQDs can be utilized for advanced applications like the entangled photon LED [10] or on-demand single photon sources [7, 11]. SAQDs have found further applications in classical electrical components like memory cells [12–14] or memristors [15]. Furthermore, they are being explored for the use in quantum computation, as potential candidates to host the quantum bits, experimentally realised with spins [16, 17] and excitons [18].

An in-depth understanding of the capture and emission processes of charge carriers is crucial for enhancing the performance and efficiency of these applications. Several experimental techniques have been established to study the occupation dynamics of these quantum dots, providing valuable insights. Commonly used techniques include photoluminescence spectroscopy [19, 20], which probes for a shift in the resonance frequency of an electron hole pair inside a dot when additional charge is stored inside the dot. They include also transconductance spectroscopy [21, 22], where charge in quantum dots influence the conductance of a nearby channel, or capacitance-voltage spectroscopy [23–25]. The latter relies on charge carriers elastically tunneling between the energetic states of the quantum dot and free charge carriers at the Fermi level of a nearby reservoir, to name a few.

Deep level transient spectroscopy (DLTS) [26] is employed in this thesis to investigate the time-dependent occupation dynamics of the dots. Compared to other experimental techniques listed above it has the advantage that it does not rely on a nearby conductive channel from which electrons can elastically tunnel back and forth. The SAQDs are embedded in a *pn* or Schottky junction, the occupation dynamics is monitored by the capacitance of the junction, with a typical distance of hundreds of nm between the SAQDs and the edge of the depletion region. This allows to prepare experimental conditions where solely the capture or emission of

---

charge carriers is the dominant process [27–37].

This thesis presents three projects regarding the occupation dynamics of SAQDs and deep level traps. The first project investigates the capture dynamics of electrons into SAQDs that are in large distances ( $>100$  nm) from their reservoirs. *Paper I* [13] and *Paper II* [38] result from this project. The second project explores the interactions between two layers of SAQDs, discovering a novel type of interaction arising from the electrostatic properties and the occupation dynamics of the dot layers, as seen in *Paper III*. In the third project, summarised in *Paper IV* [39], the occupation dynamics of deep level traps in response to illumination is analysed. Based on this analysis, the technique of deep level transient photocapacitance spectroscopy (DLTPCS) is developed to extract the parameters of the deep level traps from the photocapacitance transients.

In *Paper I* [13] isothermal DLTS measurements at selected temperatures are applied to a Schottky junction containing a single layer of SAQDs in large distance from its reservoir, as commonly found in applications in the fields of optoelectronics [8, 40] or information storage units [41]. Measurements on the capture dynamics of electrons into such SAQDs structures had so far been mainly limited to methods relying on a nearby conductive reservoir [24, 42], indirect observation, were emission processes as a function of preceding capture is observed [35, 43], or optical methods [44–46]. A direct measurement of the electron capture had been carried out isothermal at a temperature of 77 K [47]. In *Paper I* electronic measurements of the capture rates at cryogenic temperatures as low as  $T = 7$  K are reported. It was found that the capture rates increased with increasing bias voltage, while a comparative analysis between different temperatures indicated an apparent thermally activated origin. In the emission spectra tunneling from the  $s$ -,  $p$ - and  $d$ - states could be observed. A fit with empirical rate equations was established to model this behaviour. The results of this fit were further used to model the well known capacitance voltage hysteresis of the junction [41, 48–52]. Such a hysteresis can be used as an information storage, where the charge in the quantum dots is used as bit. The modelled time- and bias voltage-dependent occupancy agrees well with observed hysteric capacitance voltage traces.

*Paper II* [38] further explores the mechanisms of capture into the SAQDs. Additional experiments on the sample studied in *Paper I* were conducted in a magnetic field. A detailed analysis of the data used in *Paper I* identify the back contact as the dominant source of the electrons. The apparent thermally activated character of the capture rates can be explained by diffusion of electrons from the back contact into the depletion region of the junction where the dots are located. Under specific conditions tunnelling could be observed, which could be achieved by sufficiently low temperatures or capture in partially filled quantum dots. The evolution of the tunneling current can be investigated with the help of an applied magnetic field that shifted the energy levels inside the SAQDs.

---

Many of the devices that utilise the properties of SAQDs employ multiple layers of SAQDs to enhance their performance, such as in LEDs [53], quantum dot lasers [54] or solar cells [55]. A detailed understanding of the interactions between the layers is thus essential for optimising the devices functionality. In correlated growth, the nucleation side of the quantum dots depends on the layer beneath it [56, 57], relevant up to distances of approximately 50 nm. For inter-layer distances below 10 nm the energetic levels of the dots can couple quantum mechanically, leading to the formation of *artificial molecules* [58–60], relevant for quantum computation [18, 61]. An electrostatic coupling of adjacent SAQDs layers had been reported for a distance of 20 nm [62]. In *Paper III* an electrostatic coupling between two layers of SAQDs at a large distance of 200 nm is reported, a distance commonly found in devices, but large enough that the interactions like tunnel or correlated growth can be excluded. The interaction is driven by the electrostatic properties of the layers and their interdependence on the capture and emission rates of the respective other layer of SAQDs. Isothermal DLTS was conducted at a temperature of  $T = 77\text{ K}$ . The observed effects were modelled using a system of rate equations, similar to the ones reported in Refs. [13, 47] with the extension of the interaction mechanism, successfully reproducing the data.

Crytal defects can also introduce additional energetic states in the semiconductor bandgap. These are known as deep level traps. In *Paper IV* [39] the occupation dynamics of deep level traps are used to develop the deep level transient photocapacitance spectroscopy (DLTPCS) [39]. This novel measurement technique extracts parameters of deep level traps from photocapacitance transients. In particular, compared to other photocapacitive methods [63, 64], it allows for extracting the capture cross section by an optical method as well as correctly determining the traps parameter under significant recapture [65]. Rutile titanium dioxide ( $\text{TiO}_2$ ), whose oxygen vacancies create deep level traps [66–68], served as a platform to develop this technique. A *rolled up nanomembrane* (rNM) [69–72] made from gold (Au) was used as an electrical contact to ensure a high illumination of the oxide [73]. Temperature dependent capacitance transients were analysed using a least-square fit to a system of rate equations, yielding valuable information on the binding energy, the capture cross section, the optical emission rate and the apparent thermal activation energy for the capture process. The resulting data showed good agreement with the data obtained through conventional DLTS.

This thesis is structured as follows: Chapter 1 discusses the relevant physics underlying this research, including the growth and energetic properties of self-assembled quantum dots and deep level traps, as well as the formation of Schottky junctions. Chapter 2 provides a detailed description of the samples used in this thesis and the measurement setup employed. Chapter 3 introduces the deep level transient spectroscopy, the primary investigation tool in this thesis. The four papers are included in the chapters 4 to 6. The thesis concludes in chapter 7 with a summary of the main findings and an outlook onto possible future related research projects.





---

# Chapter 1

## Fundamental concepts

### 1.1 Self-assembled quantum dots

Quantum dots are conducting islands of nanoscale size that can confine electric charge carriers in all three spatial dimensions below their de-Broglie wavelength. This confinement results in the discretisation of available energetic states for the charge carriers, in good proximity to the ones in atoms, which has led to them being labeled *artificial atoms*. However, quantum dots differ from single atoms in terms of their size and potential shape. While the potential confinement in atoms is created by a charged nucleus, the potential confinement in quantum dots is generated by applied bias voltages on metallic gate voltages or offsets in the energetic bands structure, depending on the realisation method. Quantum dots can consist of thousands of atoms resulting in a smaller energetic level spacing compared to singular atoms. This property makes quantum dots an optimal platform for fundamental research under conditions unachievable with real atoms [74, 75].

The de-Broglie wavelength for electrons at the Fermi level of a crystal, often called *Fermi wavelength*  $\lambda_F$ , is a function of dimensionality and charge carrier density  $n$ . In the three-dimensional case it reads [75]

$$\lambda_F = 2^{3/2} \left( \frac{\pi}{3n} \right)^{1/3}. \quad (1.1)$$

For typical semiconductor materials the Fermi wavelength is of the order of ten to hundreds of nanometers. Hence, semiconductors provide an optimal platform for the realisation of quantum dots. Over the last few decades numerous variations of quantum dots have been developed, each with unique properties and applications. Typical examples of materials for *colloidal quantum dots* are CdSe [76] and graphene [77]. The synthesis of these materials in a solution allows for a mass production as well as precise control over their size, shape and chemical attachments [78]. Applications of these dots are found in the fields of photocatalysis [79] to biomedical applications where they can serve as biomarkers in living cells [80].

A quantum dot can also be created by electrical gates over a *2 dimensional electron gas* formed beneath the surface of a semiconductor heterostructure. The use of electrical gates allows for dynamic tuning of the confinement potential, enabling

---

precise control over the quantum dots' shape and depth. This is particularly useful for studying charge transport through single and multiple quantum dots [81–83], as well as adjusting the energetic states of multiple quantum dots to generate qubits for quantum computing [84].

Another significant method for creating quantum dots is by *self assembly* [1, 2]. The epitaxial growth of certain semiconductor materials can result in the formation of small three-dimensional islands, that can be electronically accessible once overgrown and contacted. Their growth and energetic states are described below.

### 1.1.1 Growth

The InAs SAQDs used in this thesis were grown by molecular beam epitaxy (MBE), a high purity growth technique for semiconductor materials [85]. Effusion cells containing different materials create directed molecular beams that are pointed at a substrate crystal. On the surface, these atomic species can form new layers of the substrate crystal or new material combinations. This capability allows to produce semiconductor material combinations as well as the embedding of precise doping profiles. The MBE process is conducted under ultra-high vacuum conditions to avoid the incorporation of unwanted foreign atoms into the crystal structure. During the growth process the substrate crystal is rotated to balance inhomogeneous evaporation profiles from the effusion cells. Heating units allow for regulation of the substrate temperature during deposition, an important parameter for the kinetics of the adatoms and the surface interactions.

The growth of a semiconductor material on top of a different one leads to strain if the lattice constants of the materials do not match. Depending on the surface free energy, the thin film can grow in three different modes, an illustration of the growth modes can be seen in figure 1.1. The relevant energies are thereby the surface free energy at the epilayer-vacuum interface  $\gamma_e$ , the epilayer-substrate interface  $\gamma_i$  and substrate-vacuum interface  $\gamma_s$  [86]. The growth of the epilayer follows the minimization of the total free surface energy.

When the sum  $\gamma_e + \gamma_i < \gamma_s$ , it is energetically favorable for the material on the crystal surface to cover as much of the substrate surface as possible. This is referred to as the *Frank-van der Merwe* growth mode [87]. The epilayer grows in a successive, incremental manner, completing a full crystal layer before forming a new, incomplete layer.

Opposing the Frank-van der Merve mode is the *Volmer-Weber* growth mode [88], which occurs when  $\gamma_e + \gamma_i > \gamma_s$ , the epilayer reduces its energy by formation of droplets on the crystal surface. The droplets are discrete and self-assembled and can exhibit size distributions small enough to form quantum dots. An example of quantum dots grown under this mode is InAs on GaP [89].

The third growth mode is the *Stranski-Krastanov* growth mode [90]. With increasing thickness of the epilayer the strain energy is increased until it is released by the formation of three dimensional islands. During the initial layers, the material of the epilayer fully covers the substrate, forming the *wetting layer*. This resembles the layer-over-layer or Frank-van der Merve growth. The strain increases with each layer. Above a critical thickness it is energetically favorable to release this strain

by the formation of three dimensional islands. This transition from two to three dimensions is frequently referred to as the nucleation process.

On perfectly flat surfaces the nucleation of quantum dots is a statistical process [91], however on non-ideal surfaces step edges are the preferred nucleation sites [92, 93]. High uniformity of quantum dot size distribution can be achieved with variations of only 10 % [1]. This is due to the *Ostwald ripening*, whereby the large quantum dots grow at the expense of the smaller ones [86, 94]. Parameters such as temperature, material flux or strain significantly influence the density of the quantum dots as well as their shape [95]. The quantum dots were nucleated and homogenised without external influence, which is why they are referred to as self-assembled.

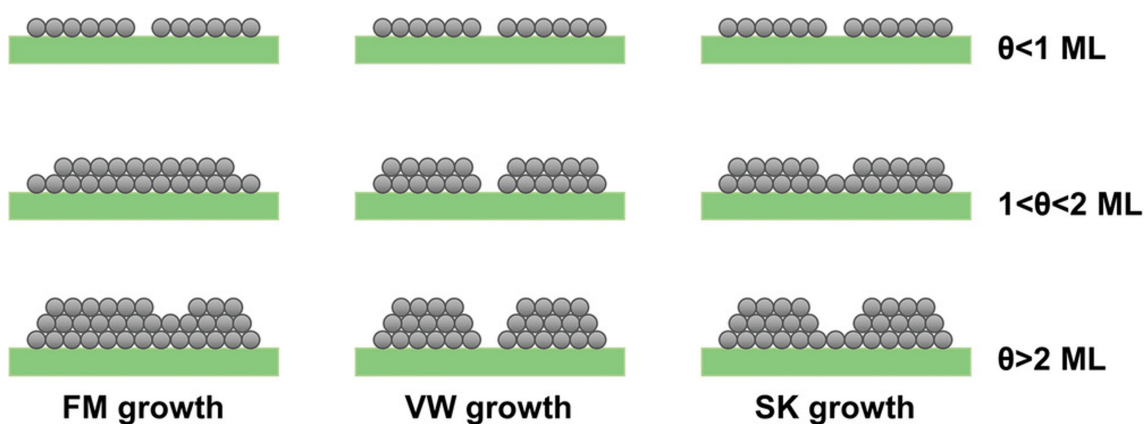


Figure 1.1.: Illustration of the different growth mode as a function of the layer coverage  $\theta$  in units of molecular layers (ML). FM denotes the Frank-van der Merwe, VW the Volmer-Weber and SK the Stranski-Krastanov growth modes. Reprinted with permission from Ref. [96]. © 2022 Wiley-VCH GmbH

For the electronic experiments the three-dimensional SAQDs are overgrown with a *capping layer*. Overgrowing interrupts the Ostwald ripening and reshapes the quantum dots [97].

The SAQDs utilised in this thesis were grown by the material combination of InAs on top of GaAs in the (100) orientation. The dots form themselves under the Stranski-Krastanow mode. Other combinations of materials are also known to form SAQDs under the Stranski-Krastanow mode, like CdSe on ZnSe [98], Ge on Si [99], PbSe on PbTe [100] or InGaAs on GaAs [101] to name just a few. A transmission electron microscopy image of a single InAs dot can be seen in figure 1.2. This dot was grown under comparable conditions to the dots used in the experiments in *Papers I to III*, it has a height of  $\approx 8$  nm and a diameter of  $\approx 30$  nm.

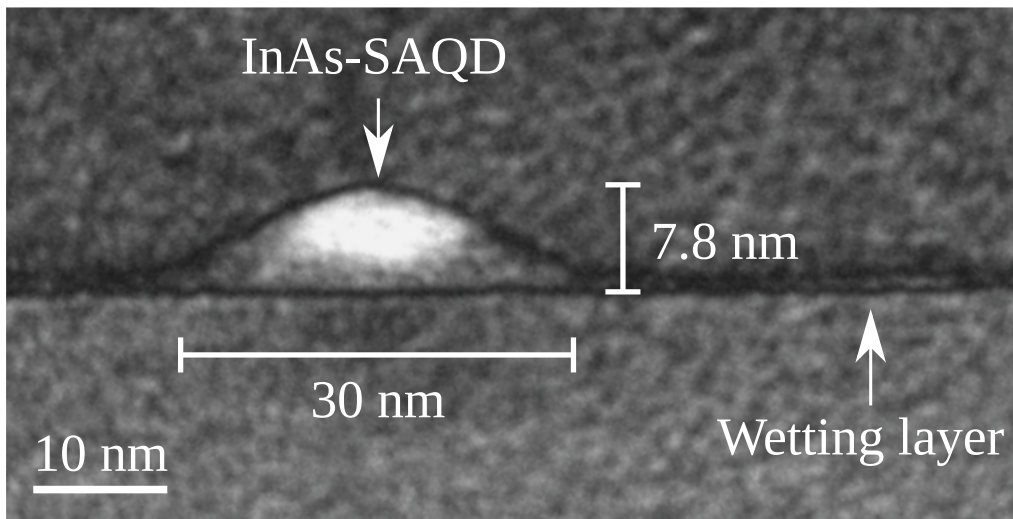


Figure 1.2.: Transmission electron microscopy image of a single InAs-SAQD. The dot has been grown under conditions similar to the ones studied in this thesis, so its dimensions and shape can be seen as representative. The image, measured by A. Ludwig and J. M. Chauveau, is reproduced and modified from Ref. [102] with permission from A. Ludwig.

### 1.1.2 Energy spectra

Quantum dots embedded in a host crystal can confine free charge carriers in all three spatial dimensions below their de-Broglie wavelength. To obtain the allowed energetic states inside the quantum dot, one has to solve the Schrödinger equation. The structure of the energetic states has been described by the *Fock-Darwin spectrum* [103, 104]. In this simplified model the confining potential inside the quantum dots is approximated to have a rotational symmetry, lateral to the growth direction. However in the growth direction itself, the confinement is so strong that only the ground state needs to be considered. This assumption is justified by the shape of the quantum dots, the extension of the dots in lateral direction is much larger than the one in growth direction, as shown in figure 1.2. The growth parameters can influence the shape of the dots and thus modify the shape of the confining potential, a more detailed theoretical description can be found in the literature, as in [105]. In the simplified model, the lateral potential  $V(x,y)$  in the  $x$  and  $y$  directions is approximated by a harmonic oscillator.

$$V(x,y) = \frac{1}{2}m^*\omega_0^2(x^2 + y^2) \quad (1.2)$$

Here,  $m^*$  is the effective electron mass and  $\omega_0$  the eigenfrequency. Without perturbation the energy levels are given by

$$E_{n,l} = (2n + |l| + 1) \hbar\omega_0 \quad (1.3)$$

where  $n$  is the radial quantum number,  $l$  is the quantum number of the angular momentum and  $\hbar$  is the reduced Planck constant. Only discrete values are allowed,  $l = 0, \pm 1, \pm 2, \dots$  and  $n = 0, 1, 2, \dots$ . Each energy level in this spectrum can be represented by its set of quantum numbers  $(n, l)$ . Each set can be occupied by two electrons due to spin degeneracy.

In the empty case the levels are degenerate. Similar to the labeling in a hydrogen atom, the three lowest levels are labelled the  $s$ - level with the quantum numbers  $(0, 0)$ , the  $p$ - level with  $(0, \pm 1)$  and  $d$ - level with  $(1, 0)$  and  $(0, \pm 2)$ . However, compared to real atoms, quantum dots have a two-dimensional instead of a three-dimensional confining potential. In consequence the  $p$ - level can only hold four and the  $d$ - level only six electrons.

A magnetic field  $B$ , applied perpendicular to the quantum dot layer, shifts its energetic structure according to the Schrödinger equation. The energetic levels are modified to [3]

$$E_{n,l} = (2n + |l| + 1)\hbar\Omega + \frac{1}{2}\hbar\omega_c l \quad (1.4)$$

with

$$\Omega = \sqrt{\omega_0^2 + \frac{1}{4}\omega_c^2} \quad (1.5)$$

and

$$\omega_c = \frac{qB}{m^*} \quad (1.6)$$

where  $q$  is the positive elementary charge. For such a non-zero magnetic field the degeneracy of the angular momentum quantum number is lifted.

The presented *Fock-Darwin model* has so far been a single particle model. When additional electrons are present in the dot, interactions between these particles have to be considered. A quantum dot can be thought of as a conductive island in its host crystal. This resembles a capacitor with a self-capacitance of  $C_s = 4\epsilon_r\epsilon_0 d$ , where  $\epsilon_0$  is the vacuum permittivity,  $\epsilon_r$  the relative permittivity of the surrounding material and  $d$  is the diameter of the quantum dot [106]. Charging this capacitor with an additional electron requires the *Coulomb-blockade energy*

$$E_{Coul.} = \frac{q^2}{C_s}. \quad (1.7)$$

This energy further lifts the spin degeneracy of the energy levels. Depending on the size of the quantum dots it can become comparable to the quantisation energy spacing  $\hbar\omega_0$ . For quantum dots used in this thesis with a diameter of  $\approx 30$  nm, as seen in figure 1.2, one can estimate  $E_{Coul.} \approx 12$  meV. A model calculation for the energetic spectrum of a SAQD can be found in figure 1.3 for the empty and occupied states.

The Coulomb barrier as described above is a purely classical picture where  $E_{Coul.}$  is a constant. Warburton et al. [5] have solved this problem a quantum mechanical approach. By perturbation theory they showed that the Coulomb blockade energy is a function of the quantum numbers of two electrons, with the one between the two  $s$ - levels being the largest.

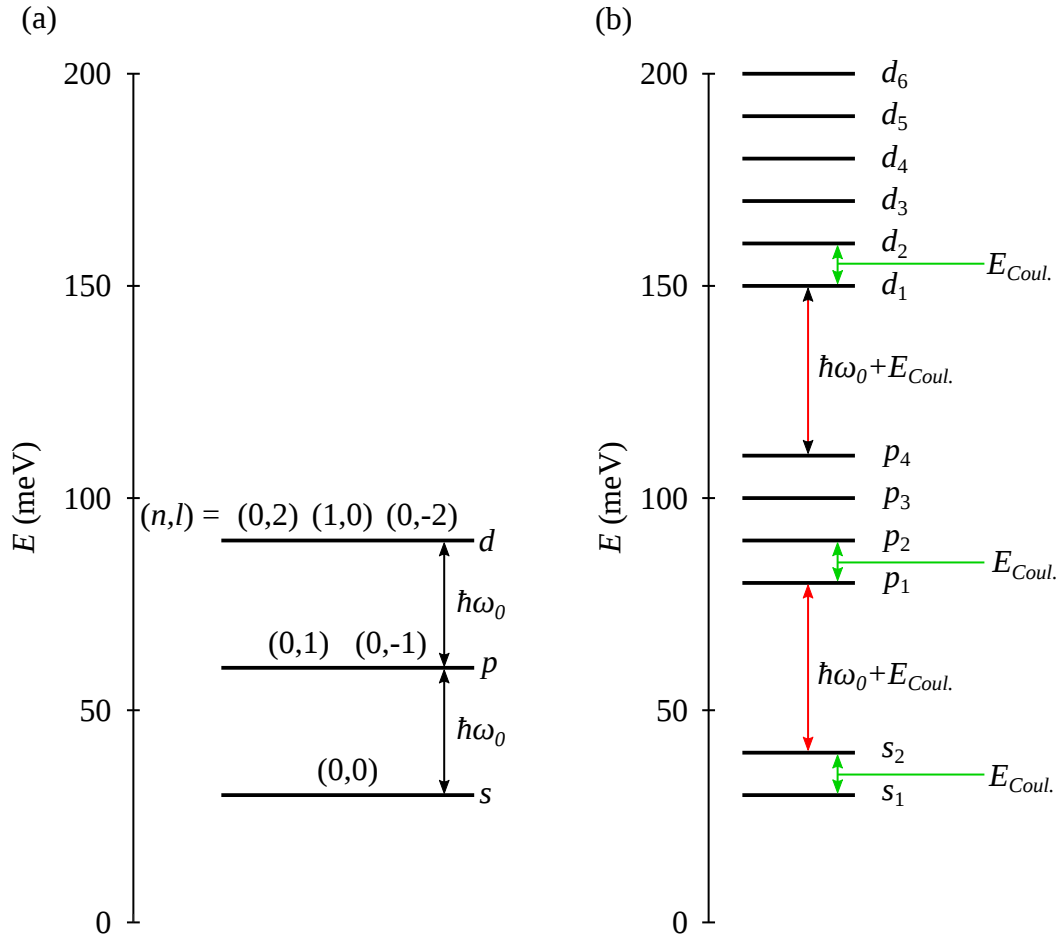


Figure 1.3.: Model calculation of the Fock-Darwin spectrum in an empty and an occupied dot, illustrated in (a) and (b) respectively. For this model, a coulomb blockade energy of 10 meV and a level spacing at zero magnetic field of  $\hbar\omega_0 = 30$  meV were chosen, similar values to the experimental data for the SAQDs under investigation [13, 107]. The energetic levels are labeled on the right side of the graph. For the unoccupied dots, the quantum numbers  $(n,l)$  are additionally written.

The energetic structure of quantum dots has been verified experimentally by capacitance voltage [108], deep level transient spectroscopy [35] and photo-luminescence experiments [109]. A detailed description of the interaction of the energetic levels in the occupied case can further be found in literature, such as in Refs. [3, 5, 108, 110]. Magnetotunnelling spectroscopy furthermore allowed to map out the wave

functions of the different energetic states [25, 111]. The measured distributions were in good agreement with those predicted by the harmonic oscillator approach, presented above.

## 1.2 Crystal defects

In an ideal crystal, each side of the lattice is occupied by its designated atom, resulting in a perfectly ordered and periodic structure. Real world crystals deviate from this perfect crystal structure due to the presence of various defects. These defects can range from atomic site errors, known as *point defects*, to more complex structures involving multiple atoms [112].

The defects can significantly change the shape of the bandpotential in their surrounding. Similar to the SAQDs discussed in section 1.1, crystal defects can induce additional energetic states within the bandgap of the semiconductor. These energetic levels are often referred to as *shallow level traps*, when their energetic levels are close to the energy bands, or *deep level traps*, when the energy levels are positioned closer to the center of the bandgap.

The presence of crystal defects can drastically affect the optical and electrical properties of the semiconductor material. For instance, defects such as impurities can increase the concentration of free charge carriers, enhancing the conductivity of the semiconductor [113].

Deep level traps find application in optoelectronic devices like light emitting diodes or solar cells where they are intentionally introduced to form radiative recombination centers [114]. However defects may also be undesirable in such applications. Deep level traps can form non-radiative recombination centers as well, which can significantly reduce the devices efficiency [115, 116]. Color centers are a specific type of deep level traps that alter the color of the crystal by absorbing light and reemit it at a specific wavelength [112]. The quantum properties of the color centers can also be used for quantum computing, likewise with the nitrogen vacancy color center of diamond [117, 118].

### 1.2.1 Point defects

Crystal defects can be classified into several types, depending on their structural origin [119]. Some defects involving only a single atomic lattice side, often called point defects, are exemplified in figure 1.4, for simplicity in a cubic lattice with monoatomic base. Depending on their atomic surrounding and origin, the defects can be charged positive, negative or neutral in the unoccupied state. Based on Refs. [112, 119] common point defects found in semiconductors are *vacancies*, *interstitials* and *impurities*.

A vacancy occurs when an atom is missing from its designated lattice side. This case is further highlighted in section 1.2.2, on the oxygen vacancy in rutile TiO<sub>2</sub> which is the subject of investigation in *Paper IV*.

An interstitial defect arises when an atom occupies a position between the regular lattice sites of the crystal. Interstitial atoms can be either a native crystal atom or a foreign atom.

Impurity defects are crystal foreign atoms within the crystal lattice. These impurities can replace native atoms, become interstitials or form more complex defects. Impurities are often deliberately introduced into the crystal in the form of doping, where they can drastically increase the conductivity of the semiconductor by providing additional charge carriers.

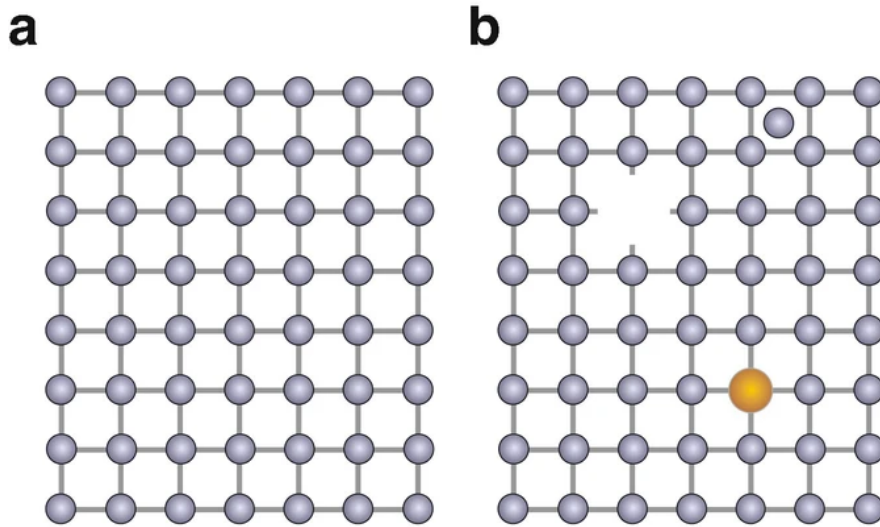


Figure 1.4.: Sketch of a perfect crystalline structure (a) and a crystalline structure with point defects (b). Both have a cubic lattice structure with a monoatomic basis. The defects in figure (b) are a vacancy on the top left, an interstitial on the top right and an impurity on the bottom right. Reproduced with permission from Springer Nature Ref. [119].

In real world devices, crystal defects are inevitable, even in the absence of intentional doping. These defects arise due to the limitations of the growth process and the thermodynamics of the intrinsic defects [112, 120].

Defects can also be introduced into the crystal after growth. High energy irradiation [121], electrons [122] and ions can create defects in the crystal lattice. Exposure to certain gas atmospheres can introduce specific defects, depending on the crystal material [123].

Annealing can reduce the density of defects, as it allows the atoms to move to a more energetically favorable position. Similarly, exposing the crystal to gas atmospheres can pacify certain types of defects [124].

Predicting the binding energy of a deep level trap requires detailed knowledge of the potential surrounding the trap and its interaction with the lattice and phonons. In limited cases the binding energy can be described by a modified hydrogen model, likewise on positively charged impurities that have energetic states close to the edge of the energetic band [113]. The potential of deep level traps is more accurately



described by a tight binding potential rather than by a long ranging Coulomb potential. Methods for approximating the binding energy of deep level traps include density functional theory (DFT) [125] and tight binding models [126]. Since the necessary knowledge of the structure of the trap is often not available, the binding energy of the deep level trap has to be determined experimentally.

Experimental methods to investigate the parameters of deep level traps are numerous, including photoluminescence spectroscopy [127] and capacitance transient based methods like the deep level transient spectroscopy [26], described in chapter 3 and the deep level transient photocapacitance spectroscopy [39], presented in *Paper IV*.

### 1.2.2 Oxygen vacancy of titanium dioxide

Titanium dioxide ( $\text{TiO}_2$ ) is a metal oxide material that has been extensively investigated due to its wide fields of applications, ranging from memristic devices [128], photocatalysis [129, 130], gas sensing [131, 132] to white paint pigments in various everyday items.

The three most commonly found crystalline phases of  $\text{TiO}_2$  are rutile, anatase and brookite. These phases differ in their unit cells, densities and bandgaps. For the purpose of this thesis only the rutile phase is relevant, as it is used as the host material for deep level traps in *Paper IV*. A sketch of the crystal structure of rutile  $\text{TiO}_2$  is shown in figure 1.5.

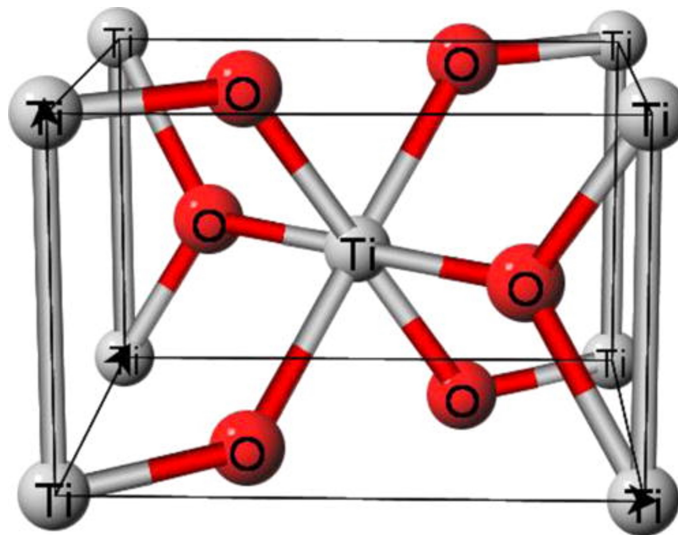


Figure 1.5.: Unit cell of a rutile  $\text{TiO}_2$  crystal. Reprinted from Chetry *et al.*, J. Appl. Phys. **110**, 113910 (2011) with the permission of AIP Publishing Ref. [133].

The defect investigated in *Paper IV* is the oxygen vacancy in rutile  $\text{TiO}_2$ . This defect is of particular interest due to its relevant role in the electroforming process,

giving rise to the memristor [128]. The oxygen vacancy can diffuse through the crystal and drift under the influence of an electric field. Models describing the drift behaviour under an electric field can be found in the literature, for instance in Ref. [134] and Ref. [135].

At the atomic level, an oxygen vacancy corresponds to a  $\text{Ti}^{3+}$  center, which forms a donor level that can be occupied predominantly by electrons [68, 136].

The oxygen vacancy can be introduced into the crystal, by growth under oxygen depletion or as an accompanist to doping. They can later be introduced into the crystal by high energy particle bombardment or hydrogen treatment, or by chemical reaction of organic compounds on the surface, as summarised in Ref. [68].

The binding energy associated with this trap has been determined using several experimental techniques, yielding values around 800 meV [66–68]. These experimental results are in agreement with theoretical calculations, which predict similar binding energies [137].

$\text{TiO}_2$  is known to exhibit further deep level traps, like the titanium interstitial or hydrogen related defects, which can be found in the literature [124, 136, 138].

### 1.3 Charge carrier dynamics

Crystal defects as well as SAQDs allow for energetic states inside the otherwise forbidden bandgap of the semiconductor. Free charge carriers can interact with these additional states, electrons can be captured and emitted from or into the conduction band  $E_C$ , holes can be captured and emitted from or into the valence band  $E_V$ . An overview over these processes is given in figure 1.6. The discrete energetic state at an energy  $E_T$  can capture charge carriers at a rate  $c$  or emit these at a rate  $r$ , indexed with  $n$  and  $p$  for electrons and holes respectively.

The samples investigated in this thesis were n-type Schottky junctions. In n-type semiconductors the density of free holes, and thus processes involving holes are negligible. Therefore, the following sections will only focus on the processes involving electrons. The corresponding equations for the processes involving holes are analogous and can be found in literature, such as Ref. [113].

#### 1.3.1 Capture

Electrons from the conduction band can reduce their energetic state by occupying the energetic state of a deep level trap or a SAQD. Energy and momentum have to be conserved during the process achieved by e.g. scattering with phonons [140] or with other charge carriers [141]. Under thermal equilibrium the capture rate  $c$  of electrons into an empty deep level trap is given by [142]

$$c = nv_{th}\sigma \quad (1.8)$$

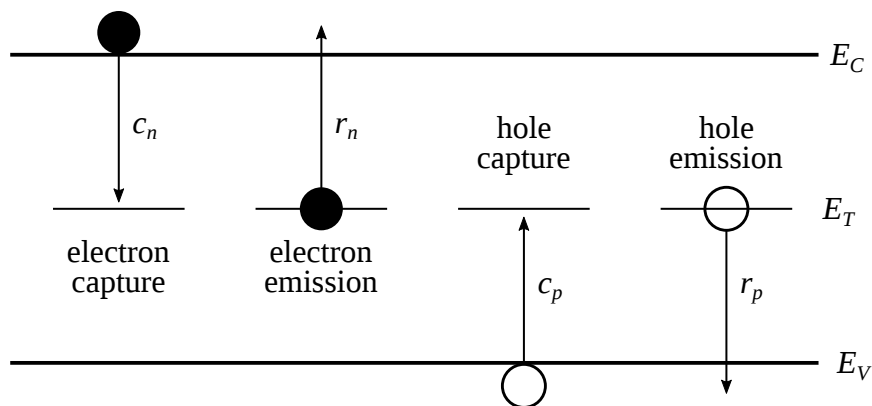


Figure 1.6.: Interaction of free electrons (filled circles) and holes (empty circles) in a crystal with the energetic state of a deep level trap. Adapted from [139].

where  $\sigma$  is the capture cross section of the trap,  $n$  is the electron density and  $v_{th.} = (3k_B T/m^*)^{1/2}$  is the mean thermal velocity of a free electron at temperature  $T$  with  $k_B$  the Boltzmann constant. Under experimental conditions additional electron capture mechanisms must be considered, especially when electrons can tunnel through a small enough barrier, as in *Paper II*, or can originate from leakage current [65].

### 1.3.2 Thermal emission

Electrons occupying a deep level trap or an energetic level in a SAQD can gain sufficient thermal energy to be excited into the continuous conduction band. Figure 1.7 visualises this process. A rate with which these electrons are emitted can be derived using detailed balance arguments [142].

At thermal equilibrium the occupation  $f$  of a discrete energetic state within the bandgap is given by

$$f = \frac{1}{1 + \frac{1}{g} \exp\left(\frac{E_T - E_F}{k_B T}\right)} \quad (1.9)$$

where  $g$  is the degeneracy of the occupied trap and  $E_F$  the Fermi level of the system. The occupancy does not change in time under thermal equilibrium, as many electrons are emitted from the occupied states, as they are recaptured in the unoccupied states.

$$rf = c(1 - f) \quad (1.10)$$

The capture rate under such conditions is given in the equation 1.8, the electron density is

$$n = N_C \exp\left(-\frac{E_C - E_F}{k_B T}\right) \quad (1.11)$$

where  $N_C$  is the effective density of states in the conduction band. Inserting into equation 1.10 yields in the thermal emission rate  $r_{th.}$  of an electron out of a deep level trap or energetic state in a quantum dot [143].

$$r_{th.} = \frac{N_C v_{th.} \sigma}{g} \cdot \exp\left(-\frac{E_b}{k_B T}\right) \quad (1.12)$$

This equation is in dependence of two of the traps' characteristics, the binding energy  $E_b = E_C - E_T$  and the capture cross section  $\sigma$ . In chapter 3 it is described how one can determine these two parameters experimentally from capacitance transients.

Under an applied electric field  $F$  the potential  $E_C$  is tilted, as also visualised in figure 1.7. This allows for the two emission pathways of tunneling and thermally assisted tunneling, discussed in the following sections. The electric field also affects the thermal emission rate. The potential is tilted, resulting in a potential lowering of the amount  $E_{PF}$  and consequently an increase in thermal emission. This is known as the *Poole-Frenkel effect*. For an one-dimensional Coulomb well a difference in energy, due to the Poole-Frenkel, effect is given by [144]

$$E_{PF} = 2q\sqrt{\frac{qF}{\epsilon_r \epsilon_0}}. \quad (1.13)$$

Detailed measurements of the Poole-Frenkel effect on the SAQDs used in *Paper I* and *II* can be found in Ref. [107].

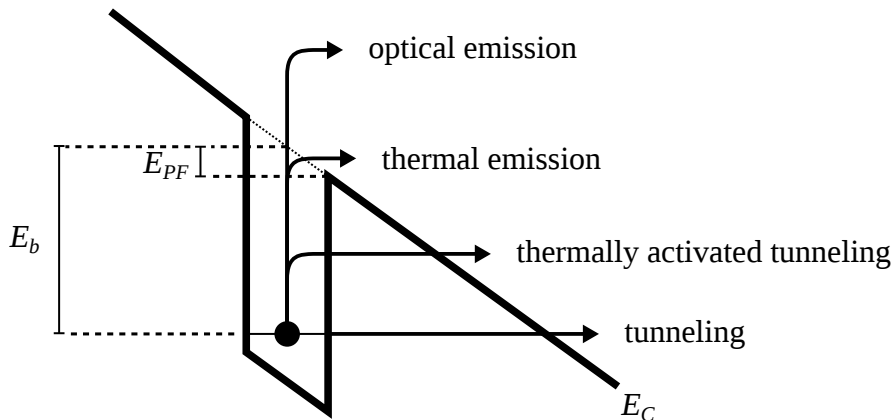


Figure 1.7.: Emission paths of an electron out of an energetic state within the bandgap under an applied electric field.

### 1.3.3 Tunnel emission

A confined electron can also escape by tunneling through the potential barrier. An electric field tilts the band potential. For suitable binding energies the barrier has a finite width, enabling quantum mechanical tunneling into the continuous energetic

bands. In the simplest case the barrier has a linear slope, as shown in figure 1.7. The tunneling rate has been calculated by [145]

$$r_{tun.} = \frac{qF}{4\sqrt{2m^*E_b}} \exp\left(-\frac{4}{3} \frac{\sqrt{2m^*} E_b^{3/2}}{q\hbar F}\right). \quad (1.14)$$

As the electric field is increased, the barrier gets thinner and the tunneling rate increases. The formula is independent of the temperature, the electric field at a fixed position inside a Schottky junction however may be not. For more complicated barriers, like parabolic ones, or tunneling in the presence of a magnetic field one can use the Wentzel-Kramers-Brillouin approximation, often related to as the WKB approximation [111, 146].

### 1.3.4 Thermally activated tunneling

Thermally assisted tunneling can be described as a combination of thermal activation and quantum mechanical tunneling. An electron in a deep level is excited to a quasi-level inside the trap. From this level, the electron can tunnel through the remaining thinner potential barrier, thus increasing the probability of tunneling. This problem was solved in a semi-classical approach by Vincent et al. [147]. Further quantum mechanical models that take phonon scattering into account can be found in literature [148, 149].

Following Vincent's approach, the emission rate for thermally activated tunneling  $r_{th.tunn.}$  can be described by introducing a factor multiplied by the thermal emission rate 1.12. This factor  $r_{th.tunn.}/r_{th.}$  is often labeled the *Vincent factor*.

$$\frac{r_{th.tunn.}}{r_{th.}} = 1 + \int_0^{E_b} \frac{1}{k_B T} \exp\left(\frac{E}{k_B T} - \frac{4\sqrt{2m^*} E^{3/2}}{3q\hbar F}\right) dE \quad (1.15)$$

### 1.3.5 Optical emission

Electrons in deep level traps or SAQDs can reach a higher energetic state by absorbing the energy of an incident photon. This state may be in the continuous conduction band, allowing the electron to be emitted. The optical emission rate  $r_{opt.}$  is given by [63]

$$r_{opt.} = \sigma_{opt.} \Phi \quad (1.16)$$

where  $\Phi$  is the incident photon flux and  $\sigma_{opt.}$  the optical capture cross section. It is noted that  $\sigma_{opt.}$  is in general a function of the energy of the incident photons, the binding energy, the temperature and the interaction of the deep level trap with the surrounding lattice, causing the *Franck-Condon shift* [63, 150–152].

The optical emission rate can be used to determine the parameters of the traps, as found in the deep level optical spectroscopy [63, 153]. Such a technique is especially useful for deep level traps with large binding energies, where thermal emission of electrons would require temperatures hardly realisable in experimental conditions. The optical emission rate is only relevant for *Paper IV*, where deep level traps in  $\text{TiO}_2$  are illuminated. All experiments with SAQDs in the *Papers I to III* were conducted in darkness. Literature on optically induced electron capture and emission from or into SAQDs can be found in Refs. [154] and [155].

## 1.4 Schottky junction

The samples investigated in this thesis are Schottky junctions consisting of a metal and an n-type semiconductor. The capacitance of these junctions acts as a sensor for the charge stored in the SAQDs or deep level traps. This section explains the relevant physical background of n-type Schottky junctions based on the Schottky-Mott model [75, 113, 156].

A metal and an n-type semiconductor are initially separated. The energy required to excite an electron at the Fermi level of the bulk of the metal  $E_F$  into the vacuum  $E_{vac}$  is called the work function of the metal, denoted  $\Phi_M$ . Similarly, the electron affinity  $q\chi$  of a semiconductor is defined as the energy required to excite an electron from the bottom of the conduction band  $E_C$ . When separated, both the metal and the semiconductor have their own defined thermal equilibrium. The two materials are now brought into contact, allowing charge to flow between them. Electrons can now thermalise into an unoccupied, lower energy state in the other material. For the highlighted n-type Schottky junction electrons diffuse from the semiconductor to the metal side. In this simplified model this occurs when the work function of the metal is smaller than the electron affinity. In reality this is only true in limiting cases, due to the surface properties of the materials [157, 158].

The electrons near the interface move into the metal side, leaving behind positively charged dopant atoms, that are no longer compensated by the negative electrons. On the metal side these electrons are attracted by the positively charged region and, being mobile, accumulate at the interface of the metal-semiconductor contact. In combination the charge neutrality is maintained. The charged volume is referred to as the *depletion region*. As the metallic side is very narrow due to the free electrons it is often referred to as solely the semiconductor side.

Charge transport in this region is governed by two mechanisms: Diffusion and drift of electrons. The space charge region creates an electron gradient, that causes electrons to diffuse into the space charge region from the crystal bulk. According to Poisson's law the space charge region builds up a linearly varying electric field. A drift current is created by this electric field opposing the diffusion current. The junction is in equilibrium when both currents have the same magnitude, resulting in zero net charge transport. At this point, the Fermi levels of both materials are aligned.

The linearly varying electric field furthermore creates a quadratic potential which

bends the energy bands of the semiconductor. Figure 1.8 illustrates a schematic representation of the energetic bands of an n-type Schottky junction under equilibrium conditions. Electrons moving from the metal side into the semiconductor must overcome the *Schottky barrier*  $\Phi_B = \Phi_M - q\chi$ , while in the opposite direction, they must overcome the *built-in potential*  $qV_{bi}$ .

In the Schottky-Mott model, the Schottky barrier and the built-in potential are determined by the work function of the metal and the electron affinity of the semiconductor, properties of the electrons in the bulk of the crystal. However, measurements have demonstrated that the Schottky barrier height is largely independent of the bulk material properties, but is primarily determined by the electronic structure of the junction's interface [113, 157, 159].

More sophisticated models take into account the high density of electronic states at the interface. The metal creates a large number of energetic states at the interface, the *metal-induced gap states*, that can hold a large amount of electrons, effectively shifting the Fermi level to the center of the semiconductor bandgap. This effect is often referred to as *fermi level pinning* [113, 160].

Predicting the exact value of the Schottky potential requires detailed knowledge of the electrical structure at the interface and remains an active area of research [158].

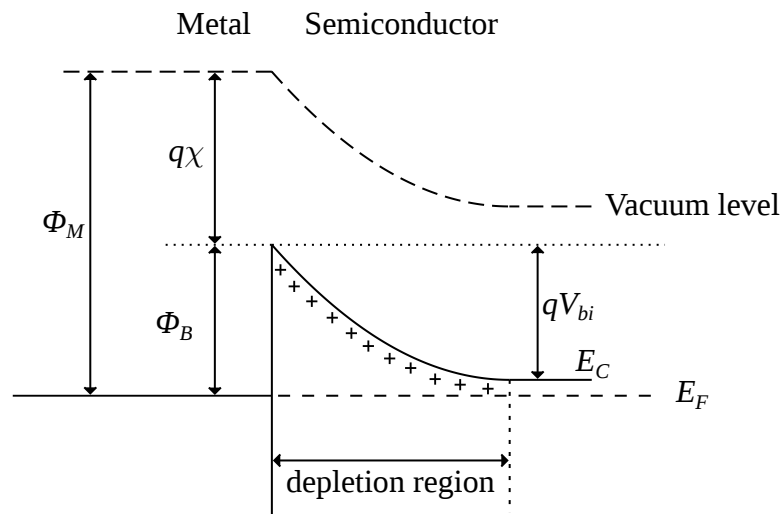


Figure 1.8.: Band diagram of a Schottky junction under equilibrium conditions. The black crosses in the depletion region denote the uncompensated ionised dopands.

A bias voltage  $V$  is now applied to the Schottky junction. Consistent with the experiments conducted in this thesis, the focus is on the scenario where the bias voltage is applied to the metal side of the junction with respect to a grounded semiconductor side.

When a bias voltage is applied, the Schottky barrier remains pinned to the Fermi level of the metal, causing the relevant changes to occur in the bandpotential of

the semiconductor. The built-in potential adjusts accordingly, requiring electrons to overcome a barrier of the height  $q(V_{bi} + V)$ . Following Poisson's equation the width of the depletion region has to adjust correspondingly. A negative bias voltage applied to the metal side results in an extended depletion region, while a positive bias voltage reduces the width of the depletion region in comparison to the equilibrium case.

In the experiments described in *Papers I to III*, the SAQDs are at a fixed position within the Schottky junction. The application of a bias voltage allows for tuning parameters such as the electric field and distance between SAQDs and the free electron gas. To determine the capture and emission rates correctly it is necessary to accurately determine the electric field and electron density distributions at the location of the SAQDs. These values were extracted from a one-dimensional Poisson-Schrödinger solver [161].

### 1.4.1 Current voltage characteristics

Electrons moving from the metal to the semiconductor side must overcome the Schottky potential, which, in approximation, is independent of the bias voltage due to Fermi level pinning. In contrast, electrons moving from the semiconductor to the metal side encounter a potential barrier that depends on the applied bias voltage. The transport properties can be calculated using thermionic emission theory as demonstrated in Ref. [113]. The density of electrons with sufficient energy to overcome the barrier increases exponentially with increasing bias voltage, resulting in an exponential bias voltage relation. The current density can be expressed as

$$J(V) = R^* T^2 \exp\left(-\frac{\Phi_B}{k_B T}\right) \cdot \left[\exp\left(\frac{qV}{k_B T}\right) - 1\right] \quad (1.17)$$

where  $R^* = \frac{m^*}{m_0} \cdot 120 \frac{\text{A}}{\text{cm}^2 \text{K}^2}$  is the effective Richardson constant with  $m_0$  the electron mass.

This approach can be extended to include diffusion [162] and tunneling currents [163]. For real world devices the impurities and defects at the interface have to be further considered, which may lead to leakage or break-through currents.

### 1.4.2 Capacitance voltage characteristics

In a Schottky junction, opposing charges are present, namely the one in the space charge region  $Q$  and in the metal. From the differential capacitance relation it can be shown [156]

$$C(V) = -\frac{dQ}{dV} = A \frac{\epsilon_0 \epsilon_r}{z_{dep}} = A \cdot \sqrt{\frac{\epsilon_0 \epsilon_r q n_D}{2(V_{bi} - V)}} \quad (1.18)$$

where  $A$  denotes the area of the gate,  $\epsilon_r$  the relative permittivity of the semiconductor,  $z_{dep}$  the width of the depletion region and  $n_D$  the doping density. The Schottky



junction can be thought of as a plate capacitor wherein the distance between the plates is the width of the depletion region. For inhomogeneous doping or charge stored in SAQDs or deep level traps, the capacitance changes according to Poisson's law.

### 1.4.3 Capacitance transients

A Schottky junction exhibits a capacitance that is dependent upon the charge stored within the depletion region. When deep level traps or SAQDs are present within the depletion region, additional charge can be captured or emitted from or into the depletion region. This results in a time-dependent change in the width of the depletion region, which in turn affects the capacitance. An overview of these capture and emission processes was given in section 1.3. The first capacitance transient measurements of charge in deep level traps were made by Williams et al. in 1966 [164]. In 1974 Lang proposed the *Deep Level Transient Spectroscopy* (DLTS) to extract the parameters of the traps from capacitance transients [26].

When charge from deep level traps or SAQDs is present in the depletion region, the band profile and consequently the capacitance changes according to Poisson's law. In the experiments presented in this thesis electrons are captured or emitted from deep level traps and SAQDs in an n-type Schottky junction.

From a qualitative perspective, the negative charge creates an additional potential hub. To satisfy Poisson's equation this hub needs to be compensated by an additional positive charge from the dopants of the semiconductor. Compared to the case without negative charge, the depletion region has expanded.

For a homogeneously doped Schottky junction embedding a single layer of SAQDs, the capacitance is a function of the time-dependent occupancy of the SAQDs. As a large number of SAQDs is present, the charge can be approximated by a charge sheet density  $\rho(t)$  at the SAQDs' position  $z_Q$ . The capacitance can be written as [106]

$$C(V,t) = \epsilon_r \epsilon_0 A \sqrt{\frac{q^{n_D}}{2(\epsilon_r \epsilon_0 (V_{bi} - V) - \rho(t) z_Q)}}. \quad (1.19)$$

In an approximation, valid for  $\rho(t) \ll \epsilon_r \epsilon_0 (V_{bi} - V) / z_Q$ , this equation can be approximated as

$$C(V,t) \approx C_{Schottky}(V) \cdot \left(1 + \frac{\rho(t) z_Q}{2\epsilon_r \epsilon_0 (V_{bi} - V)}\right) \quad (1.20)$$

where  $C_{Schottky}$  is the junction without charge in the SAQDs, as given by equation 1.18. The formula 1.20 demonstrates that, to a good approximation, the capacitance of the Schottky junction follows linearly the occupation dynamics of the quantum dots. The exponential decay processes, as described in section 1.3, are reflected in the exponential decay function of the capacitance.

In *Paper III* a Schottky junction with two layers of SAQDs was under investigation. In a similar approach, the capacitance can be calculated as

$$C(V,t) = \epsilon_r \epsilon_0 A \sqrt{\frac{qn_D}{2(\epsilon_r \epsilon_0 (V_{bi} - V) - \rho_B(t)z_B - \rho_T(t)z_T)}}. \quad (1.21)$$

Here the indices  $B$  and  $T$  denote the bottom and top layers respectively, two layers of SAQDs at different positions in the junction. A detailed description can be found in *Paper III*.

---

# Chapter 2

## Experimental techniques

### 2.1 Capacitance transients recording

As previously stated in section 1.4.3, the occupation dynamics of the SAQDs and deep level traps within the depletion region of a Schottky junction can be studied by the time-dependent capacitance of the junction. In this thesis, the capacitance measurements were performed with the help of a lock-in amplifier, as illustrated in figure 2.1. Similar experimental setups have been reported in the literature, see Refs. [47, 107].

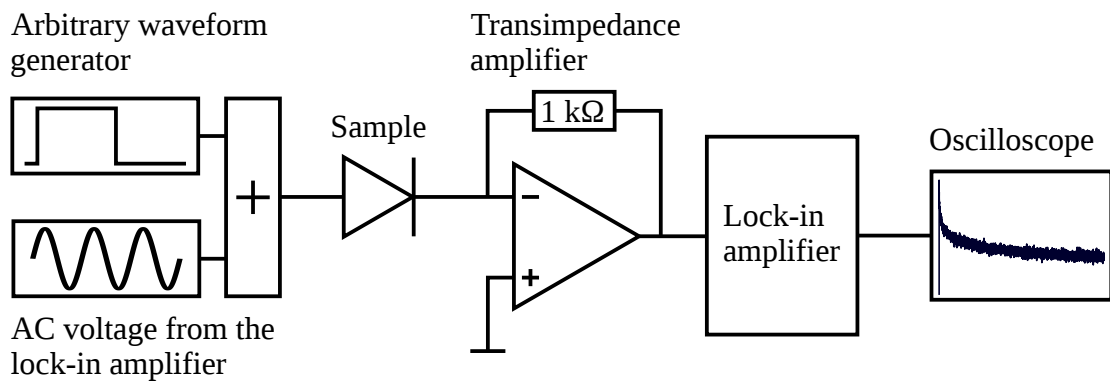


Figure 2.1.: Sketch of the experimental setup used to measure the capacitance in this thesis.

A HF2LI lock-in amplifier from *Zurich Instruments* generates an AC voltage signal  $V_{AC}$ , typically with an amplitude of 10 mV and a frequency  $f$  of 30 MHz. This signal was connected to the anode side of the Schottky junction. The cathode of the junction was kept at virtual ground by the input of the HF2TA transimpedance amplifier.

In addition to the AC voltage, a bias voltage can be superimposed. This bias voltage

---

was generated by a Keithley model 3390 arbitrary waveform generator and can take the form of a DC bias voltage, used for capacitance voltage spectroscopy, or a bias pulse, used for transient measurements. The addition was done internally by the lock-in amplifier.

An out-of-phase current  $I_y$  proportional to the capacitance flows through the sample.

$$C = \frac{I_y}{2\pi f V_{AC}} \quad (2.1)$$

Subsequently, the HF2TA transimpedance amplifier converts this out-of-phase current back into an AC voltage signal. A sensitivity of 1 kV/A was selected as a compromise between gain and bandwidth [165]. The AC voltage signal was read out by the HF2LI lock-in amplifier and demodulated into in-phase and out-of-phase signals. Potential phase shifts due to runtime of the signals through the cables can be compensated by a digital offset [166].

The demodulation process plays a crucial role in determining both the time resolution and signal-to-noise ratio in the output signal. A longer timeconstant in the demodulators translates into a reduced noise level, albeit at the expense of the time resolution. In the experiments a time sampling interval was chosen where the demodulators reach 99% of their settling value [165].

With a frequency of typically 30 MHz a time resolution of 10  $\mu$ s was achieved. The signal-to-noise ratio could be further improved by averaging repetitive measurements of the transients.

The demodulated out-of-phase component of the input signal can then be read out either digitally from a computer or through the analogue output of the lock-in amplifier. However, the data transfer rate from the lock-in amplifier to the computer was insufficient for the transient measurements. A PicoScope 5444B digital oscilloscope from *Pico Technology* was used to record the analogue signal output of the lock-in. The time resolution of the oscilloscope was adjusted to match the settling time selected for the demodulators. Additionally, averaging of the repetitive transients was done by the oscilloscope to increase the signal-to-noise ratio. The captured transients were then saved on an external hard drive. A typical recorded capacitance transient is illustrated in figure 2.2.

In order to calculate the capacitance value from this analogue output voltage of the lock-in amplifier, it is necessary to consider the scaling factor and offset, which can be adjusted at the interface of the lock-in amplifier. Furthermore, a negative sign arises from the HF2TA transimpedance amplifier. Impedance matching of the measurement devices is crucial and for the experiments an input impedance of 50  $\Omega$  was chosen for the lock-in amplifier to ensure a high bandwidth [165], resulting in an additional factor of 2.

As the runtime of the signals through the cables becomes comparable to the period of the AC test signal, a shift in phase must be considered or compensated by a digital phase offset within the lock-in amplifier. Caution must be given to the dielectric relaxation condition of the sample [113], the selected AC frequency should be sufficiently low to observe the correct capacitance amplitude accurately.

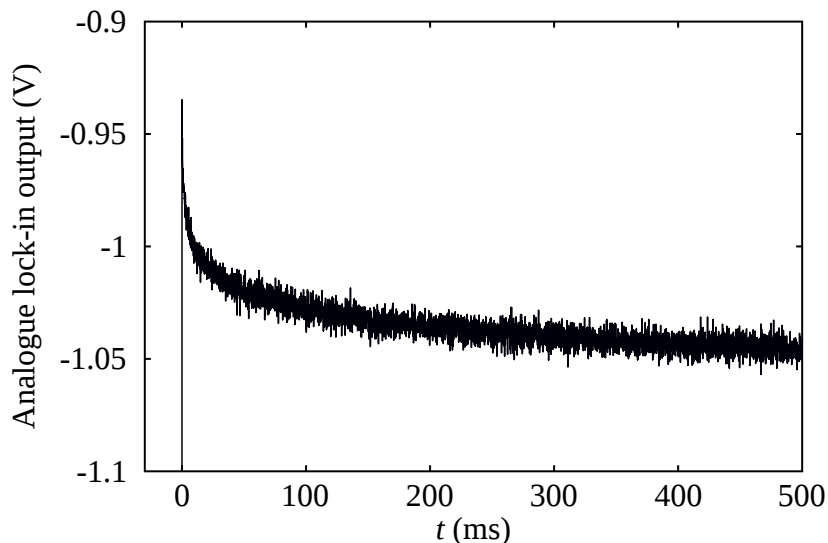


Figure 2.2.: Example of the measured out-of-phase analogue output signal of the lock-in, proportional to the capacitance of the sample. Shown is a transient obtained from the sample used in *Paper II*, described in detail in section 2.2.1 in response to a bias pulse with a preparation voltage of  $-1.5$  V and a measurement voltage of  $-0.35$  V at a temperature of 5 K and zero magnetic field.

## 2.2 Samples

Three different samples have been studied in this thesis. This section gives an overview over these samples. Two of these samples contained SAQDs and one consisted of rutile  $\text{TiO}_2$  with deep level traps.

### 2.2.1 Single layer SAQDs sample

The first sample investigated in *Paper I* and *II* was an n-type Schottky junction containing a single layer of SAQDs. S. Scholz, from the group of Prof. A. D. Wieck from the Lehrstuhl für Angewandte Festkörperphysik at the Ruhr-Universität Bochum, had grown the sample by molecular beam epitaxy. The growth protocol can be found in the appendix A, the sample is identified by the number # 14691. A visualisation of the different layers and a sketch of the resulting band diagram can be found in figure 2.3.

The sample was grown on an undoped GaAs single crystal. An initial 100 nm of undoped GaAs was deposited, followed by a 100 nm GaAs/AlAs superlattice. This superlattice acts as a barrier that traps impurities that might diffuse from the lower layers to the electronically active regions of the sample. Subsequently a 50 nm layer of GaAs was added.

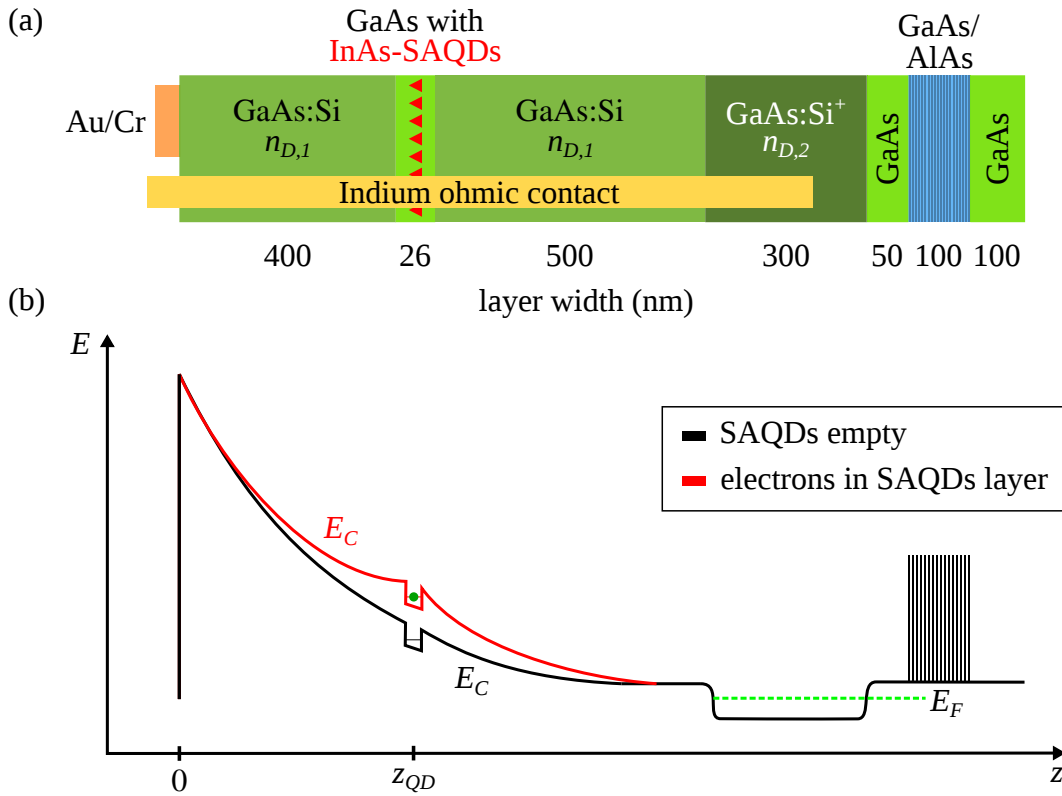


Figure 2.3.: (a) Layer structure of the sample containing a single layer of SAQDs, indicated by the red triangles. (b) Sketch of the resulting conduction band profile under a negative applied bias voltage in the case for unoccupied (black curve) and occupied (red curve, the green circles denote the electrons) SAQDs.

Next, a 300 nm thick layer of degenerately Si-doped GaAs was deposited. The high doping density of  $n_{D,2} = 2 \times 10^{18} \text{ cm}^{-3}$  results in a quasi-metallic behaviour of this layer, allowing it to function as an electron reservoir and back contact for the Schottky junction in the experiments.

A 500 nm wide layer weakly Si-doped GaAs acts as a spacer between the back contact and the SAQDs. The doping density was targeted at  $n_{D,1} = 2 \times 10^{16} \text{ cm}^{-3}$ . A *Mott-Schottky analysis* conducted in *Paper II* [38] however revealed an apparent doping density of  $n_{D,1} = 9.6 \times 10^{15} \text{ cm}^{-3}$ .

On top, the InAs SAQDs were embedded in the middle of a 26 nm wide undoped GaAs capping layer. The SAQDs were grown under the Stranski-Krastavov mode, described in section 1.1.1. For similar, uncapped layers of SAQDs AFM scans were carried out, revealing a sheet density of  $n_{QD} \approx 10^{14} \text{ m}^{-2}$ , while TEM images as in figure 1.2 had shown that the individual quantum dots have a diameter and height of approximately 30 nm and 8 nm respectively.

The final layer was a 400 nm wide layer of weakly Si-doped GaAs. The doping density was the same as in the previous doped layer. This layer acts as a spacer between

the SAQDs and the surface of the crystal.

The wafer initially had a circular shape with a diameter of 75 mm. A  $5 \times 5 \text{ mm}^2$  piece was cut out. Optical lithography, as described in section 2.3, and metal evaporation were used to create 12 square AuCr gates with an edge length of  $300 \mu\text{m}$ . Small pieces of indium (In) were placed at the edges of the sample. These were alloyed into the structure by thermal treatment, creating a conductive channel to the degenerately doped layer of the sample. The lithography, evaporation, alloying process and contacting of this sample, was carried out by C. Rothfuchs-Engels, who at the time was a member of the group of Prof. A. D. Wieck.

The sample was inserted into a chip carrier and glued there using polymethylmethacrylate (PMMA). One AuCr gate was connected to an electronic pad in the chip carrier by bonding with a gold wire. The In contact was connected to a pad of the chip carrier using silver epoxy glue and a gold wire. A photograph of a similarly processed sample can be seen in figure 2.4.

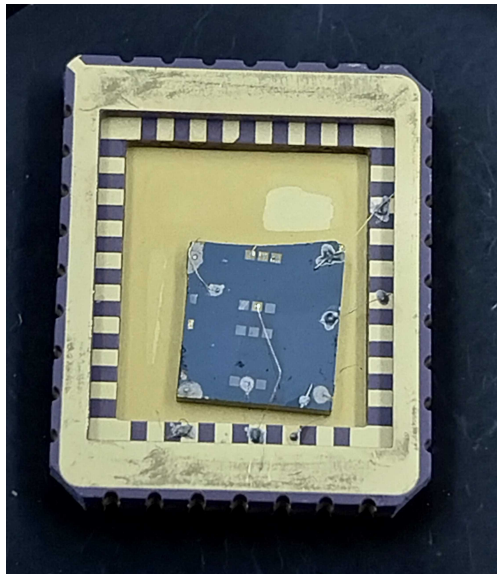


Figure 2.4.: Photograph of the processed sample containing two layers of SAQDs, described in section 2.2.2.

### 2.2.2 Double layer SAQDs sample

The second sample, used in *Paper III*, was an n-type Schottky junction containing two layers of SAQDs. The growth process was carried out by N. Bart from the group of Prof. A. D. Wieck at the Lehrstuhl für Angewandte Festkörperphysik at the Ruhr-Universität Bochum, again using molecular beam epitaxy. The growth protocol is provided in the attachment B, with the sample number #15070. A vi-

sualisation of the layer structure and band potential can be found in figure 2.5.

This sample was grown in close proximity to the first sample. A GaAs wafer was utilised as substrate. The superlattice and back contact layers followed the same pattern as in the first sample, described in section 2.2.1. A 490 nm thick weakly Si-doped spacer layer was grown on top of that, with a doping density of  $n_{D,1} = 7 \times 10^{15} \text{ cm}^{-3}$ , extracted from the *Mott-Schottky analysis* in *Paper III*. The first layer of SAQDs was then positioned, embedded in the center of a 24 nm thick undoped layer of GaAs. The SAQDs were grown with the Stranski-Krastavov mode, described in section 1.1.1. The growth conditions were similar to those of the single layer sample, so identical parameters for size and shape are assumed. After a 180 nm thick layer of weakly Si-doped GaAs, the second layer of SAQDs was grown, again in the middle of a 22 nm thick layer of undoped GaAs, under the same experimental conditions as the first layer. Then 220 nm of weakly Si-doped GaAs were deposited.

Thus, the sample contains two layers of SAQDs, one layer being at a distance of 232 nm, and the other at 432 nm from the crystal surface.

A  $5 \times 5 \text{ mm}^2$  piece was cut out from the wafer, AuCr square gates with an edge length of  $300 \mu\text{m}$  were applied by lithography steps. The back contact was again connected using alloyed In, identical to the first sample in section 2.2.1. However, the lithography and processing steps were carried out by the author of this thesis. An image of the processed sample can be seen in figure 2.4.

### 2.2.3 Titanium dioxide sample

The sample used in *Paper IV* consists of a thin layer of  $\text{TiO}_2$  sandwiched between a nickel (Ni) and a gold (Au) electrode. All steps of sample preparation and processing were carried out by Prof. Dr. C. C. Bof Bufon and Dr. L. Merces, both at that time employed at the Brazilian Nanotechnology National Laboratory at the Brazilian Center for Research in Energy and Materials in Campinas, Brazil.

The uniqueness of this sample lays in the use of a so-called *rolled-up nanomembranes* (rNM) as an electrode. These are electronically addressable metallic tubes with a diameter typically in the  $\mu\text{m}$  range. The primary advantage of using an rNM as electrode over a conventional flat wire electrode is its optical property. Incident photons are guided along the outer wall of the rNM, resembling a whispering gallery hall [167]. They reach the back of the tube where they illuminate the semiconductor material that would otherwise be in the shadow of the metal gate, allowing a high illumination rate [168, 169].

An optical microscopy image of one rNM on the sample is shown in figure 2.6. The image was obtained using a Nikon Eclipse ME600 optical microscope with a Nikon DS-2Mv digital adapter.

The rNM and the Ni electrode are indexed accordingly. Together, they form a cross-wire like junction. Au pads are connected to both ends of the rNM as well



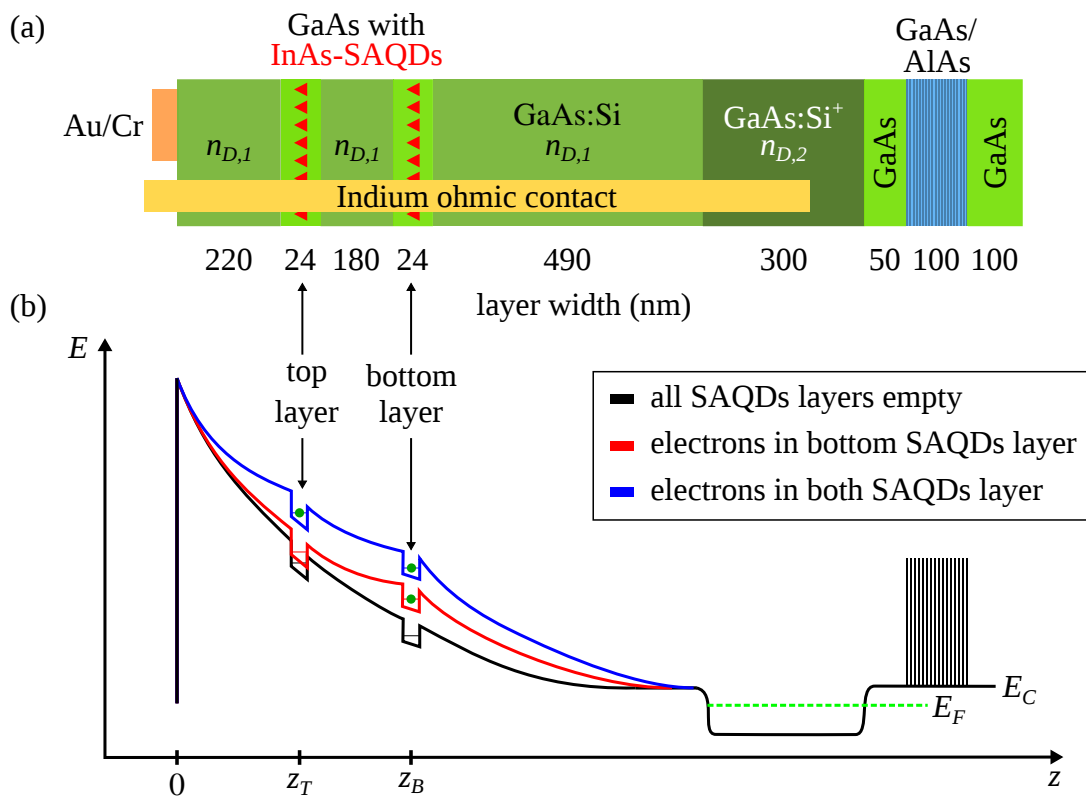


Figure 2.5.: (a) Layer structure of the sample containing two layer of SAQDs, indicated by the red triangles. (b) Sketch of the resulting conduction band profile under a negative applied bias voltage for various SAQDs occupation scenarios. The green circles again denote the electrons.

as to the Ni electrode, from which both can be bonded into the pads of a chip carrier.

The technique for processing rNMs is described in detail in the literature [69, 70]. Briefly, the structures were patterned on a silicon (Si) chip, covered by a  $2\ \mu\text{m}$  thick layer of silicon dioxide ( $\text{SiO}_2$ ). An Au film with layers Cr and titanium (Ti) on top was patterned over a germanium oxide ( $\text{GeO}_x$ ) sacrificial layer. This metal film will later form the rNM. A Ni electrode was added using photolithography. A 50 nm thick film of  $\text{TiO}_2$  was then deposited by atomic layer deposition.

The rolling-up process was initiated by removing the sacrificial layer of  $\text{GeO}_x$  with water. The strain, induced by the combination of Cr and Ti was released by curling off the film. This curling proceeded until the Au-coated nanotube landed on the  $\text{TiO}_2$  substrate.

32 Ni/ $\text{TiO}_2$ /Au vertical junctions were fabricated on a single chip. Again the chip was glued into a chip carrier and the Au contacts on the chip were connected to those in the chip carrier.

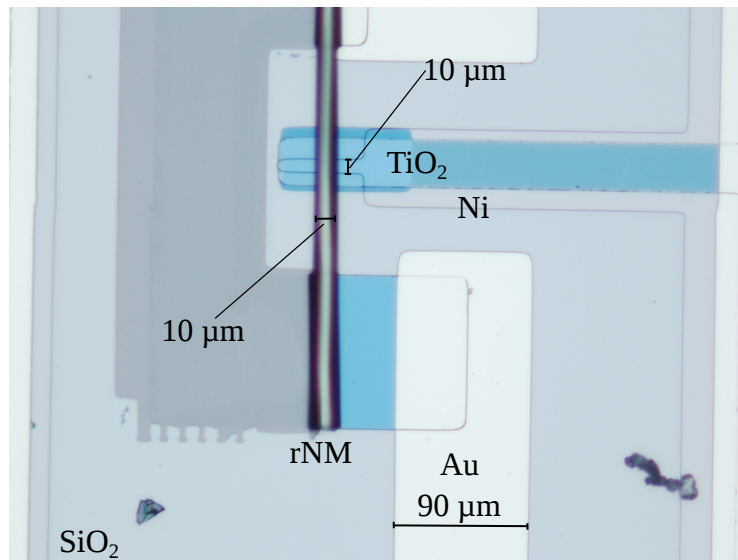


Figure 2.6.: Optical microscopy image of a single Ni/TiO<sub>2</sub>/Au vertical junction.

## 2.3 Sample preparation

This section discusses the techniques necessary for processing semiconductor material used in this thesis. These include lithography, and deposition of metal onto the surface of the semiconductor. Other commonly found techniques like etching have not been carried out in this thesis.

The lithography and the metal deposition steps of the sample used in *Paper III*, described in 2.2.2, were performed by the author of this thesis. The other samples were kindly provided and processed by the scientists mentioned in the sections 2.2.1 and 2.2.3.

The sample material was provided in the form of a quarter of a wafer disc with an initial diameter of approximately 75 mm. A smaller piece of the size 5 mm × 5 mm was cut out by scratching on the back of the wafer and by consecutively breaking along the crystal axis. The surface of the wafer was covered with photoresist to protect it from dirt and scratches.

The first step was to remove the photoresist by bathing the sample successively in acetone, isopropanol and deionised water. This step could be performed receptively until the desired level of surface cleanliness was achieved. Residual water was removed by heating the sample to 110 °C for 1 min.

Optical lithography, or photolithography, is a technique for patterning predefined geometric structures from a glass mask into a photoresist on the surface of a sample. The photoresist consists of polymers in a solvent, exposure to radiation breaks the polymer chains. Depending on the photoresist and subsequent processing steps, these polymer chains can be either sensitive or more resistant to certain solvents, named developers. In the positive process, the chains exposed to UV light are solv-

able by a developer. In the negative process the illuminated regions are resilient to the developer. While both positive and negative processes can create the same pattern by appropriate mask selection, the negative process creates an undercut profile in the photoresist, which is advantageous for lift-off steps [75].

The image reversal resist AZ 5213 E was used for the lithography. This resist can be used for both positive and negative lithographies. However, only negative lithography was employed in this thesis. The resist is applied to the surface of the sample, spinning at 5000 rpm for 30 s provides a uniform resist layer with a thickness of 1-2  $\mu\text{m}$ . The solvent is then removed from the resin by heating the sample on a hotplate at 110  $^{\circ}\text{C}$  for 40 s. Rehydration is necessary for the later photoreaction, so the sample is stored at room air for approximately 1 min, ideally at a relative humidity of 50 %.

The sample was placed under a mask and irradiated with UV light for 6 s. A reverse bake at 117  $^{\circ}\text{C}$  for 45 s reconnected the polymers in the illuminated regions, making them resilient to the developer. The entire sample was then illuminated again for 32 s to make the regions previously under the mask susceptible to the developer. The developer AZ 726 MIF was used to remove these parts from the surface.

Metal films were deposited onto this patterned surface using a BOC Edwards Auto 500 evaporation system. The sample was then placed in its vacuum chamber. The selected metal was heated by an electron beam, vaporised particles could travel through the chamber and reach the surface of the sample. The growth rate and thickness of the films could be monitored by a calibrated oscillating quartz crystal placed next to the sample. Typical growth rates for Cr or Au were 0.1 nm/s for smooth surfaces. For the processed sample a combination of 10 nm of Cr followed by 200 nm of Au was deposited.

The sample was cleaned with subsequent baths in acetone, isopropanol and deionised water to remove the photoresist with the metal layer on top, called the *lift-off*. The metal film remained on the patterned structure on the semiconductor surface.

Small droplets of In were placed at the edges of the sample. The sample was heated to 400  $^{\circ}\text{C}$  for 2 min to diffuse the In to the back contact of the sample.

The Au pad was electronically bonded using mechanical bonding and the In contact was bonded using conductive silver epoxy glue.

## 2.4 Cryogenic setup

The experiments in this thesis covered a temperature range from 5 K to 330 K, some of which required specific gas atmospheres or magnetic fields. This section presents the cryogenic setup in which these conditions were established.

### 2.4.1 Linkam HFS 600 cryostat

The experiments conducted in *Paper IV* required a temperature range from 200 K to 350 K as well as a well-defined gas atmosphere around the sample. These conditions were achieved by using a Linkam HFS 600 cryostat connected to an LNP 95 cooling

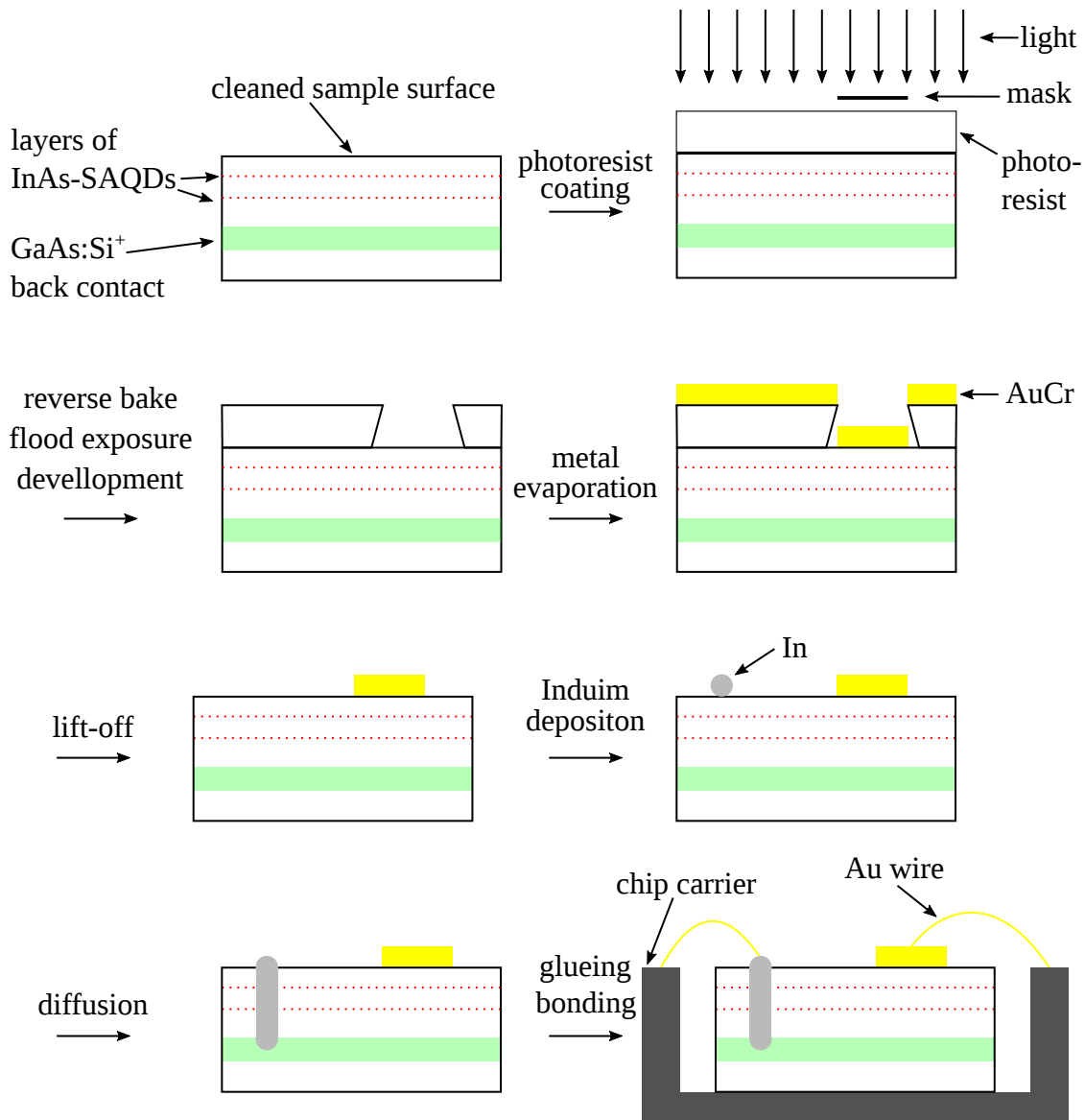


Figure 2.7.: Schematic illustration of the negative lithography and sample contacting step conducted on the sample containing two layers of SAQDs.

unit. The cooling unit pumped liquid nitrogen from a bath container through tubes inside the cryostat's chamber, reaching temperatures as low as 150 K. Heating coils inside the chamber allowed for measurements above room temperature, up to 450 K. A Pt1000 sensor was added to the sample socket to give an accurate value of the temperature by performing a four-wire measurement of its resistance. The chamber was connected to a nitrogen bottle, the gas flow was controlled by a Bronkhorst EL-Flow series gas flow controller. The experiments were conducted under a constant gas flow of typically 50 ml/min. Prior to the experiments, the chamber and sample were heated for several minutes under high nitrogen flow to remove the moisture, as it could affect the TiO<sub>2</sub> [123, 170]. An optical fiber was added to the measurement chamber. The fiber was attached to the top side of the chamber, underneath of it

was the sample. On the other side of the fiber was the LED. The LED was placed at a spacial distance from the cryostat since the wavelength of the emitted photons and intensity are a function of temperature.

### 2.4.2 Liquid nitrogen bath

In *Papers I to III* experiments are presented that require stable temperatures over a long period of time, typically one week per measurement. One experimental realisation of such conditions is the liquid nitrogen bath. Evaporation of the liquid nitrogen maintains a constant temperature of 77 K inside the liquid. A dewar with a volume of 120 L was used for the experiments. The metallic boundaries were grounded and acted as an additional Faraday cage, shielding the sample from electronic noise from the outside world. Furthermore, the openings of the dewar could be covered easily with black cloth. The sample was mounted on a rod that allowed to put it in the liquid phase of the nitrogen. Coaxial wires led to the contacts of the sample and to the outside to the measurement instruments.

### 2.4.3 Dilution refrigerator

For the temperatures in the range of 5 K to 90 K a dilution refrigerator from *Leiden Cryogenics* was used. The cryostat was cooled by a pulse tube cooler with  $^4\text{He}$  as working fluid. A temperature as low as 3 K could potentially be achieved. The temperature could further be reduced by a mixture of  $^4\text{He}$  and  $^3\text{He}$ , however this was not used for the conducted experiments.

The sample was mounted inside the cryostat and was made electronically accessible via coaxial cables connected to feedthroughs with the outside of the cryostat. Multiple Faraday shields protected the sample from external electronic noise, the vacuum chambers and gold foils protected from the heat and thermal radiation. Heating units allowed to establish a temperature above the base temperature. A calibrated CX-1010 Cernox sensor from LakeShore Cryotronics was mounted next to the sample to obtain an accurate temperature, again by a four-wire resistance measurement. The system was equipped with a superconducting solenoid, capable of generating a magnetic field of up to 11 T.



---

# Chapter 3

## Deep level transient spectroscopy

*Deep level transient spectroscopy* (DLTS) is a technique for characterising deep level traps in semiconductors, first proposed by Lang in 1974 [26]. In the original proposal the emission of charge carriers from deep level traps was observed by capacitance transients. From the temperature dependence of these emission rates, it is possible to extract the binding energy and capture cross section, two important characteristics of deep level traps.

Since the concept of DLTS was first presented it has undergone significant advancements with the development of further measurement and data evaluation techniques as well as applications. For example, the deep level optical spectroscopy (DLOS) uses photons of varying energies to excite charge carriers out of the the deep level traps [63]. Another technique, the thermally stimulated current (TSC), evaluates the current generated by charge carriers being thermally emitted [171]. An isothermal variation of the electric field allows the investigation of tunneling emission [34]. In addition to these techniques, the data evaluation techniques have undergone further development. The lock-in weighting function and the inverse-Laplace transformation permit a more detailed description of the energetic levels [107, 172].

Since its proposal DLTS has evolved into a standard technique for characterising deep levels in semiconductors. The technique has been successfully applied to both deep level traps and SAQDs. For deep level traps it has been used to investigate widely used semiconductor materials such as gallium arsenide (GaAs) [173, 174], silicon (Si) [175, 176] or beta-gallium oxide ( $\beta - \text{Ga}_2\text{O}_3$ ) [177]. The binding energies of SAQDs, grown with different materials, e.g. InP [29] or GaSb [178]. The studies further explored the behaviour of the energetic levels under different conditions, such as charge state or applied magnetic fields [35, 37].

This thesis employs the temperature and the isothermal bias voltage dependent capacitance spectroscopy. The following section presents the work principle of temperature dependent DLTS and the data evaluation methods of boxcar and lock-in weighting functions.

---

### 3.1 Work principle

A bias pulse is applied to the sample. This pulse consists of a preparation voltage  $V_p$  and a measurement voltage  $V_m$ .  $V_p$  is chosen so that the depletion region shrinks and the deep level traps can be filled with electrons.  $V_m$  expands the depletion region so that electron recapture can be neglected and only the emission process is dominant. The occupied deep level traps within the depletion region of the junction can now emit their electrons by tunneling, thermal-assisted tunneling, thermal emission or optical emission, as previously outlined in section 1.3. The emission process is represented by a time dependent capacitance transient, as described in section 1.4.3. A series of capacitance transients is now recorded at different temperatures. With rising temperature the thermal emission rate increases and the lifetime of the capacitance transients decreases. To distinguish between potentially multiple types of deep level traps the transients are analysed with the help of a weighting function  $w(t)$ . The filtered signal  $S(T)$  reads [179]

$$S(T) = \int_0^{\infty} C(t,T)w(t)dt. \quad (3.1)$$

### 3.2 Boxcar weighting function

In the original proposal by Lang [26] the so-called *Boxcar method* was employed. The weighting function is given by

$$w(t) = \delta(t_1 - t) - \delta(t_2 - t) \quad (3.2)$$

where  $t_1$  and  $t_2$  are two timepoints chosen during the measurement phase of the bias pulse, with the Dirac's delta distributions  $\delta(t)$ . The difference between the timepoints is often considered as the time window  $P = t_2 - t_1$ . The set of capacitance transients is analysed with this weighting function, as exemplified in figure 3.1.

Under the assumption of a single emission rate, it can be shown that the DLTS signal  $S$  attains its maximum when the apparent lifetime  $\tau$  of the emission process matches

$$\tau_{max} = \frac{t_1 - t_2}{\ln(t_1/t_2)}. \quad (3.3)$$

For one combination of  $t_1$  and  $t_2$  the  $T_{max}$  and  $\tau_{max}$  had been found. By selecting another value for  $t_2$ , equivalent to selecting a different time window  $P$ , the temperature of the maximum position shifts correspondingly. By rearranging the thermal emission formula 1.12 one obtains [166]

$$\ln(\tau T^2) = -\ln\left(\sigma \cdot g(2\pi)^{3/2} k_B^2 \frac{m^*}{h^3}\right) + \frac{E_b}{k_B T}. \quad (3.4)$$

A logarithmically aligned plot of  $\tau_{max} T_{max}^2$  against the inverse of the temperature generates the so-called *Arrhenius plot*. The slope is proportional to the binding



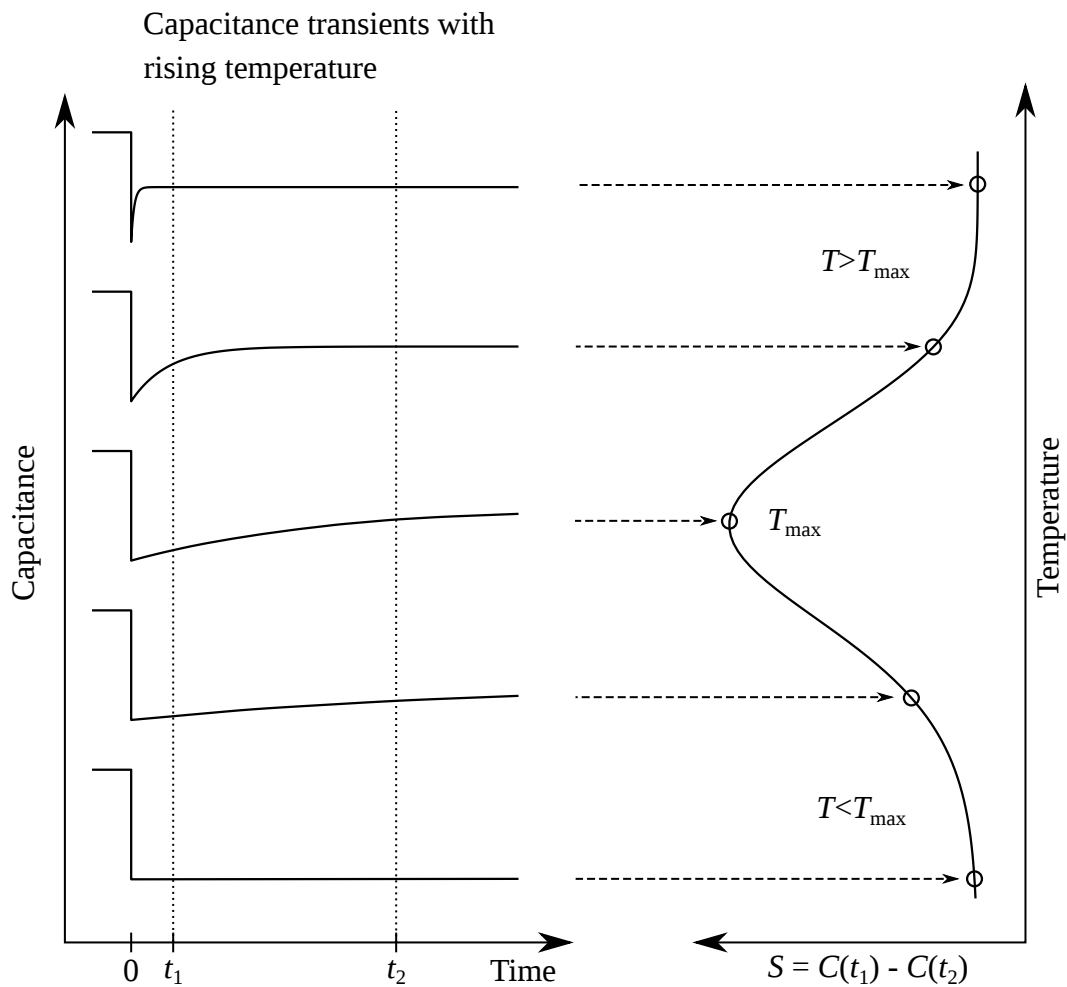


Figure 3.1.: Schematic illustration of temperature dependent capacitance transients together with their evaluation using the Boxcar method. Adapted from Ref. [26].

energy while the capture cross section can be extracted from the  $y$ -axis intersection. It has to be noted that other processes like thermal assisted tunneling [107] or re-capture by e.g. leakage current [65] can influence this plot significantly.

### 3.3 Lock-in weighting function

In order to improve the signal-to-noise ratio another approach has been presented, namely the lock-in weighting function [172]. For the experiments conducted throughout this thesis, it has been found that this approach represents a good compromise

between sensitivity, time-resolution and signal quality. For a given time window  $P$  the weighting function is given by

$$w(t) = \frac{1}{P} \cdot \begin{cases} +1 & 0 \leq t \leq P/2 \\ -1 & P/2 < t \leq P \\ 0 & \text{else.} \end{cases} \quad (3.5)$$

It is common practise in the literature to exclude the first portion of the transient, up to a time  $t_d$ . It is possible that a bias pulse may induce responses from measurement devices or capacitance and inductance induced by cables, which would require the time  $t_d$  to settle. However, in the measurement setup employed throughout this thesis, this time is well below the resolution limit and can therefore be considered as  $t_d = 0$  s [166].

As described in section 2.1, the capacitance transients have been recorded by a digital oscilloscope, sampled with a well-defined time resolution  $\Delta t$ . The lock-in signal for these time-discrete capacitance transients over  $N_t$  data points reads

$$S(T) = \frac{1}{P} \left( \sum_{i=1}^{N_t/2} C(t_i, T) - \sum_{i=N_t/2+1}^{N_t} C(t_i, T) \right) \quad (3.6)$$

with  $P = N_t \Delta t$ . It has been demonstrated by Day et al. that the lock-in signal develops its maximum when the apparent lifetime of transient meets  $\tau_{max} = 0.424 \cdot P$  [180]. However, this was calculated for weighting with a physical lock-in amplifier. It had been shown in Ref. [166], that for the lock-in signal presented in formula 3.6, a maximum can rather be found at  $\tau_{max} = 0.398 \cdot P$ . Compared to the boxcar DLTS signal, the lock-in signal exhibits an improved signal-to-noise ratio, since more data points are evaluated. It has the drawback of a slightly poorer lifetime resolution [172].

The binding energy and the capture cross section can be determined in an analogous manner as with the boxcar weighting function, by means of an Arrhenius plot with equation 3.4.

---

## Chapter 4

# Capture dynamics of self-assembled quantum dots far from equilibrium

SAQDs are often separated by wide layers of material far from conducting channels in applications such as LEDs [8, 10], lasers [9] or information storage devices [41]. A detailed understanding of the electron capture and emission dynamics for such structures is thus important for their operation. The emission process of electrons from SAQDs far from their reservoir has been studied in detail under various conditions like charge state [37] of magnetic fields [35, 36] and temperature regimes [33, 107]. Conversely, measurements of the capture dynamics were often restricted to methods that require an nearby reservoir [24, 42] or indirect measurement where the emission as a function of a preceding capture process was investigated [32, 34]. Other measurements included optical approaches [44–46] or a direct electrical measurement in the thermal regime of the SAQDs [47]. Here, isothermal DLTS measurements were conducted on the sample presented in section 2.2.1 at various selected temperatures as low as 5 K. A quantitative model allowed the capture and emission rates to be separated, revealing an increase in the capture rate with increasing bias voltage as well as an apparent thermally activated origin of the capture mechanism. *Paper I* focuses on the well known hysteretic capacitance voltage characteristic of SAQDs embedded in a Schottky junction, which is relevant for information storage devices [41, 48–52]. The hysteresis originates from the different amount of charge stored in the SAQDs during up- and down-sweeps of the bias voltage, resulting in capacitance traces whose shape depends on the sweep settings. Capture and emission rates determined by isothermal DLTS were used to model this hysteresis with good agreement. *Paper II* identifies the back contact as the main source of electrons for the capture. A model is established where electrons diffuse from their reservoir over a barrier before being captured into the SAQDs. The capture dynamics are thus influenced by the charge state of the SAQDs, as the electrons residing in the SAQDs create an additional potential hub for subsequent electrons. Additional isothermal DLTS experiments were carried out at low temperatures under an applied magnetic field, revealing a tunneling contribution to the capture under suitable conditions, especially for small barriers.

---

## 4.1 Paper I

### Reference

L. Schnorr, O. Khoukhi, L. Berg, T. Heinzl, C. Rothfuchs-Engels, S. Scholz, A. Ludwig, and A. D. Wieck Phys. Rev. B **104**, 205310 (2021)  
DOI: <https://doi.org/10.1103/PhysRevB.104.205310>  
©2021 American Physical Society




### Copyright statement

The author has the right to use the article or a portion of the article in a thesis or dissertation without requesting permission from APS, provided the bibliographic citation and the APS copyright credit line are given on the appropriate pages.

### Contributions

I participated in data evaluation and contributed to manuscript writing.

## Hysteretic capacitance-voltage characteristics of self-assembled quantum dots far from equilibrium with their environment

L. Schnorr , O. Khokhi, L. Berg , and T. Heinzel \**Solid State Physics Laboratory, Heinrich-Heine-Universität Düsseldorf, 40204 Düsseldorf, Germany*C. Rothfuchs-Engels,<sup>†</sup> S. Scholz, A. Ludwig , and A. D. Wieck *Lehrstuhl für Angewandte Festkörperphysik, Ruhr-Universität Bochum, 44780 Bochum, Germany*

(Received 22 September 2021; revised 15 November 2021; accepted 16 November 2021; published 29 November 2021)

Capacitance-voltage measurements on self-assembled quantum dot layers exposed to strong electric fields and with large distances to the reservoirs show a marked hysteretic behavior. It is shown that at low temperatures this hysteresis can be explained quantitatively in terms of state-dependent capture and emission rates that are obtained by a rate equation model, applied to the measured capacitance transients. The occupation dynamics and the steady-state configuration can be extracted from these data via a Markov chain model.

DOI: [10.1103/PhysRevB.104.205310](https://doi.org/10.1103/PhysRevB.104.205310)

### I. INTRODUCTION

Self-assembled quantum dots (SAQDs) are quasi-zero-dimensional semiconductor islands embedded in a crystalline semiconductor host [1,2]. Due to the electronic band offsets, they are capable of capturing, storing, and re-emitting electrons or holes, respectively. SAQDs have been of great scientific interest over the past three decades due to their versatility for fundamental research [3–6] as well as because of their application potential [7]. SAQDs are used routinely in semiconductor optoelectronics, in particular in quantum dot lasers [8,9], single photon sources [10], and light-emitting diodes [11]. Regarding all-electronic applications like memory cells [12–14] or memristors [15], it is well known that the charging/discharging dynamics of SAQDs can generate hysteretic behavior as a function of a bias voltage [16–22], detectable, for example, in the capacitance of the structure [21–24] or in the conductance of a nearby conductive channel, on which the SAQDs act as a floating gate [14,18–20,22,25–29]. Charging/discharging times of 600 ps have been reported [30], while the storage time depended strongly on the temperature and can reach values of  $10^4$  s at a temperature of 180 K [13]. The markedness of the hysteresis depends, in general, on the modifications of the potential landscape accompanied by the electron transfer [28,31]. For several experiments, these modifications were described qualitatively and with high plausibility [18,19,21–24]. However, to understand these hysteretic effects in more detail, a quantitative description is desirable. In particular, it is important to be able to determine the capture and emission rates of the SAQD states as a function of the external parameters. Such information can be useful not only to explain certain phenomena in more detail, like the inversion of the hysteresis orientation above

a threshold bias [32] or nontrivial shapes of hysteresis loops [20], but also to improve characteristic values, for example, the limits for ultrafast charging of SAQDs [33], relevant for single-photon sources.

Here, we present an experimental concept which allows the determination of the bias voltage-dependent (and temperature-dependent) capture and emission rates of the SAQD states that take part in the hysteresis. The SAQDs are in states far from equilibrium with the environment due to the strong electric field and large distances to reservoirs prevent corresponding elastic electron transfers. Such a layout is typical for memory devices as well as for optoelectronic applications. Deep level transient spectroscopy (DLTS, [34]), a well-established technique in the field [35–44], is used in its version of *Lock in-DLTS* [45], as an excellent compromise between high-energy resolution and acceptable measurement times. A rate equation model allows to extract the electron transfer rates of the participating states from the measured capacitance transients. From these rates, the average electron occupation numbers of the SAQDs as a function of time are determined. They not only provide an explanation in terms of the corresponding depletion region width  $z_d$ , but also describe the measured hysteresis loop quite well and allow the prediction of the steady-state configuration in the limit of negligible voltage sweep rates.

In Sec. II, the sample and the experimental methods are described. Section III reports the DLTS measurements, which are analyzed within the rate equation model in Sec. IV. These results are used in Sec. V for the modeling and explanation of the capacitance voltage hysteresis, and in Sec. VI for calculating the steady state. The paper concludes with a summary and an outlook (Sec. VII).

### II. EXPERIMENTAL SETUP AND MEASUREMENT TECHNIQUES

The sample structure and the measurement technique were described in detail elsewhere [43,44]. In brief, we use a

\*thomas.heinzel@hhu.de

<sup>†</sup>Present address: DESY, Notkestrasse 85, 22607 Hamburg, Germany.

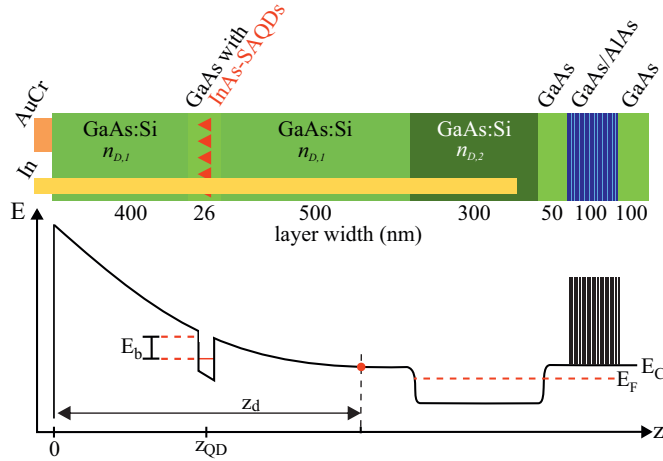


FIG. 1. Top: Cross-sectional schematic view of the sample layout. The SAQD layer is indicated by the red triangles. The back electrode is accessed via an alloyed In contact, and the top gate is formed by a Cr/Au electrode. Silicon doping densities are indicated by  $n_{D,1}$  and  $n_{D,2}$ . Bottom: Schematic band diagram for the case of a negative voltage applied to the top gate with respect to the grounded back electrode, including our conventions for the quantities of relevance. The width of the depletion layer is denoted by  $z_d$ .

GaAs/AlAs heterostructure as a model system, grown by molecular beam epitaxy, with a SAQD layer 500 nm above a  $\text{Si}^+$ -doped back contact and 426 nm below the sample surface, see Fig. 1(a). The InAs SAQDs have a sheet number density of  $n_{QD} = 10^{14} \text{ m}^{-2}$  and are embedded in a 26-nm layer of undoped GaAs. Bias voltages can be applied between a square Cr/Au top electrode (edge length 0.3 mm) and the back electrode, which is accessed via an alloyed In contact. The densities of the Si doping in the spacer layers are  $n_{D,1} = 6.02 \times 10^{21} \text{ m}^{-3}$  and  $n_{D,2} = 2 \times 10^{24} \text{ m}^{-3}$ . The active sample area covers approximately  $9 \times 10^6$  quantum dots.

The sample is inserted into a liquid helium cryostat with a temperature range from 3 K to 300 K. DC bias voltages are applied to the top gate with respect to the back contact, kept at virtual ground via a HF2TA transimpedance amplifier ( $Z = 1 \text{ k}\Omega$ ) from Zurich Instruments, the output of which is fed into a Zurich Instruments HF2LI lock in amplifier. The voltage pulses are generated using a Keithley Model 3390 arbitrary waveform generator with a transition time of 100 ns and are superimposed to the AC test voltage generated by the lock in amplifier. Thus, the output current obtained at a phase shift of  $\pi/2$  with respect to the input AC voltage detects the differential capacitance of the sample.

### III. EXPERIMENTAL RESULTS

#### A. Capacitance-voltage measurements and their temperature dependence

Multiple capacitance-voltage sweeps between  $V = -4 \text{ V}$  and  $V = +0.3 \text{ V}$  were recorded at various temperatures between  $T = 7 \text{ K}$  and room temperature. For each temperature both the up- and down-sweeps were measured. The bias voltage step size was  $\Delta V = 12.5 \text{ mV}$  with a waiting time of  $\Delta t = 0.85 \text{ s}$  and the capacitance was measured via a test

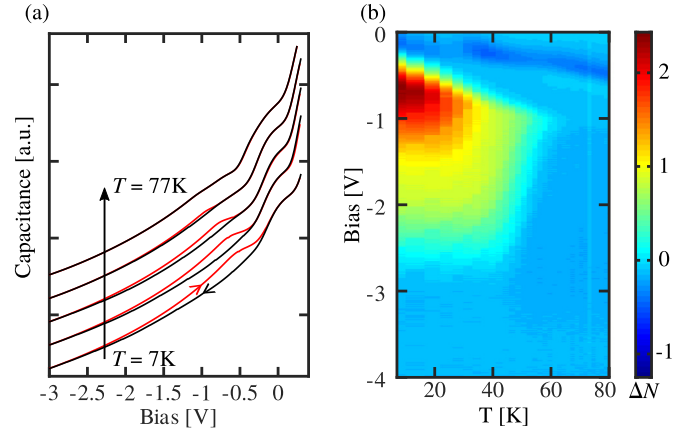


FIG. 2. (a) Capacitance-voltage hysteresis as a function of temperature with red and black lines corresponding to the up- and down-sweeps, respectively. The temperature values are (from bottom to top)  $T = 7 \text{ K}$ , 22 K, 33 K, 52 K, and 77 K. Adjacent traces are offset vertically for clarity. (b) Difference of the number of electrons stored per SAQD between the up- and down-sweep as a function of the bias voltage and temperature.

signal with an amplitude of  $V_{ac} = 10 \text{ mV}$  and a frequency of  $f_{ac} = 10.44 \text{ MHz}$ . The lock in time constant was set to  $\tau = 20.33 \text{ ms}$ . A selection of these traces is shown in Fig. 2(a).

As the bias voltage is increased from  $V = -4 \text{ V}$  to  $V = +0.3 \text{ V}$  at  $T = 7 \text{ K}$  [lower-most trace in Fig. 2(a)], two peaks can be observed on top of the smooth voltage dependence expected for a Schottky diode capacitance, one at  $V \approx -0.6 \text{ V}$  and a second one at  $V = 0 \text{ V}$ . In the successive down-sweep, however, only the peak at  $V = 0 \text{ V}$  is observed, while the second one is absent. A similar behavior was reported in earlier work [13,24,46]. This hysteretic behavior is the main focus of the present work.

As the temperature is increased, both features shift towards lower bias voltages. The hysteretic peak becomes weaker until it vanishes at about  $T = 60 \text{ K}$ . The nonhysteretic peak, however, becomes more pronounced as the temperature is increased up to  $T \approx 150 \text{ K}$  above which its shape and position remain essentially unchanged (not shown).

In Fig. 2(b), the difference  $\Delta N$  in the number of electrons stored per SAQD between the up- and down-sweeps is shown as a function of the bias voltage and the temperature, see Sec. V for details. The maximum hysteresis opening thus corresponds to a charge difference of more than two electrons per SAQD at low temperatures. Qualitatively, its origin can be described as follows [24]. At sufficiently negative bias voltages  $V$  the SAQDs are empty. As  $V$  is increased, the width  $z_d$  of the space charge layer decreases according to  $z_d = \sqrt{\frac{2\epsilon\epsilon_0}{en_D}(V_{bi} - V)}$ , where  $V_{bi}$  is the built-in voltage and  $e$  denotes the elementary charge. This leads to an increase of the capacitance according to  $C = \epsilon\epsilon_0 A/z_d$ , where  $A$  denotes the area underneath the top gate, which causes the smooth increase of  $C$  with  $V$ . Above a threshold voltage, electrons are captured at a significant rate by the SAQDs, leading to an average electron number  $N$  per SAQD. This causes an increase of  $z_d$  since these electrons have to be compensated

by additional positively charged donor ions [46]

$$z_d(N) = \sqrt{\frac{2}{en_D} [\epsilon\epsilon_0(V_{bi} - V) + Nen_{QD}z_{QD}]} \quad (1)$$

As a consequence, the capacitance decreases to  $C = \epsilon\epsilon_0 A/z_d(N)$  when the steady state is reached. During our up-sweeps and in the hysteresis interval, however, the sweep rate is comparable to or larger than the smallest charge transfer rate, and the steady state has not yet been reached. Consequently, a larger capacitance as compared to the steady-state value is measured. Likewise, in a down-sweep, the measured capacitance can be smaller than its steady-state value. Therefore, one expects to observe characteristic capacitance transients in response to voltage steps with positive (negative) sign for negative (positive) voltage steps and with time constants that depend on the capture and emission rates of the participating SAQD states. As we will show below, the relation between the time constants of the transients and the state-dependent electron transfer rates is nontrivial but explains the hysteresis in quantitative terms.

### B. Lock in: DLTS measurements

We determine the electron transfer rates from capacitance transients of the sample in response to abrupt voltage steps. The transients are characterized by lock in–DLTS measurements at four selected temperatures, namely at  $T = 7$  K, 16 K, 41 K, and 77 K. Measurement voltages  $V_m \in [-3.0$  V, 0 V] were applied after preparation voltages  $V_p$ . Each voltage was applied for a time interval  $t_p = t_m = 498$  ms. Measurements were recorded for combinations of  $V_p$  and  $V_m$  over the measurement interval with a voltage step size of  $\Delta V = 40$  mV. Afterwards, the lock in signal  $S(V_p, V_m)$  was calculated according to

$$S(V_p, V_m) = \sum_{i=1}^{N_t/2} C(t_i, V_p, V_m) - \sum_{i=N_t/2+1}^{N_t} C(t_i, V_p, V_m), \quad (2)$$

where  $N_t$  is the number of time samples in the recorded transient. Thus, the lock in signal represents the difference of the areas in the first and the second half of the transient. It approaches zero for time constants much smaller or much larger than the measurement window and shows a maximum for a time constant of  $\approx 40\%$  of the evaluated recording time [44]. The results are shown in Fig. 3.

At  $T = 7$  K, three clearly separated negative emission peaks can be observed at  $V_p > -0.5$  V for  $V_m \approx -2.55$  V,  $V_m \approx -1.2$  V, and  $V_m \approx -0.4$  V. All emission peaks are approximately symmetric with respect to  $V_m$ . For  $V_p < -0.5$  V, electron capture can be observed via a positive lock in–DLTS signal at  $V_m \approx (-0.4 \pm 0.1)$  V. Outside of the transition region from electron emission to capture at  $V_p \approx -0.5$  V the emission peaks do not exhibit any dependence on  $V_p$ . The capture peak, however, shows a step-like dependence on  $V_p$  on its border towards smaller  $V_m$  with two steps occurring at approximately  $V_p = -1.25$  V and  $V_p = -2.4$  V.

At  $T = 16$  K, the features remain qualitatively unchanged, with the capture and emission signals at the largest  $V_m$  values shifting towards smaller  $V_m$ . The transition region between the capture and emission regimes has decreased to  $V_p \approx -0.6$  V.

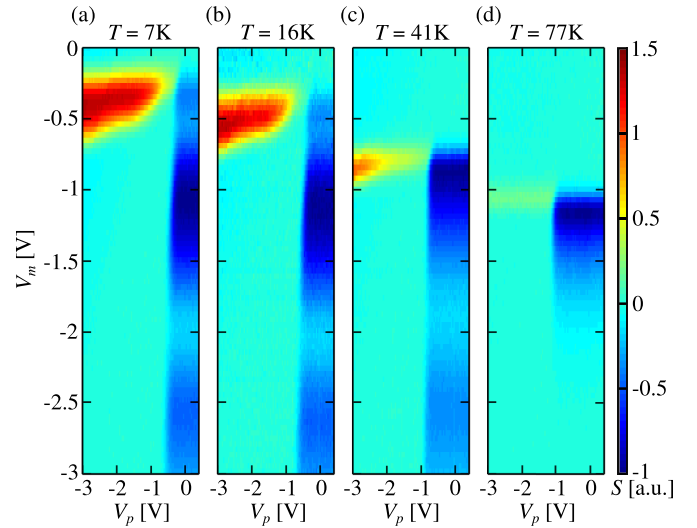


FIG. 3. Lock in–DLTS measurements at  $T = 7$  K, 16 K, 41 K, and 77 K (a)–(d). The colorscale value of each spectrum is scaled to  $-1$  at its respective minimum.

At  $T = 41$  K, however, the changes are more pronounced: only two emission peaks can be observed, a large one that is asymmetric with respect to  $V_m$  as well as an approximately symmetric one centered at  $V_m \approx -2.55$  V, separated by a minimum at  $V_m \approx -0.9$  V. The capture signal is significantly weaker compared to those at lower temperatures and now covers the interval  $V_m \in [-1$  V,  $-0.75$  V]. A slight dependence of its low-voltage edge on  $V_p$  can still be observed, but the resolution is too small to identify the steps here. The transition region between the capture and emission regimes has shifted downwards to  $V_p \approx -0.9$  V.

Only one asymmetrical emission signal can be observed at  $T = 77$  K, which has its minimum at  $V_m \approx -1.2$  V. A relatively weak capture signal at  $V_m \approx -1.05$  V can still be detected. Neither the capture nor the emission peaks show a  $V_p$  dependence outside the transition region that has now shifted to  $V_p \approx -1$  V.

Thus, a monotonous behavior of the temperature dependence is observed: as the  $T$  increases, the capture signal becomes less pronounced compared to the strongest respective emission peak, while its position moves in the direction of smaller  $V_m$ . The transition region between electron capture and emission shifts towards smaller  $V_p$  as  $T$  is increased. The fine-structure of both the capture and emission signals smear out as  $T$  increases. Furthermore, no emission signals can be observed at measurement voltages larger than the upper boundary of the capture structure on the  $V_m$  axis.

In the following, we restrict ourselves to an analysis of the situation at the lowest temperature, where the richest structure is observed and the emission occurs by elastic tunneling only. A quantitative discussion of the behavior at larger temperatures, where thermally activated processes are significant, is beyond our scope here and will be provided elsewhere.

### IV. RATE EQUATION MODEL

To analyze quantitatively the observed lock in–DLTS signals taken at  $T = 7$  K, we proceed by modeling the charge



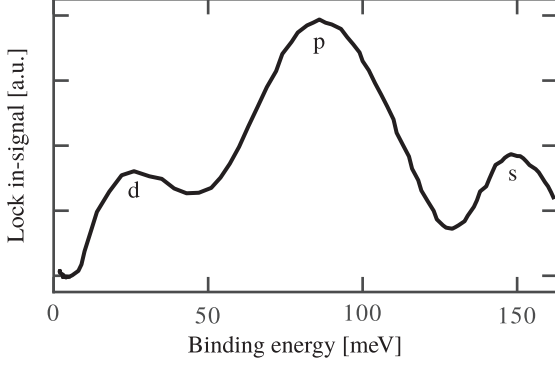


FIG. 4. Energy spectrum obtained from the emission features observed at  $T = 7$  K, calculated via Eq. (3).

transfer dynamics by a system of coupled differential equations [47].

### A. Rate equations for the electron transfer dynamics

Based on previous measurements on the same sample [43] we attribute the emission feature observed at  $V_m \approx -2.6$  V at  $T = 7$  K to electron emission from the  $s$ -states.

In analogy to the analysis described in Ref. [43], the energy spectrum can be calculated from the emission transients, but now at temperatures where elastic tunneling is dominant. Via the relationship derived by Korol *et al.* [48], the time constant of the capacitance transient is given by

$$\tau = \frac{4\sqrt{2m^*E_b}}{eF} \exp\left(\frac{4\sqrt{2m^*E_b}^{3/2}}{3e\hbar F}\right). \quad (3)$$

Here,  $E_b$  is the binding energy of the captured electrons (see also Fig. 1) and  $F$  denotes the electric field at the SAQD layer. The spectrum shown in Fig. 4 can be obtained by taking a line scan through the lock in–DLTS colorscale plot, Fig. 3(a), at  $V_p = 0$ . The voltage dependence in the obtained spectrum  $S(V_m)$  can be converted into an electric field-dependent spectrum  $S(F)$  via the voltage-dependent band structure of the sample as obtained from a one-dimensional Poisson-Schrödinger solver [49]. This electric field dependence is then converted into energy and presented in Fig. 4 by solving numerically Eq. (3) for the binding energy  $E_b$  with  $\tau = \text{const.} = 0.398 \cdot t_m = 198$  ms, fixed by our transient recording time and the rate window of lock in signal.

The large energy spacing of  $\approx 60$  meV between the peaks, as well as their relative magnitude indicate that they originate from the  $s$  (smallest  $V_m$ ),  $p$ , and  $d$  (largest  $V_m$ ) states. Sublevels like  $s_1, s_2, p_1$ , and so on cannot be resolved here. We therefore assume that the step-like structure of the capture peak arises from a superposition of three different capture paths, one for the  $s$ ,  $p$ , and  $d$  states each. This gives rise to the system of coupled differential equations:

$$\dot{w}_0 = -c_{0s} \cdot w_0 + r_{s0} \cdot w_s, \quad (4)$$

$$\dot{w}_s = -c_{sp} \cdot w_s + r_{ps} \cdot w_p + c_{0s} \cdot w_0 - r_{s0} \cdot w_s, \quad (5)$$

$$\dot{w}_p = +c_{sp} \cdot w_s - r_{ps} \cdot w_p + r_{dp} \cdot w_d - c_{pd} \cdot w_p, \quad (6)$$

$$\dot{w}_d = +c_{pd} \cdot w_p - r_{dp} \cdot w_d, \quad (7)$$

TABLE I. Fit parameters used to calculate the results shown in Figs. 5(b), 5(c), and 6.

$x$	$y$	$m_{xy} [\text{V}^{-1}]$	$n_{xy}$	$m_{yx} [\text{V}^{-1}]$	$n_{yx}$
0	s	13.53	8.63	-6.15	-14.08
s	p	16.18	7.71	-4.97	-4.16
p	d	15.68	6.35	-16.66	-2.91

where  $w_0$  is the probability for one SAQD being empty, while  $w_j$  is the probability that state  $j$  and all states at lower energies are occupied, while all states with larger energies are empty. The capture and emission rates related to these occupation probabilities are denoted by  $c_{ij}$  and  $r_{ij}$ ,  $i, j \in \{0, s, p, d\}$ , respectively.

The total, time-dependent occupation number per dot is then given by

$$N(t) = 2 \cdot w_s(t) + 6 \cdot w_p(t) + 12 \cdot w_d(t). \quad (8)$$

Here, the weighting factors rely on the assumption that all sublevels of each SAQD state, e.g., the  $p$  state, share the same occupancy for all times. Other reasonable assumptions are possible as well which, however, cause only marginal changes of the fit parameters discussed below (not shown).

### B. Fit of the experimental transients

We proceed by fitting the rate equation model to the data using a similar approach as reported earlier [44], where the choice of the initial conditions for the differential equations and the simulation of the pulse sequences are kept the same. The individual electron transfer rates are modeled by

$$c_{xy}(V) = \exp(m_{xy} \cdot V + n_{xy}) s^{-1}, \quad (9)$$

$$r_{yx}(V) = \exp(m_{yx} \cdot V + n_{yx}) s^{-1}, \quad (10)$$

where  $x, y \in \{0, s, p, d\}$ .

The lock in signal is calculated via Eq. (2) from the total charge per dot under the assumption that  $\text{red } \Delta C(t) \propto N(t)$ . The constants  $m_{xy}$  and  $n_{xy}$  are the fit parameters, alongside a scaling factor that accounts for the proportionality between  $N(t)$  and  $\Delta C(t)$ .

Equations (4) to (7) have no analytical solution. We thus solve them numerically for each iteration of the fitting process, using the RADAU solver of the SCIPY library [50] which implements a fifth-order implicit Runge-Kutta method [51].

To avoid excessive computation times, the calculated rates were limited to  $\leq 10^3 \text{ s}^{-1}$ . This cutoff is justified by the recording time of  $t_m = 498$  ms, which leads to a rate window of the lock in signal that is centered around  $r_{\text{ref}} = (0.398 \cdot t_m)^{-1} = 5.1 \text{ s}^{-1}$ , more than two orders of magnitude smaller.

The results of this fit algorithm are given in Table I, and the corresponding, numerically obtained lock in–DLTS signals are shown in comparison to the experimental data in Figs. 5(a) and 5(b). The resulting capture and emission rate functions are depicted in Fig. 5(c). Starting from a negative bias voltage, say  $V = -3$  V, all emission rates are large as compared to the capture rates, and the SAQDs are empty in a steady state. As  $V$  is increased, the emission rates decay exponentially while significant capture sets in around  $V = -1$  V. The capture rates



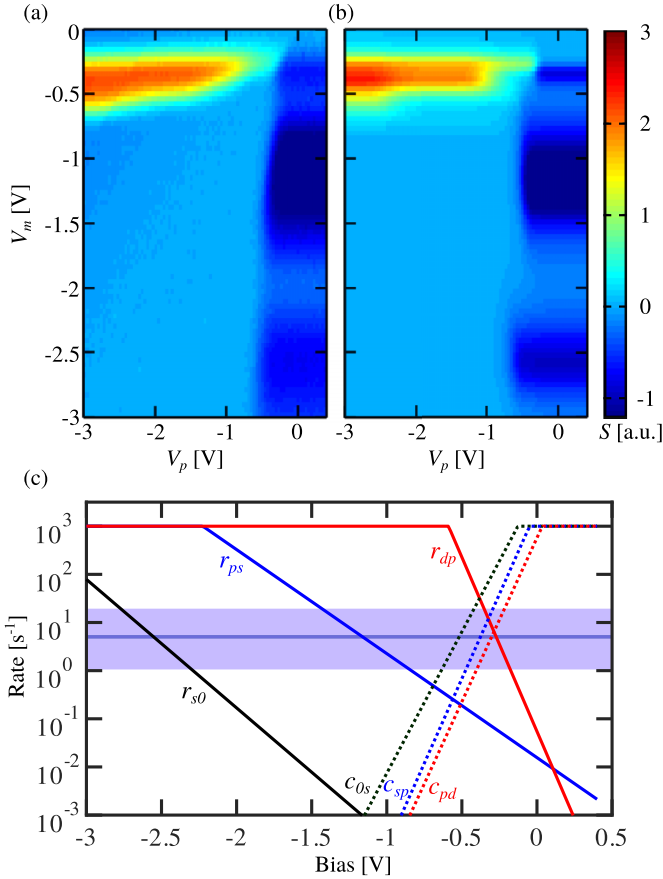


FIG. 5. (a) Measured and (b) calculated lock in-DLTS spectra for the measurement at  $T = 7$  K and the voltage-dependent electron transfer rates (c), as obtained from the fit.

increase exponentially with increasing bias voltage, leading to an occupied steady state, with an occupation probability  $w_j(V)$  (see below).

For the emission processes, the physical interpretation of the obtained fit parameters is straightforward: each exponential voltage dependence, parameterized by its two fit parameters, is an approximation to the general expression describing the emission dynamics, which in our case of  $T = 7$  K consists of pure tunneling, Eq. (3). This approximation is valid in the voltage interval in which the resulting emission rate falls within the rate window of  $r_{\text{ref}} = 5.1 \text{ s}^{-1}$  of our lock in-DLTS filter function. This value is denoted by the purple horizontal line in Fig. 5(c) alongside the corresponding full width at half maximum interval (indicated by the shaded area). We note that, only in this interval, our simple assumption of the respective rates as a function of the bias voltage needs to approximate the real dependence since outside this window the contribution to the measured signal is negligible. For the capture processes, we envisage a similar interpretation, but to the best of our knowledge, a model for the capture dynamics of electrons under the conditions present here is yet to be developed. It should be noted that the shape of the capture peak can only be reproduced accurately as long as  $c_s > c_p > c_d$ . Other scenarios lead to a qualitatively different shape (not shown). This may be indicative of the Coulomb barrier set up by the electrons already captured in the SAQDs, which (while

the system remains at the same bias voltage) suppresses the capture of further electrons. Thus, the dynamics of the capture processes cannot be dominated by the tunneling barrier width in our case. This finding is in contrast to the observations by Luyken *et al.* [52] who measured larger transfer rates for higher SAQD states which they were able to explain via the increased tunneling coefficient through the smaller potential barrier. Their measurements, however, studied each SAQD state at bias voltages where the respective state was aligned with the Fermi level in the back contact and the difference between charging and discharging times was negligible to a good approximation. Our measurements, however, are carried out with the states well above the bulk Fermi level and far from equilibrium with the environment, where capture and emission rates can differ by orders of magnitudes, see Fig. 5(c).

Based on these findings, we can now interpret qualitatively the behavior at higher temperatures. The shift of the capture peak towards smaller  $V_m$  in Fig. 3 with increasing temperature is indicative of increasing capture rates. Since they become larger as  $V$  is increased, the shift of the peaks towards more negative  $V_m$  compensates the increased thermal contribution, such that the combined rate still matches our experimental rate window. The same line of arguing is applicable to the emission peaks. The measured charge transfer rates are, however, composed of the individual transfer rates in a nontrivial way [44], where the observed decay rates are never smaller than each individual charge transfer rate. This explains the asymmetry of emission peaks close to the capture peaks in the lock in-DLTS spectra since, for larger  $V_m$  than the position of the capture peaks, there will always be a capture rate larger than any emission rate that will dominate the dynamics and make it too fast to be observable.

## V. APPLICATION TO THE CV HYSTERESIS

We continue by solving the system of differential Eqs. (4) to (7) using the previously determined fit parameters for the slowly varying bias voltage that was applied during the measurement of the CV hysteresis.

The system is solved numerically for two sweep cycles, each from  $V = +0.3$  V to  $V = -4$  V and back, with the initial condition that all SAQDs are completely filled. The bias voltage is stepped by  $\Delta V = \pm 12.5$  mV (depending on the sweep direction) every  $\Delta t = 0.85$  s. The calculation is considered to be finished when the solution has become independent of the initial condition.

From these simulations, the occupation probability of the SAQD states  $w_j(V)$  for the down- and up-sweep is obtained, where  $j \in \{0, s, p, d\}$ , leading directly to a computed value for  $\Delta N(V)$ . Experimentally,  $\Delta N(V)$  can be obtained from the measured CV hysteresis opening via the relation [46]

$$\Delta N = \frac{(\epsilon_0 \epsilon A)^2 n_D \cdot n_{QD}}{2z_{QD}} (C_{\text{down}}^{-2} - C_{\text{up}}^{-2}), \quad (11)$$

where  $A$  is the gate area and  $C_{\text{down(up)}}$  the capacitance in a down (up)-sweep.

The corresponding computed and experimentally determined results are compared in Fig. 6(a). Reasonable agreement is found, both with respect to its magnitude and

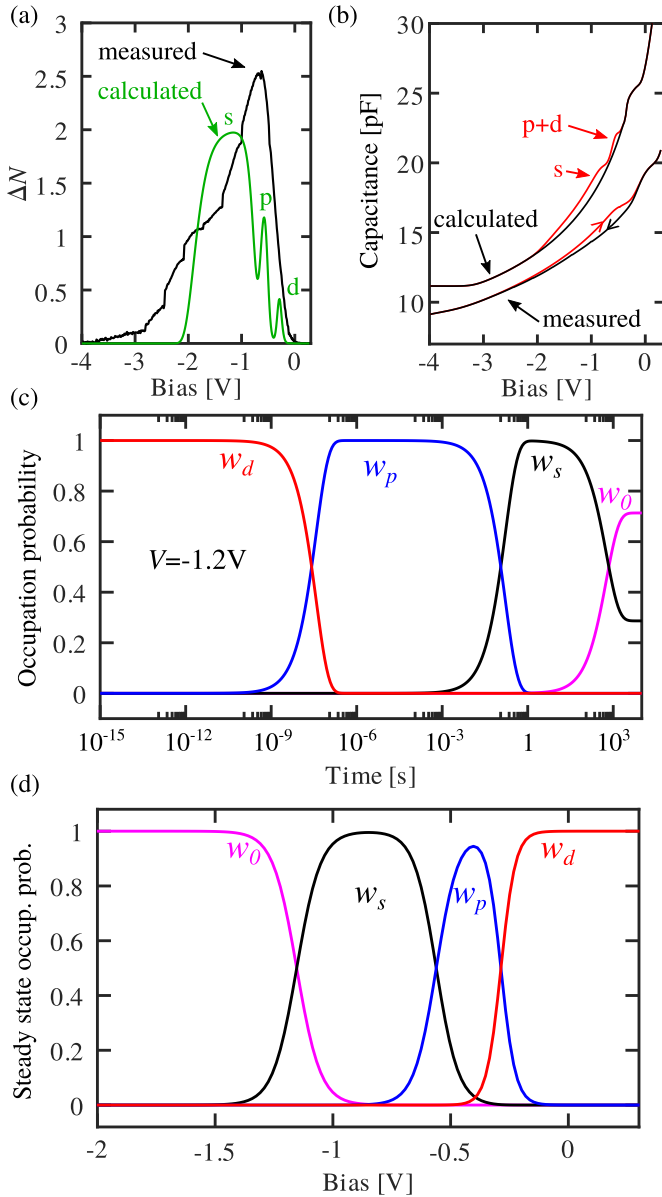


FIG. 6. Measured and calculated values for (a)  $\Delta N$ , (b) measured and calculated CV hysteresis, (c) time evolution towards the steady state at  $V = -1.2$  V, and the voltage dependence of the steady-state occupancy at (d)  $T = 7$  K.

its position along the bias voltage axis. In the calculation the contributions of the individual charge states can be resolved, whereas in the measurement, such an attribution is not possible. The assignment of the three features in the calculation to the individual charge states is obtained by setting the respective contribution of one state to zero and checking which feature vanishes. It is obvious that the  $s$  states form the largest contribution to the hysteresis, which seems plausible since their electron transfer rates are the smallest ones, they are thus affected most strongly by the varying bias voltage. For the  $p$  states, a small contribution is visible, while the participation of the  $d$  states, however, is close to be negligible since they can adapt sufficiently rapidly to the changed bias voltage.

To reproduce the CV characteristics of the down-sweep numerically, the band structure of the sample is solved in a

first step, using a one-dimensional Poisson and Schrödinger solver [49]. A doping density of  $n_{D,1} = 6.02 \times 10^{21} \text{ m}^{-3}$  as obtained from a  $C^{-2}(V)$  analysis of the measured down-sweep was used, and the SAQD layer was simulated by a 21-nm layer of InGaAs with a constant charge density. The result of this simulation for  $T = 7$  K is shown in Fig. 6(b) (upper black trace). It can be seen that the nonhysteretic shoulder at  $V \approx 0$  is reproduced simply by the different layered materials. By rearranging Eq. (11) we can obtain the capacitance of the up-sweep from the calculated down-sweep and the simulated charge difference between the sweeps. The result is shown in Fig. 6(b) (upper red curve). Good agreement with the measurement [lower traces in Fig. 6(b)] can be observed regarding the boundaries of the hysteresis on the voltage axis. Two separate peaks can be observed for the  $s$ - and  $p$ -state contributions in the simulation, which cannot be resolved in the measurement. The hysteresis due to the  $d$  states is completely invisible in the CV curve.

Thus, by the analysis presented above, the qualitative picture developed in Sec. III A can be quantified and interpreted in terms of the weight by which individual SAQD states contribute to the hysteresis via their capture and emission rates. The good agreement between the measurements and the model furthermore implies that changes of the electron transfer rates by variation of the occupation numbers of the SAQDs are of minor importance, albeit this effect may explain the remaining deviations between the model and the experiment. These effects are hard to quantify since this would require unreasonably many fit parameters in our model, or maybe even a three-dimensional treatment of the SAQD potential as a function of their occupation, which is beyond our present scope.

Under the assumption that the average charge density in the SAQD layer is small compared to the doping density, the maximum, normalized opening of the hysteresis trace can be approximated as [46]  $\Delta C/C_s = N n_{QD} z_{QD} / 2 \epsilon \epsilon_0 (V_{bi} - V)$ . Hence, the opening of this type of hysteresis can be maximized by increasing  $n_{QD}$  or  $z_{QD}$  to their upper limits and can be suppressed by corresponding minimizations.

As the temperature is increased, the transfer rates increase as well and the SAQDs come closer to their steady state during the time window  $\Delta t = 0.85$  s at each voltage. Thus, the hysteresis decreases and vanishes for our parameters at  $T \approx 60$  K, see Fig. 2(b). While for the model presented here, there is no analytical expression for the observable capacitance transient as a function of the individual rates, it is reasonable to assume that the combined rate can never be slower than any individual rate. Hence, the maximum sweep rate where no hysteresis can be observed can be estimated from our model by taking the slowest individual electron transfer rate for the  $s$  state at  $V \approx -1.2$  V, i.e.,  $r_{\min} \approx 10^{-3} \text{ s}^{-1}$  for  $T = 7$  K, as the limiting factor.

## VI. CALCULATION OF THE STEADY-STATE CONFIGURATION

The experimentally determined electron transfer rates can be used as input for a continuous time [53] Markov chain [54] model, with the goal to obtain the steady-state configuration, which may be inaccessible experimentally, for example, due

to the required slow voltage sweep rates. In this picture, the states of the Markov chain correspond to the charge states ( $0, s, p, d$ ) of the SAQDs in that particular order, and we can therefore define the corresponding transition rate matrix [53] for each bias voltage as

$$Q = \begin{pmatrix} -c_{0s} & c_{0s} & 0 & 0 \\ r_{s0} & -(r_{s0} + c_{sp}) & c_{sp} & 0 \\ 0 & r_{ps} & -(r_{ps} + c_{pd}) & c_{pd} \\ 0 & 0 & r_{dp} & -r_{dp} \end{pmatrix}, \quad (12)$$

from which the occupation numbers follow via

$$P(t) = \exp(Qt), \quad (13)$$

and thus the steady-state configuration follows according to

$$P = \lim_{t \rightarrow \infty} \exp(Qt), \quad (14)$$

which was evaluated numerically using GNU OCTAVE [55].

Figure 6(c) shows, as an example, the time evolution of the system from an initial state where all SAQD states are occupied, i.e., at  $V = 0$ , towards its steady-state configuration at  $V = -1.2$  V where the  $s$  states have equal capture and emission rates. It can be seen that the  $d$  states have a lifetime of the order of microseconds while the  $s$  states decay on the order of seconds. In general, we observed a convergence towards the steady state after, at most, 6000 s for the voltage range studied here. Calculation examples for further scenarios are given in the Supplemental Material [56].

Thus, to measure a steady-state CV of our system at  $T = 7$  K, one would have to wait at least  $t = 6000$  s between each voltage step which makes such an experiment impractical. Therefore, the numerical determination of the steady-state occupation probability represents a valid alternative. Here, the voltage-dependent steady-state configuration was calculated by approximating the limit in Eq. (14) by setting  $t = 10^7$  s. In the steady-state configuration the rows of  $P$  are identical and the columns correspond to the occupation probability of the corresponding SAQD state. For our system this result is shown in Fig. 6(d). It can be seen that for  $V < 1.5$  V the SAQDs are empty. For  $V < -0.9$  V only the  $s$  states contribute to the filling factor whereas for  $V < -0.5$  V both the  $s$  and the  $p$

states are contributing. Only for  $V > -0.5$  V do the  $d$  states begin to be filled with electrons.

## VII. SUMMARY AND OUTLOOK

The hysteretic capacitance-voltage characteristics of self-assembled quantum dot layers with large distances to reservoirs and in strong electric fields was measured and the charge transfer dynamics was analyzed within a rate equation model. It has emerged how the hysteresis is determined by the capture and emission rates of the SAQD states, which were obtained via lock-in-DLTS. Reasonable quantitative agreement of the experimentally observed and calculated hysteresis traces as well as of the measured and calculated electron occupation numbers is found for all temperatures. The evolution of these rates as a function of the bias voltage supports an intuitive picture for the origin of the hysteresis, namely a time-dependent change of the width of the depletion region that forms between the top gate and the back electrode. Changes of the electron transfer rates by the local potential close to the SAQDs, on the other hand, appear to be of minor relevance in our system, but may be responsible for the residual deviations of the model to the experimental data. It has also been shown how these rates can be used to model the steady-state configuration, which may be inaccessible experimentally. Furthermore, the state-resolved capture rates have been measured, revealing that lower-lying states have larger capture rates, as one might expect from energetic considerations. The developed methodology is quite universal and can be applied to a variety of related scenarios, like storage of holes in SAQDs, different material systems, or the effect of the SAQD occupation number on the conductance of a nearby electron gas, as long as the relevant transfer rates lie within the experimentally accessible rate window. Hopefully, our studies inspire future work towards a better understanding of such systems, in particular regarding the electron capture process.

## ACKNOWLEDGMENTS

Computational support and infrastructure was provided by the ‘‘Centre for Information and Media Technology’’ (ZIM) at the University of D usseldorf (Germany). C.R., S.E.S., A.D.W., and A.L. gratefully acknowledge support of TRR 160/2-Project B04, DFG 383065199, and the DFH/UFA CDF A-05-06.

[1] D. Leonard, M. Krishnamurthy, C. M. Reeves, S. P. Denbaars, and P. M. Petroff, *Appl. Phys. Lett.* **63**, 3203 (1993).  
 [2] P. M. Petroff, A. Lorke, and A. Imamoglu, *Phys. Today* **54**, 46 (2001).  
 [3] P. Michler, A. Kiraz, C. Becher, W. V. Schoenfeld, P. M. Petroff, L. Zhang, E. Hu, and A. Imamoglu, *Science* **290**, 2282 (2000).  
 [4] M. Kroutvar, Y. Ducommun, D. Heiss, M. Bichler, D. Schuh, G. Abstreiter, and J. J. Finley, *Nature (London)* **432**, 81 (2004).  
 [5] C. L. Salter, R. M. Stevenson, I. Farrer, C. Nicoll, D. A. Ritchie, and A. J. Shields, *Nature (London)* **465**, 594 (2010).

[6] A. Faraon, A. Majumdar, D. Englund, E. Kim, M. Bajcsy, and J. Vuckovic, *New J. Phys.* **13**, 055025 (2011).  
 [7] D. J. Mowbray and M. S. Skolnick, *J. Phys. D: Appl. Phys.* **38**, 2059 (2005).  
 [8] V. M. Ustinov, N. A. Maleev, A. E. Zhukov, A. R. Kovsh, A. Y. Egorov, A. V. Lunev, B. V. Volovik, I. L. Krestnikov, Y. G. Musikhin, N. A. Bert, P. S. Kopev, and Z. I. Alferov, *Appl. Phys. Lett.* **74**, 2815 (1999).  
 [9] E. U. Rafailov, M. A. Cataluna, and W. Sibbett, *Nat. Photon.* **1**, 395 (2007).  
 [10] S. Buckley, K. Rivoire, and J. Vučkovi c, *Rep. Prog. Phys.* **75**, 126503 (2012).

- [11] I. L. Krestnikov, N. A. Maleev, A. V. Sakharov, A. R. Kovsh, A. E. Zhukov, A. F. Tsatsulnikov, V. M. Ustinov, Z. I. Alferov, N. N. Ledentsov, D. Bimberg, and J. A. Lott, *Semicond. Sci. Technol.* **16**, 844 (2001).
- [12] M. Geller, A. Marent, T. Nowozin, and D. Bimberg, *J. Phys. Cond. Mat.* **20**, 454202 (2008).
- [13] T. Nowozin, A. Marent, M. Geller, D. Bimberg, N. Akçay, and N. Öncan, *Appl. Phys. Lett.* **94**, 042108 (2009).
- [14] A. Marent, T. Nowozin, M. Geller, and D. Bimberg, *Semicond. Sci. Technol.* **26**, 014026 (2011).
- [15] P. Maier, F. Hartmann, M. Emmerling, C. Schneider, M. Kamp, S. Hofling, and L. Worschech, *Phys. Rev. Appl.* **5**, 054011 (2016).
- [16] K. Koike, K. Saitoh, S. Li, S. Sasa, M. Inoue, and M. Yanoa, *Appl. Phys. Lett.* **76**, 1464 (2000).
- [17] N. Ooike, J. Motohisa, and T. Fukui, *Jpn. J. Appl. Phys.* **46**, 4344 (2007).
- [18] C. R. Muller, L. Worschech, J. Heinrich, S. Höfling, and A. Forchel, *Appl. Phys. Lett.* **93**, 063502 (2008).
- [19] A. Marent, T. Nowozin, J. Gelze, F. Luckert, and D. Bimberg, *Appl. Phys. Lett.* **95**, 242114 (2009).
- [20] P. Maier, F. Hartmann, M. Emmerling, C. Schneider, S. Höfling, M. Kamp, and L. Worschech, *Appl. Phys. Lett.* **105**, 053502 (2014).
- [21] D. Nataraj, N. Ooike, J. Motohisa, and T. Fukui, *Appl. Phys. Lett.* **87**, 193103 (2005).
- [22] E. S. Kannan, G.-H. Kim, and D. A. Ritchie, *Appl. Phys. Lett.* **95**, 143506 (2009).
- [23] M. Geller, A. Marent, T. Nowozin, D. Bimberg, N. Akçay, and N. Öncan, *Appl. Phys. Lett.* **92**, 092108 (2008).
- [24] A. Gubanov, A. Schramm, V. Polojärvi, and M. Guina, *J. Phys. D: Appl. Phys.* **46**, 325102 (2013).
- [25] C. Balocco, A. M. Song, and M. Missous, *Appl. Phys. Lett.* **85**, 5911 (2004).
- [26] B. Marquardt, M. Geller, A. Lorke, D. Reuter, and A. D. Wieck, *Appl. Phys. Lett.* **95**, 022113 (2009).
- [27] M. Geller, B. Marquardt, A. Lorke, D. Reuter, and A. D. Wieck, *Nanoscale Res. Lett.* **5**, 829 (2010).
- [28] Y.-A. Liao, Y.-K. Chao, S.-W. Chang, W.-H. Chang, J.-I. Chyi, and S.-Y. Lin, *Appl. Phys. Lett.* **103**, 143502 (2013).
- [29] T. Nowozin, A. Beckel, D. Bimberg, A. A. Lorke, and M. Geller, *Appl. Phys. Lett.* **104**, 053111 (2014).
- [30] J. Nannen, W. Quitsch, S. Eliasson, T. Kummell, and G. Bacher, *Phys. Rev. B* **85**, 035325 (2012).
- [31] H. Lu, F. Guo, B. Zhang, and W. Ning, *Micro & Nano Lett.* **11**, 623 (2016).
- [32] C. R. Muller, L. Worschech, and A. Forchel, *Phys. Rev. B* **79**, 205307 (2009).
- [33] J. Nannen, T. Kummell, M. Bartsch, K. Brunner, and G. Bacher, *Appl. Phys. Lett.* **97**, 173108 (2010).
- [34] D. V. Lang, *J. Appl. Phys.* **45**, 3023 (1974).
- [35] S. Anand, N. Carlsson, M.-E. Pistol, L. Samuelson, and W. Seiffert, *Appl. Phys. Lett.* **67**, 3016 (1995).
- [36] C. M. A. Kapteyn, F. Heinrichsdorff, O. Stier, R. Heitz, M. Grundmann, N. D. Zakharov, D. Bimberg, and P. Werner, *Phys. Rev. B* **60**, 14265 (1999).
- [37] S. W. Lin, C. Balocco, M. Missous, A. R. Peaker, and A. M. Song, *Phys. Rev. B* **72**, 165302 (2005).
- [38] S. Schulz, A. Schramm, C. Heyn, and W. Hansen, *Phys. Rev. B* **74**, 033311 (2006).
- [39] M. Geller, E. Stock, C. Kapteyn, R. L. Sellin, and D. Bimberg, *Phys. Rev. B* **73**, 205331 (2006).
- [40] O. Engström, M. Kaniewska, M. Kaczmarczyk, and W. Jung, *Appl. Phys. Lett.* **91**, 133117 (2007).
- [41] A. Schramm, S. Schulz, T. Zander, C. Heyn, and W. Hansen, *Phys. Rev. B* **80**, 155316 (2009).
- [42] T. Nowozin, L. Bonato, A. Högner, A. Wiengarten, D. Bimberg, W.-H. Lin, S.-Y. Lin, C. J. Reyner, B. L. Liang, and D. L. Huffaker, *Appl. Phys. Lett.* **102**, 052115 (2013).
- [43] L. Schnorr, T. Heinzl, S. Scholz, A. Ludwig, and A. D. Wieck, *J. Appl. Phys.* **124**, 104301 (2018).
- [44] L. Schnorr, J. Labes, L. Kurten, T. Heinzl, C. Rothfuchs-Engels, S. Scholz, A. Ludwig, and A. D. Wieck, *Phys. Rev. B* **104**, 035303 (2021).
- [45] D. S. Day, M. Y. Tsai, B. G. Streetman, and D. V. Lang, *J. Appl. Phys.* **50**, 5093 (1979).
- [46] S. Schulz, Ph.D. Thesis, Hamburg University (2005).
- [47] V. Korobov and V. Ochkov, *Chemical Kinetics with Mathcad and Maple* (Springer, Vienna, 2011).
- [48] E. N. Korol, *Ukr. Phys. J.* **18**, 1890 (1973).
- [49] G. Snider, 1D Poisson-Schrodinger solver (2017), <https://www3.nd.edu/~gsnider/>, Accessed on Sep. 15th, 2017.
- [50] P. Virtanen, R. Gommers, T. E. Oliphant, M. Haberland, T. Reddy, D. Cournapeau, E. Burovski, P. Peterson, W. Weckesser, J. Bright, S. J. van der Walt, M. Brett, J. Wilson, K. J. Millman, N. Mayorov, A. R. J. Nelson, E. Jones, R. Kern, E. Larson, C. J. Carey, Í. Polat, Y. Feng, E. W. Moore, J. VanderPlas, D. Laxalde, J. Perktold, R. Cimrman, I. Henriksen, E. A. Quintero, C. R. Harris, A. M. Archibald, A. H. Ribeiro, F. Pedregosa, P. van Mulbregt, and SciPy 1.0 Contributors, *Nature Methods* **17**, 261 (2020).
- [51] E. Hairer and G. Wanner, *Solving Ordinary Differential Equations II. Stiff and Differential-Algebraic Problems*, Vol. 14 (Springer, New York, 1996).
- [52] R. J. Luyken, A. Lorke, A. O. Govorov, J. P. Kotthaus, G. Medeiros-Ribeiro, and P. Petroff, *Appl. Phys. Lett.* **74**, 2486 (1999).
- [53] J. R. Norris, in *Markov Chains*, Cambridge Series in Statistical and Probabilistic Mathematics (Cambridge University Press, Cambridge, 1997), pp. 60–107.
- [54] A. A. Markov, *Sci. Context* **19**, 591 (2006).
- [55] J. W. Eaton, D. Bateman, S. Hauberg, and R. Wehbring, GNU Octave version 5.2.0 manual: A high-level interactive language for numerical computations (2020).
- [56] See Supplemental Material at <http://link.aps.org/supplemental/10.1103/PhysRevB.104.205310> for simulations under additional initial conditions.

# Hysteretic capacitance-voltage characteristics of self-assembled quantum dots far from equilibrium with their environment

L. Schnorr, O. Khoukhi, L. Berg, and T. Heinzel\*

*Solid State Physics Laboratory, Heinrich-Heine-Universität Düsseldorf, 40204 Düsseldorf, Germany*

C. Rothfuchs-Engels, S. Scholz, A. Ludwig, and A. D. Wieck

*Lehrstuhl für Angewandte Festkörperphysik, Ruhr-Universität Bochum, 44780 Bochum, Germany*

This supplement gives further information on the time dependent occupation probability of the SAQD ensembles at selected bias voltages as well as the voltage dependent time required to reach a steady state.

## I. TIME EVOLUTION

Figure 1 shows the calculated, time dependent occupation probability of the SAQD layer for various bias voltages after preparation in the initial state with all three SAQD levels fully occupied. As discussed in the main text, the time needed to reach a steady state configuration shows a maximum for  $V = -1.2$  V.

## II. SETTLING TIME

Figure 2 shows the time needed to reach the steady state as a function of the bias voltage. Three peaks can be observed at  $V = -1.2$  V,  $V = -0.62$  V and  $V = -0.29$  V which coincide with the crossings of the capture and emission rates for the s-, p- and d-states, respectively, in Fig. 5(c) of the main text, as well as with the maxima of the calculated hysteretic charge difference in Fig. 6(a) . The global maximum of the time needed to reach a steady state is located at  $V = -1.2$  V where it amounts to 5200 s.

---

\* thomas.heinzel@hhu.de



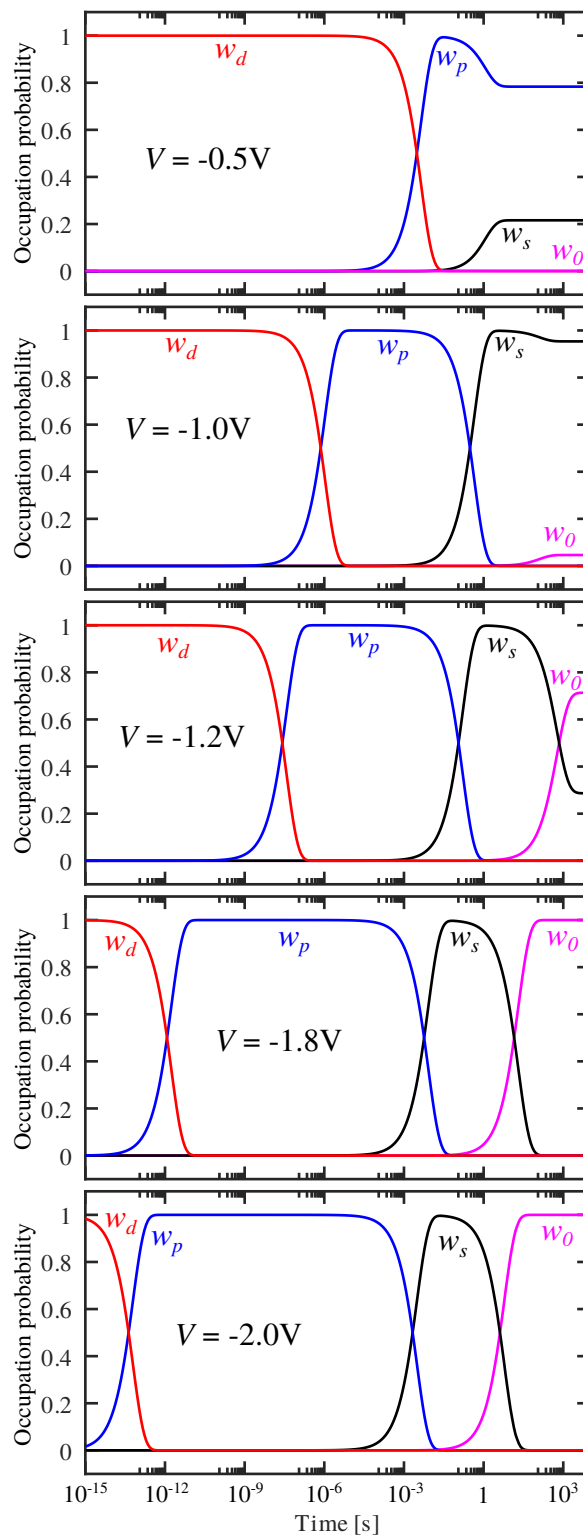


FIG. 1. Time evolution towards the steady state from completely filled SAQDs at various bias voltages.

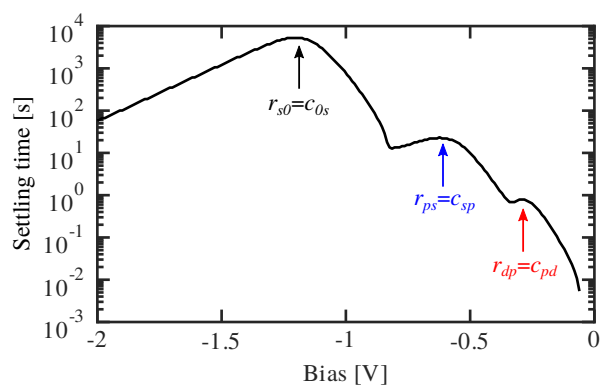


FIG. 2. Time needed to reach a steady state as a function of the bias voltage.



## 4.2 Paper II

### Reference

L. Berg, L. Schnorr, J. Wilkens, T. Heinzl, C. Rothfuchs-Engels, S. Scholz, A. Ludwig, and A. D. Wieck  
Phys. Rev. B **109**, 235433 (2024)  
DOI: <https://doi.org/10.1103/PhysRevB.109.235433>  
©2024 American Physical Society

### Copyright statement







The author has the right to use the article or a portion of the article in a thesis or dissertation without requesting permission from APS, provided the bibliographic citation and the APS copyright credit line are given on the appropriate pages.

### Contributions

I planned most of the experiments and participated in their conduction. I analysed most of the data. I contributed to manuscript writing.

---

## Electron capture dynamics into self-assembled quantum dots far from equilibrium with their environment

L. Berg <sup>1</sup>, L. Schnorr <sup>1</sup>, J. Wilkens <sup>1</sup>, T. Heinzel <sup>1,\*</sup>, C. Rothfuchs-Engels <sup>2</sup>, S. Scholz <sup>2</sup>, A. Ludwig <sup>2</sup> and A. D. Wieck <sup>2</sup>

<sup>1</sup>*Solid State Physics Laboratory, Heinrich-Heine-Universität Düsseldorf, 40204 Düsseldorf, Germany*

<sup>2</sup>*Lehrstuhl für Angewandte Festkörperphysik, Ruhr-Universität Bochum, 44780 Bochum, Germany*



(Received 4 October 2023; revised 2 May 2024; accepted 7 June 2024; published 26 June 2024)

We report studies of the electron capture process in self-assembled quantum dots (SAQDs) far from equilibrium with their environment and at large distance to the reservoirs. Deep level transient spectroscopy is used to determine the capacitance transients in response to bias voltage pulses, from which the capture rates are obtained as a function of the temperature and the quantum dot occupancy. The observed activated character of the capture suggests that the dominant electron source is the back contact. A model is developed based on electrons diffusing from the reservoir across the flat band region and getting captured in the SAQDs after overcoming the barrier formed by the space charge region between its onset and the quantum dots. For small barriers, we identify a distinct tunneling contribution to the capture current.

DOI: [10.1103/PhysRevB.109.235433](https://doi.org/10.1103/PhysRevB.109.235433)

### I. INTRODUCTION

Self-assembled quantum dots (SAQDs) are quasi-zero-dimensional semiconductor islands embedded in a host crystal with a larger band gap [1,2]. They can be considered as artificial atoms which can be ionized but also excited internally. This enables a wide variety of fundamental experiments [3–6] and technological applications [7]. In several implementations like quantum dot lasers [8,9] or light-emitting diodes [10], the SAQDs are positioned inside an extended, weakly conductive spacer layer that inhibits charge transfers close to equilibrium conditions. However, it is quite common to apply large electric fields to such structures, for example, in electrically driven single-photon sources or in floating-gate type storage devices [11]. Frequently, the capture process plays a crucial functional role. In single-photon sources as well as in storage devices, a short capture time is beneficial due to its influence on the repetition rates. A comprehensive understanding of the capture process is therefore of vital interest, not only for fundamental reasons, but also to optimize it according to the specific requirements. Hitherto, however, the electron capture under such conditions has not been studied thoroughly.

Here, we use deep level transient spectroscopy (DLTS) [12] to measure the capacitive capture transients as a function of the bias voltage and the temperature and discuss the underlying physics within a diffusive model based on band structure calculations. The work is complementary to previous studies on similar samples with focus on the emission process [13–25]. Capacitive capture transients on a similar sample have been reported before, however, without analysis or modeling of the data [24].

In Sec. II, the samples and experimental methods are described. Section III reports the DLTS measurements and the dependence of the measured time constant on temperature and

bias voltage. In Sec. IV, a model for the dominant capture process is proposed and alternative processes are discussed. The text concludes with a summary and an outlook (Sec. V).

### II. EXPERIMENTAL SETUP AND MEASUREMENT TECHNIQUE

The layout of the sample and its preparation have been described in detail elsewhere [23–25]. In brief, we focus on InAs quantum dots embedded in a Ga[Al]As heterostructure as a model system. The structure is prepared by molecular beam epitaxy, with an SAQD layer 500 nm above a Si<sup>+</sup> doped back contact and 413 nm below the sample surface; see Fig. 1(a). The SAQDs have a sheet density of  $n_{QD} = 10^{14} \text{ m}^{-2}$ . They are embedded in a 26 nm layer of undoped GaAs in order to avoid mutual influences of the dopants and the SAQD growth. Bias voltages can be applied to a Cr/Au top electrode with respect to the grounded back contact, which is accessed via a local region where In has been alloyed into the heterostructure. The gated area amounts to  $A = (0.3 \text{ mm})^2$ , covering approximately  $9 \times 10^6$  quantum dots.

The measurements are taken in a liquid helium cryostat (Leiden Cryogenics), operated at temperatures between 3 K and 77 K. The sample rests in vacuum. The system is equipped with a superconducting solenoid, which allows the generation of magnetic fields up to  $B = 11 \text{ T}$ , oriented perpendicularly to the sample surface. Rectangular voltage pulses with levels for preparation ( $V_p$ ) and measurement ( $V_m$ ) of the SAQD occupancy are applied to the top gate with respect to the back contact, which is kept at virtual ground via a HF2TA transimpedance amplifier ( $Z = 1 \text{ k}\Omega$ ) from Zurich Instruments. Its output is recorded with a 5444B digital oscilloscope (PicoTechnology) plus a HF2LI lock-in amplifier (Zurich Instruments), which also provides the ac voltage. The voltage pulses are generated using a Keithley Model 3390 arbitrary waveform generator with a transition time of 100 ns and

\*Contact author: [thomas.heinzel@hhu.de](mailto:thomas.heinzel@hhu.de)

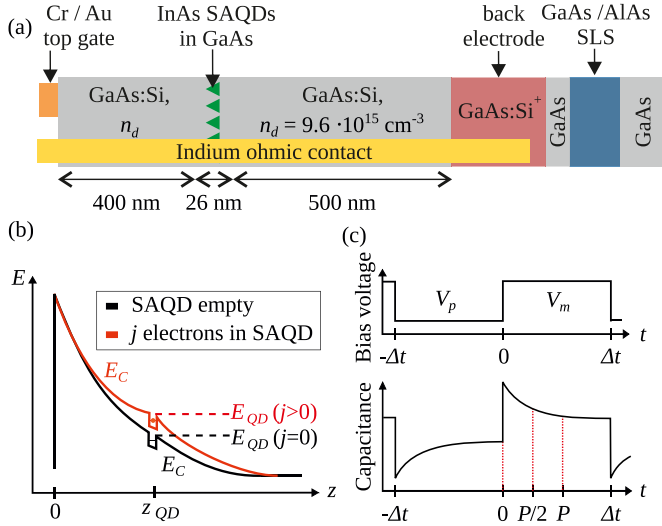


FIG. 1. (a) Cross sectional schematic view of the sample layout. The SAQD layer is indicated by the green triangles. The back electrode is accessed via an alloyed In contact and the top gate is formed by a Cr/Au electrode. The silicon doping density in the spacer layer is indicated by  $n_d$ . (b) Schematic band diagram for the case of a negative voltage applied to the top gate with respect to the grounded back electrode and its dependence on the SAQD occupation. (c) Schematic capacitance transients in response to rectangular bias voltage pulses (voltage levels  $V_p$  and  $V_m$  for the preparation and the measurement of the charge configuration, respectively) of duration  $\Delta t$ . The time window selected for the analysis is denoted by  $P$ .

superimposed with the ac voltage. In this setup, the output current obtained at a phase shift of  $\pi/2$  with respect to the input ac voltage detects the differential capacitance of the sample. The excitation frequency of 28 MHz (amplitude 10 mV) was selected as a compromise between high time resolution and negligible dielectric relaxation.

### III. LOCK-IN DLTS MEASUREMENTS

The initial state of the sample is prepared by applying a bias voltage  $V_p$  for a duration of  $\Delta t = 491$  ms to the top gate with respect to the grounded back electrode. Afterwards, the measurement voltage  $V_m$  is applied for  $\Delta t$  and the capacitance transient is recorded with a time resolution of 10  $\mu$ s. In Fig. 1(c), the typical capacitive response of the sample to such bias voltage pulses is illustrated schematically. As the SAQDs are gradually filled with electrons, the (positive) charge density decreases locally, which is compensated by an increase of the depletion length, thereby leading to a decrease of the capacitance over time, which represents our primary measurement signal.

Lock-in DLTS [26] is very convenient for characterizing the charge transfer processes as a function of the temperature, the initial conditions, and of the applied voltage. Within this concept, the measured capacitance transients  $C(t, V_p, V_m)$  are processed numerically according to

$$S(T, P, V_p, V_m) = \frac{1}{N_P} \left( \sum_{i=1}^{N_P/2} C_i - \sum_{i=N_P/2+1}^{N_P} C_i \right), \quad (1)$$

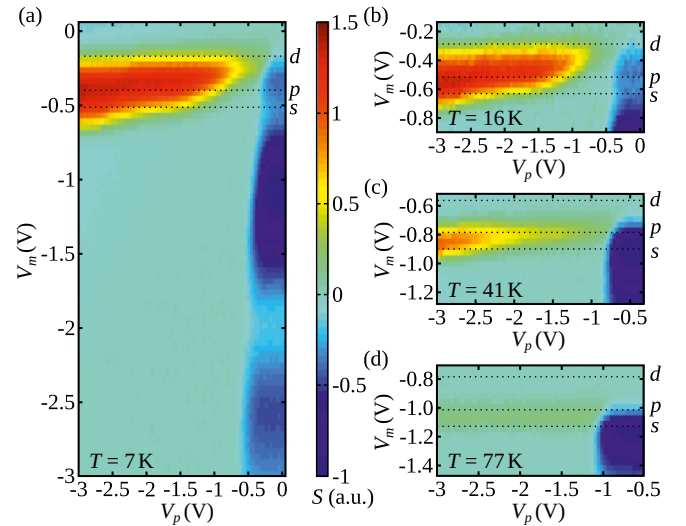


FIG. 2. Color plots of the measured lock-in DLTS signals  $S(V_p, V_m)$  for various temperatures. The underlying experimental data are the same as those evaluated in Fig. 3 of Ref. [25]. The dotted horizontal lines denote the computed onset voltages for capture into previously empty  $s$ ,  $p$ , and  $d$  states, respectively. The color bar, valid for all subfigures, represents the value of  $S$  in arbitrary units.

where  $T$  denotes the temperature and  $N_P$  is the number of data points (labeled by  $i$ ) within the selected time window. In the case that the absolute value of  $S(P)$  has a maximum, it appears at  $P = \tau/0.398$ , where  $\tau$  is the time constant of an exponential transient. Furthermore, positive values of  $S$  indicate electron capture, while for negative  $S$  electrons are emitted from the SAQDs. With our setup, DLTS signals can be obtained for time windows  $P$  ranging from  $\approx 100$   $\mu$ s to  $\Delta t$  and  $P$  was selected according to the best visibility of the capture process.

In Fig. 2, the measured lock-in DLTS signals are reproduced for four different temperatures with focus on the voltage regime where capture is observed (i.e.,  $S > 0$ ). In these measurements,  $P = 491$  ms has been used. For a temperature of 7 K shown in Fig. 2(a), the emission transients are located at  $V_p \geq -0.7$  V and extend over the range  $-3 \text{ V} \leq V_m \leq 0$  V. They have been described in detail elsewhere [24,25] and will not be discussed here. We first focus on the capture behavior observed at  $T = 7$  K; see Fig. 2(a). As the measurement voltage is increased starting from  $V_m - 3$  V, capture sets in at  $V_m \approx -650$  mV for a preparation voltage  $V_p = -3$  V. As  $V_p$  is increased, this onset voltage increases as well in the form of two weakly pronounced steps. As  $V_m$  is further increased, the capture signal disappears abruptly and almost independently of  $V_p$  at  $V_m = -200$  mV. A temperature increase, see Figs. 2(b)–2(d), causes the capture peak to shift towards lower  $V_m$ , reaching a value of  $V_m = -1.05$  V at 77 K. This goes along with  $S(V_m)$  becoming more symmetric, while the fine structure is suppressed and no longer visible at 77 K.

These observations can be interpreted qualitatively in a straightforward way. After applying a sufficiently negative preparation voltage pulse, the SAQDs are empty. As  $V_m$  is increased, the energies of the SAQD states with respect to the grounded back electrode decrease, thereby increasing the capture rate. At the lower edge of the peak, the time constant

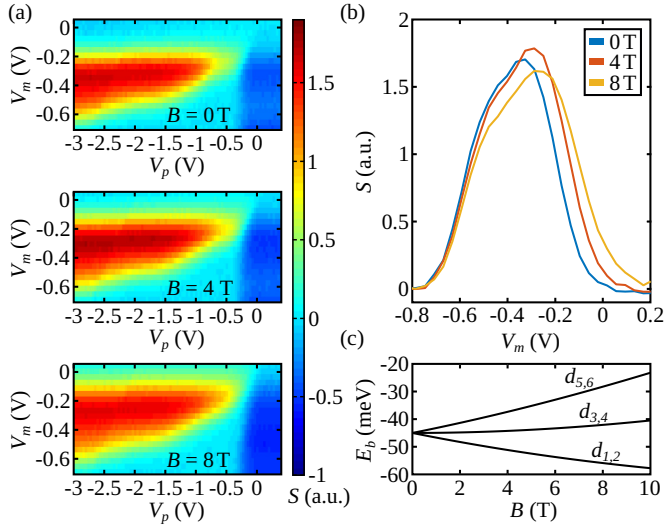


FIG. 3. Dependence of the lock-in signal on perpendicular magnetic fields  $B$ . (a) Evolution of  $S(V_p, V_m)$  as  $B$  is increased and (b) lineouts  $S(V_m, V_p = -3 \text{ V})$  thereof. Further functions  $S(V_p, V_m)$  at different  $B$  are shown in the Supplemental Material. (c) Model calculation for the evolution of the binding energy  $E_B$  of the  $d$  states of the SAQDs as a function of  $B$  within the Fock-Darwin spectrum. Not shown is the splitting of the levels of the single electron charging energy of 15 meV per electron that enters an SAQD.

of the transient drops into the time window defined by the selection of  $P$ . Capture can be observed up to the measurement voltage where it becomes too fast to be measured with the selected  $P$ — $V_m = -200 \text{ mV}$  in the present case. For larger  $V_p$  values, the initial occupancy of the SAQDs increases, leading to a reduced capture signal, as well as to steps in the onset value of  $V_m$  when the SAQD states have remained occupied during the preparation stage. Furthermore, the temperature dependence implies a thermally activated capture process. As the temperature is increased, the average kinetic energy of the electrons to be captured increases as well, thus enabling capture with the same rate at larger SAQD energies. The substructure of the capture peak is suppressed under increasing temperature. For example, at 77 K and for negative bias voltages, the emission time constant for the  $p$  states can be estimated to 100 ns—two orders of magnitude below our resolution limit.

Apparently, despite the presence of strong electric fields, the capture comprises a dominant thermally activated process. This is not self-evident considering that the electrons could originate from, for example, the leakage current or field ionization of deep donors.

A perpendicular magnetic field  $B$  allows one to tune the SAQD energy levels independent of the applied electric field. The  $B$  dependence of the capture is summarized in Fig. 3(a). Cross sections of  $S(V_m)$  at fixed  $V_p$  [selected in 3(b) was  $V_p = -3 \text{ V}$ ] illustrate the composite structure of the  $S$  peak, comprising a  $B$ -independent component at lower  $V_m$  and a  $B$ -dependent contribution located at larger  $V_m$  values, i.e., for  $V_m < \approx -500 \text{ mV}$ , whose time constant increases with increasing magnetic field.

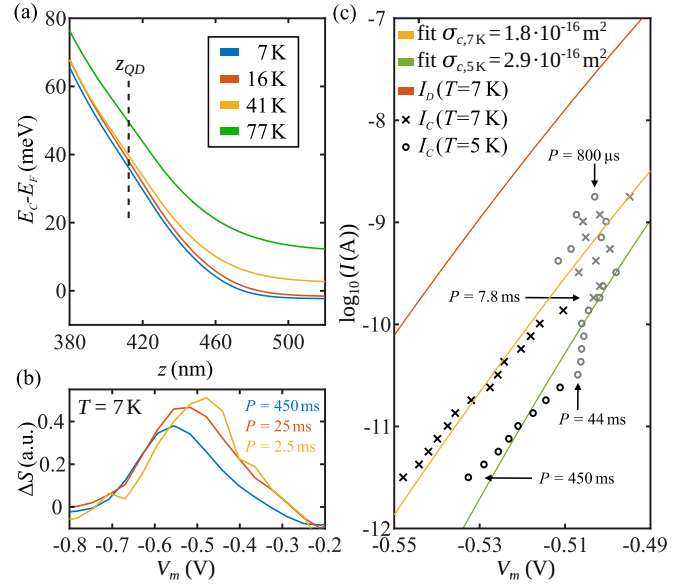


FIG. 4. (a) Calculated conduction band profiles for different temperatures at a bias voltage of  $-0.8 \text{ V}$ . (b) Contribution  $\Delta S$  to  $S$  from the SAQD  $s$  states for different time constants, as found for  $T = 7 \text{ K}$  after subtracting the contributions from the  $p$  and  $d$  levels. (c) Current due to charging of the  $s$  states as a function of the measurement voltage for various time constants and for two temperatures  $T = 5 \text{ K}$  (open circles) and  $7 \text{ K}$  (crosses) and the corresponding fits according to Eq. (4) with the capture cross section as fit parameter (green and yellow full lines). Also shown is the total diffusion current reaching  $z_{QD}$  (orange line). Only the black symbols have been used in the fits described in the text.

#### IV. MODEL FOR THE ELECTRON CAPTURE PROCESS

In this section, we are going to argue that, at large SAQD energies  $E_{QD}$  (low  $V_m$ ), electrons get captured predominantly from the diffusion current arriving at the SAQD site from the back electrode. At lower  $E_{QD}$ , the barrier between the back electrode and the SAQD is sufficiently small to allow additional tunneling between the conduction band and the  $d$  states of the SAQDs.

To identify the origin of the captured electrons, we first compute the conduction band profile. The doping density in the spacer layer is obtained from capacitance-voltage measurements followed by a Mott-Schottky analysis to  $n_d = 9.6 \times 10^{15} \text{ cm}^{-3}$  and a built-in potential barrier of  $V_{bi} = 650 \text{ mV}$  is extracted [27]. These values are used as input for one-dimensional, self-consistent Poisson-Schrödinger calculations of the conduction band profile [28]. Here, the SAQD layer is included in the form of a two-dimensional charge layer, with an electron density that corresponds to the assumed occupancy of the SAQDs. Literature values for the temperature dependent dielectric constant of GaAs have been used [29]. It becomes apparent that the capture by initially empty dots sets in at measurement voltages where the SAQD layer resides close to, i.e., within  $\approx 50 \text{ nm}$  of the edge of the space charge region. At these conditions, the barrier height with respect to the Fermi level of the back electrode is relatively small; see Fig. 4(a) for an example. As the temperature is increased from 7 K to 77 K,  $E_{QD}$  increases by  $\approx 20 \text{ meV}$ .



Now, thermally activated electrons can diffuse from the back electrode across the flat band region into the space charge layer and may get captured in SAQD states. For this process, the capture rate equals the flux density of diffusing electrons at the location  $z_{QD}$  of the SAQDs, multiplied by the capture cross section  $\sigma_c$  [30]. Comparing this situation at  $V_m = -0.8$  V, for example, to the measured capture signal with  $\tau = 195$  ms as shown in Fig. 2, this effective barrier between the back contact and the SAQDs is too large for capture at 7 K and 16 K, while at 41 K a peak in  $S$  is observed. As  $T$  is increased further to 77 K, the capture time drops well below 195 ms and the lock-in DLTS signal vanishes.

For an initial nonzero occupancy, the Coulomb interaction increases the energy barrier of height  $E(z_{QD}, V_m, k)$ , where  $k$  denotes the number of electrons in one dot at the end of the preparation pulse. Therefore, the capture of additional electrons per SAQD sets in at a steplike increasing value for  $V_m$  as the preparation voltage increases, in agreement with the observations. Since  $E(z_{QD})$  increases with the occupancy, the onset value for  $V_m$  at which filling of a particular level starts can be estimated with the Poisson Schrödinger solver for each occupancy at a given value for  $V_p$ , by calculating the detectable diffusion current according to Eq. (3). In Fig. 2, the computed values for  $V_m$  required to fill the first, the third, and the seventh electron (i.e., the onset of filling electrons in the  $s$ ,  $p$ , and  $d$  levels, respectively) in the SAQDs are included as dashed horizontal lines. These values agree reasonably well with the observed fine structure of the capture peak.

We now focus on the filling of the  $s$  states after a preparation voltage of  $V_p = -3$  V, assuming that the electrons can enter the SAQDs via all their energy levels and then relax rapidly into the  $s$  states. The contribution of the  $s$  state filling to the capture signal is isolated by subtracting  $S(V_m)$  for  $V_p = -2$  V (where capture into the  $s$  state is negligible) from the function  $S(V_m)$  measured at  $V_p = -3$  V.

The time constants  $\tau(V_m, T)$  follow directly from the measured transients and reflect the effective time of charge transfer between the SAQDs and the environment, composed of both capture and emission of electrons. It can be interpreted directly as capture time constant  $\tau_c$  only in limiting cases where emission is negligible. This is certainly not justified at higher temperatures or over the full interval of bias voltages. For example, in the measurement at  $T = 7$  K close to  $V_p = V_m = -0.5$  V, Fig. 2(a),  $S$  vanishes, indicating that the two transfer rates are identical. Previously, a rate equation model has been established which allows the separation of the capture and emission rates [25]. It shows that, after our preparation time interval, all SAQD states are empty for  $V_p \lesssim -2.8$  V, since  $\tau_e \ll P \ll \tau_c$ , where  $\tau_e$  denotes the emission time constant. The difference  $\Delta S(V_m) \equiv S(V_m, V_p = -3$  V)  $- S(V_m, V_p = -2$  V) therefore represents the capture solely into the  $s$  states and is shown in Fig. 4(b) for a few exemplifying rate windows. The maximum of  $\Delta S(V_m)$  shifts to larger voltages as the selected time window  $P$  is decreased, reflecting the faster charging under more positive bias voltages. The corresponding charging current  $I_c$  during capture can be estimated by

$$I_c(V_m) = A \frac{en_{QD}}{\tau(V_m)}, \quad (2)$$

where  $e$  denotes the elementary charge. These values, with the time constant obtained from the maximum of a Gaussian function fitted to  $\Delta S(V_m)$ , are plotted in Fig. 4(c) for two temperatures. Apparently, at  $T = 5$  K, the charging current increases approximately exponentially with  $V_m$ , with an abrupt increase of the exponent at  $V_m \approx -0.505$  V, suggesting that the charging mechanism changes for sufficiently low potential barriers. As the temperature is increased to  $T = 7$  K,  $I_c$  is larger for the same measurement voltage, with a comparable exponent. However, a kink at larger  $V_m$  is no longer clearly visible. Rather, the extracted values for  $I_c$  become quite noisy for  $V_m \geq -0.51$  V, a consequence of the small  $P$  values.

The measured current can be compared to the calculated diffusion current  $I_D(V_m)$  generated by electrons arriving at  $z_{QD}$  from the back electrode,

$$I_D(V_m) = eA \times \mu k_B T \frac{dn}{dz}. \quad (3)$$

Here, the density and the mobility of the electrons are denoted by  $n$  and  $\mu$ , respectively, and the SAQDs are assumed to be empty initially. The diffusion current  $I_D(V_m)$  obtained for  $V_m \leq -0.505$  V and  $V_m \leq -0.51$  V for  $T = 5$  K and  $T = 7$  K, respectively, has the same shape as the capture current  $I_c(V_m)$ ; see Fig. 4(c). These currents are related by

$$I_c(V_m) = I_D(V_m)n_{QD} \times \sigma_c. \quad (4)$$

A least squares fit according to Eq. (4) is carried out for data at  $T = 5$  K in the interval  $V_m < -0.505$  V, using  $\sigma_c$  as a fit parameter that takes the value  $\sigma_c = 1.8 \times 10^{-16}$  m<sup>2</sup>, which is plausible considering that the SAQDs have an approximately conical shape with a base radius of  $\approx 15$  nm [31]. This analysis has been carried out for the other temperatures as well, which gives similar capture cross sections within a factor of 2 [27]. The case of  $T = 7$  K thereof has been included in Fig. 4(c).

For the lowermost temperature and  $V_m \geq -0.505$  V, the exponent of  $I_c(V_m)$  shows a different slope. In this regime, the barrier between the flat band region and the SAQDs is of the order of a few meV only and decreases with increasing  $V_m$ . Thus tunneling through this barrier becomes possible and may contribute to the capture current. As  $V_m$  is increased, both the thickness and the height of the barrier decrease, while the spectral electron density around  $E_{QD}$  increases. It appears plausible that as a result a strongly gate voltage-dependent tunnel current evolves, which may be composed of elastic and thermally activated components. Due to its dependence on several parameters, modeling the tunneling current in this system is not very trustworthy with the information at hand and we therefore refrain from a quantitative description. Since, however, the barrier for tunneling into the  $s$ ,  $p$ , and  $d$  states is very large, capture by tunneling under these conditions is expected to take place via high lying states only, which are no longer bound in occupied dots.

In view of this analysis, the  $B$ -independent lower edge of  $S(V_m)$  in Figs. 3(a) and 3(b) can be interpreted as a diffusion-dominated regime. The upper,  $B$ -dependent tails of these peaks are dominated by tunneling into the  $d$  states of the SAQDs with occupied  $s$  and  $p$  levels: as  $B$  increases, the levels  $d_3$ – $d_6$ , see Fig. 3(c), increase in energy and thus the spectral density of electrons available for tunneling decreases, which results in larger capture time constants. This line of

arguing is similar to that one used to explain the magnetic field dependence of the emission by tunneling, as observed with conventional DLTS [19]. The full spectra  $S(V_m, V_p)$  as a function of  $B$  as well as lineouts in the emission-dominated regime are represented and interpreted in Fig. 4 of the Supplemental Material [27].

We conclude this section with three remarks. First of all, the leakage current is below our resolution limit in the studied bias voltage interval [27]. It therefore does not contribute significantly to the filling of the SAQDs. Second, the energy resolution of the measurement concept used here is too low to observe the effects of single electron charging on the capture dynamics within one orbital energy level. In the diffusion-dominated capture regime, the time constant changes rapidly with  $V_m$  and generates a narrow peak in  $S(V_m)$ . In the capture regime dominated by tunneling, on the other hand, the capture time constants are too close to our resolution limit. Possibly, the resolution can be improved by applying the much more time-consuming Laplace transform spectroscopy, where the single electron charging energy could be well resolved during emission processes [23]. Finally, the shape of the capture peak in the  $(V_p, V_m)$  plane can be modeled by solving the system of rate equations with  $c_k(V_p, V_m)$  as a fit parameter, where the  $c_j$  represent the capture rates into level  $j$ . However, these complements do not contribute to the identification of the capture process and are beyond the scope of the present work.

## V. SUMMARY AND CONCLUSIONS

We have used capacitive deep level transient spectroscopy to characterize the electron capture into self-assembled quantum dots which are far from equilibrium with their environment and reside at a large distance from the reservoirs.

The measured time constants of the transients contain, but are not equal to, the capture time, since significant emission takes place during capture over a wide parameter range. Therefore, the capture process has been analyzed in the voltage regime where emission is negligible. The capture shows a predominantly activated behavior. The combination of the experiments with Poisson-Schrödinger simulations suggest that, after changing the band structure by a bias voltage step, a new steady state will be established by a diffusion current  $\propto dn/dz$ , which fills the SAQDs up to the local quasi-Fermi level. Capture occurs predominantly if the SAQD layer is sufficiently close to the edge of the space charge region, such that the remaining barrier can be overcome thermally. Since under these assumptions the capture current as obtained from the capacitance transients should equal the diffusion current, the capture cross section of the  $s$  states can be estimated to  $\sigma_c \approx 3 \times 10^{-16} \text{ m}^2$ . For sufficiently small energy barriers between the SAQDs and the flat band region, tunneling contributes to the capture as well and we have explained the magnetic field dependence of the capture rates by tunneling into  $d$  states or, in the case of empty dots, into higher states. Future work may comprise measurements at higher energy resolution, for example, by using Laplace transform spectroscopy, with the possible identification of spin-selective charging as well as further capture mechanisms. Also, a detailed modeling of the capture peak with voltage-dependent capture rates, based on a rate equation model, is a possible next step.

## ACKNOWLEDGMENTS

C.R.-E., S.S., A.D.W., and A.L. gratefully acknowledge the support of TRR 160/2-Project No. B04, Deutsche Forschungsgemeinschaft Grant No. 383065199, and the Deutsch-Französische Hochschule Grant No. CDFH-05-06.

- 
- [1] D. Leonard, M. Krishnamurthy, C. M. Reaves, S. P. Denbaars, and P. M. Petroff, Direct formation of quantum-sized dots from uniform coherent islands of In[Ga]As on GaAs surfaces, *Appl. Phys. Lett.* **63**, 3203 (1993).
  - [2] P. M. Petroff, A. Lorke, and A. Imamoglu, Epitaxially self-assembled quantum dots, *Phys. Today* **54**(5), 46 (2001).
  - [3] P. Michler, A. Kiraz, C. Becher, W. V. Schoenfeld, P. M. Petroff, L. Zhang, E. Hu, and A. Imamoglu, A quantum dot single-photon turnstile device, *Science* **290**, 2282 (2000).
  - [4] M. Kroutvar, Y. Ducommun, D. Heiss, M. Bichler, D. Schuh, G. Abstreiter, and J. J. Finley, Optically programmable electron spin memory using semiconductor quantum dots, *Nature (London)* **432**, 81 (2004).
  - [5] C. L. Salter, R. M. Stevenson, I. Farrer, C. Nicoll, D. A. Ritchie, and A. J. Shields, An entangled-light-emitting diode, *Nature (London)* **465**, 594 (2010).
  - [6] A. Faraon, A. Majumdar, D. Englund, E. Kim, M. Bajcsy, and J. Vuckovic, Integrated quantum optical networks based on quantum dots and photonic crystals, *New J. Phys.* **13**, 055025 (2011).
  - [7] D. J. Mowbray and M. S. Skolnick, New physics and devices based on self-assembled semiconductor quantum dots, *J. Phys. D: Appl. Phys.* **38**, 2059 (2005).
  - [8] V. M. Ustinov, N. A. Maleev, A. E. Zhukov, A. R. Kovsh, A. Y. Egorov, A. V. Lunev, B. V. Volovik, I. L. Krestnikov, Y. G. Musikhin, N. A. Bert, P. S. Kopev, and Z. I. Alferov, InAs/InGaAs quantum dot structures on GaAs substrates emitting at 1.3  $\mu\text{m}$ , *Appl. Phys. Lett.* **74**, 2815 (1999).
  - [9] E. U. Rafailov, M. A. Cataluna, and W. Sibbett, Mode-locked quantum-dot lasers, *Nat. Photon.* **1**, 395 (2007).
  - [10] I. L. Krestnikov, N. A. Maleev, A. V. Sakharov, A. R. Kovsh, A. E. Zhukov, A. F. Tsatsulnikov, V. M. Ustinov, Z. I. Alferov, N. N. Ledentsov, D. Bimberg, and J. A. Lott, 1.3  $\mu\text{m}$  resonant-cavity InGaAs/GaAs quantum dot light-emitting devices, *Semicond. Sci. Technol.* **16**, 844 (2001).
  - [11] T. Nowozin, A. Marent, M. Geller, D. Bimberg, N. Akcay, and N. Öncan, Temperature and electric field dependence of the carrier emission processes in a quantum dot-based memory structure, *Appl. Phys. Lett.* **94**, 042108 (2009).
  - [12] D. V. Lang, Deep-level transient spectroscopy: A new method to characterize traps in semiconductors, *J. Appl. Phys.* **45**, 3023 (1974).
  - [13] S. Anand, N. Carlsson, M.-E. Pistol, L. Samuelson, and W. Seiffert, Deep level transient spectroscopy of InP quantum dots, *Appl. Phys. Lett.* **67**, 3016 (1995).

- [14] C. M. A. Kapteyn, F. Heinrichsdorff, O. Stier, R. Heitz, M. Grundmann, N. D. Zakharov, D. Bimberg, and P. Werner, Electron escape from InAs quantum dots, *Phys. Rev. B* **60**, 14265 (1999).
- [15] S. W. Lin, C. Balocco, M. Missous, A. R. Peaker, and A. M. Song, Coexistence of deep levels with optically active inas quantum dots, *Phys. Rev. B* **72**, 165302 (2005).
- [16] S. Schulz, A. Schramm, C. Heyn, and W. Hansen, Tunneling emission from self-assembled inas quantum dots probed with capacitance transients, *Phys. Rev. B* **74**, 033311 (2006).
- [17] M. Geller, E. Stock, C. Kapteyn, R. L. Sellin, and D. Bimberg, Tunneling emission from self - organized InGaAs/GaAs quantum dots observed via time - resolved capacitance measurements, *Phys. Rev. B* **73**, 205331 (2006).
- [18] O. Engström, M. Kaniewska, M. Kaczmarczyk, and W. Jung, Electron tunneling from quantum dots characterized by deep level transient spectroscopy, *Appl. Phys. Lett.* **91**, 133117 (2007).
- [19] A. Schramm, S. Schulz, J. Schäfer, T. Zander, C. Heyn, and W. Hansen, Electron emission from self-assembled quantum dots in strong magnetic fields, *Appl. Phys. Lett.* **88**, 213107 (2006).
- [20] A. Schramm, S. Schulz, C. Heyn, and W. Hansen, Suppression of competing tunneling processes in thermally-activated carrier emission on self-assembled InAs quantum dots, *Phys. Rev. B* **77**, 153308 (2008).
- [21] A. Schramm, S. Schulz, T. Zander, C. Heyn, and W. Hansen, Thermionic tunneling through coulomb barriers in charged self-assembled quantum dots, *Phys. Rev. B* **80**, 155316 (2009).
- [22] T. Nowozin, L. Bonato, A. Högner, A. Wiengarten, D. Bimberg, W.-H. Lin, S.-Y. Lin, C. J. Reyner, B. L. Liang, and D. L. Huffaker, 800 meV localization energy in GaSb/GaAs/Al<sub>0.3</sub>Ga<sub>0.7</sub>As quantum dots, *Appl. Phys. Lett.* **102**, 052115 (2013).
- [23] L. Schnorr, T. Heinzel, S. Scholz, A. Ludwig, and A. D. Wieck, Laplace deep level transient spectroscopy on self-assembled quantum dots, *J. Appl. Phys.* **124**, 104301 (2018).
- [24] L. Schnorr, J. Labes, L. Kurten, T. Heinzel, C. Rothfuchs-Engels, S. Scholz, A. Ludwig, and A. D. Wieck, Electron capture and emission dynamics of self-assembled quantum dots far from equilibrium with the environment, *Phys. Rev. B* **104**, 035303 (2021).
- [25] L. Schnorr, O. Khoukhi, L. Berg, T. Heinzel, C. Rothfuchs-Engels, S. Scholz, A. Ludwig, and A. D. Wieck, Hysteretic capacitance-voltage characteristics of self-assembled quantum dots far from equilibrium with their environment, *Phys. Rev. B* **104**, 205310 (2021).
- [26] G. L. Miller, D. V. Lang, and L. C. Kimerling, Capacitance transient spectroscopy, *Annu. Rev. Mater. Sci.* **7**, 377 (1977).
- [27] See Supplemental Material at <http://link.aps.org/supplemental/10.1103/PhysRevB.109.235433> for characterization measurements and the capture analysis at additional temperatures as well as in further magnetic fields.
- [28] G. Snider, *1D Poisson-Schrödinger solver* [accessed on Sep 15, 2017].
- [29] I. Strzalkowski, S. Joshi, and C. R. Crowell, Dielectric constant and its temperature dependence for GaAs, CdTe, and ZnSe, *Appl. Phys. Lett.* **28**, 350 (1976).
- [30] P. Blood and J. Orton, in *The Electrical Characterization of Semiconductors: Majority Carriers and Electron States*, edited by N. H. March (Academic Press, New York, 1992).
- [31] L. Schnorr, Electron capture and emission dynamics of self-assembled quantum dots, Ph.D. thesis, HHU Düsseldorf, 2022.

# Electron capture dynamics into self-assembled quantum dots far from equilibrium with their environment: supplemental material

L. Berg,<sup>†</sup> L. Schnorr,<sup>†</sup> J. Wilkens,<sup>†</sup> T. Heinzl,<sup>\*,†</sup> C. Rothfuchs-Engels,<sup>‡</sup> S. Scholz,<sup>‡</sup> A. Ludwig,<sup>‡</sup> and A. D. Wieck<sup>‡</sup>

<sup>†</sup>*Solid State Physics Laboratory, Heinrich-Heine-Universität Düsseldorf, 40204 Düsseldorf, Germany*

<sup>‡</sup>*Lehrstuhl für Angewandte Festkörperphysik, Ruhr-Universität Bochum, 44780 Bochum, Germany*

E-mail: thomas.heinzel@hhu.de

## Abstract

This supplement gives information about the current-voltage and capacitance-voltage properties of the sample used to determine the leakage currents, the doping density and the built-in potentials at the relevant temperatures. Additional measurements of the lock-in signal at various perpendicular magnetic fields are shown. Furthermore, the capture current is compared to the developed model expression at higher temperatures.



## I. Current-voltage characteristics

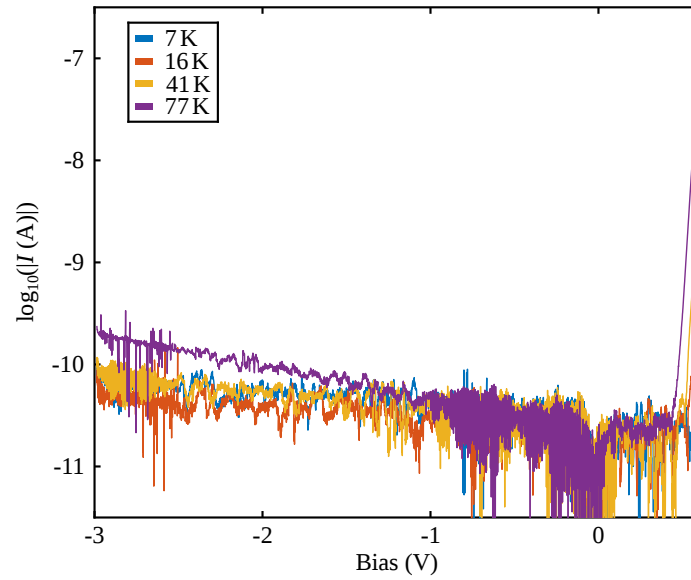


Figure 1: Current-voltage characteristics of the sample at the temperatures used for the studies. It is too small to explain the capture current in the studied measurement voltage interval.

## II. Mott-Schottky analysis

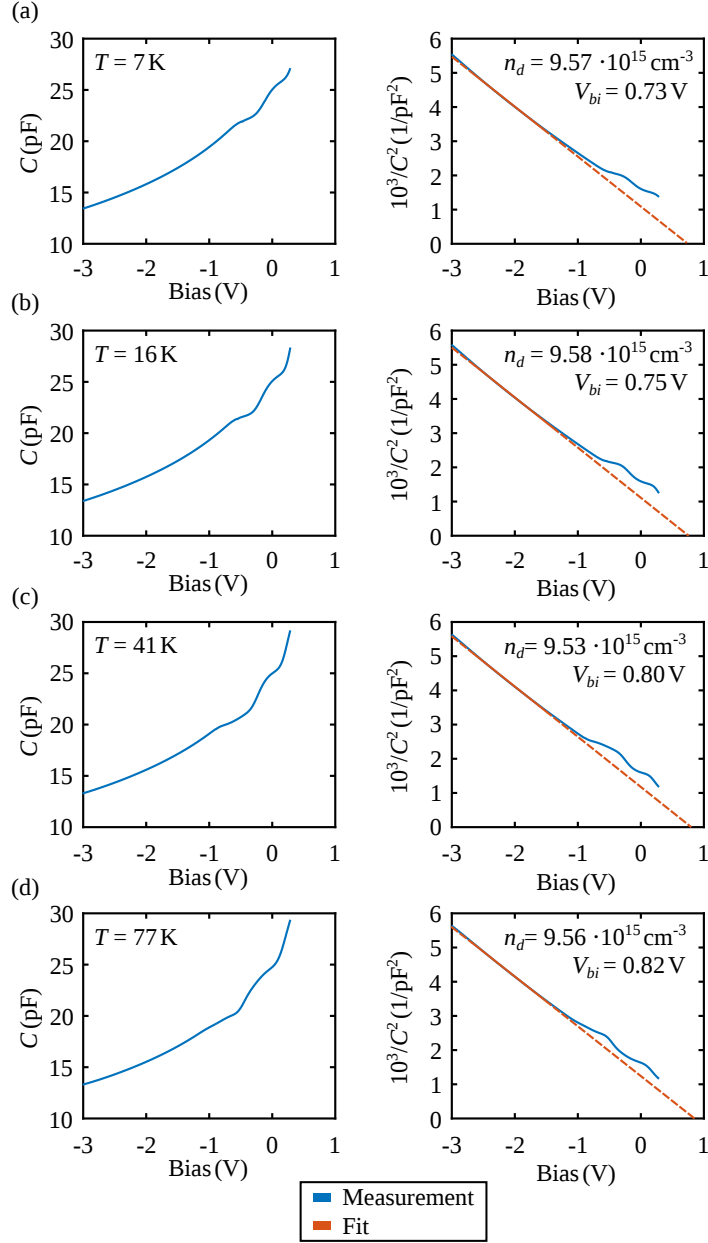


Figure 2: Capacitance-voltage dependence of the sample and the corresponding Mott-Schottky analysis in a temperature range from (a) 7 K to (d) 77 K. The fit for the Mott-Schottky analysis has been carried out in the region where the fit function is shown as a solid line. Voltages below  $-2.7$  V have been excluded due to a possible influence of the back contact. Above  $-1.5$  V, the SAQDs layer is getting filled which causes the peaks in this interval. To avoid hysteric effects, due to charge in the SAQDs, a sufficiently low bias has been applied to the sample before recording the data with an increasing bias voltage.

### III. Energetic barrier for the capture by diffusion

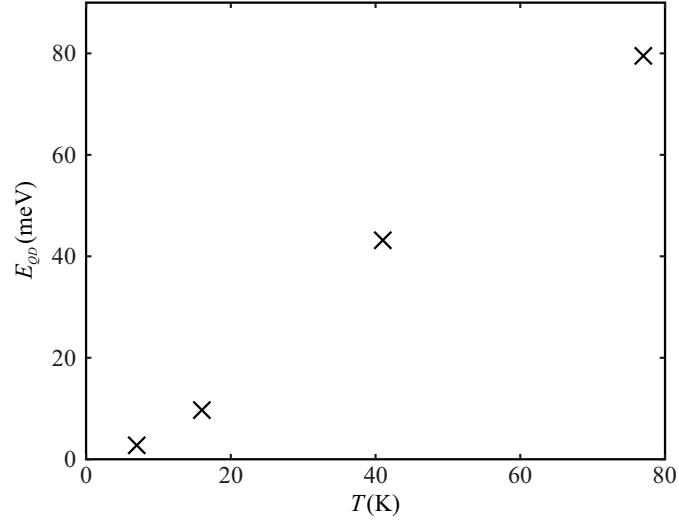


Figure 3: Energy barrier height for the SAQD filling within 450 ms, shown as a function of temperature. The measured bias voltages where capture in the empty dot is observed were extracted from figure 2 in the main text and the corresponding energy barriers were calculated with the help of the Poisson-Schrödinger solver.

## IV. Lock-in signals for various magnetic fields

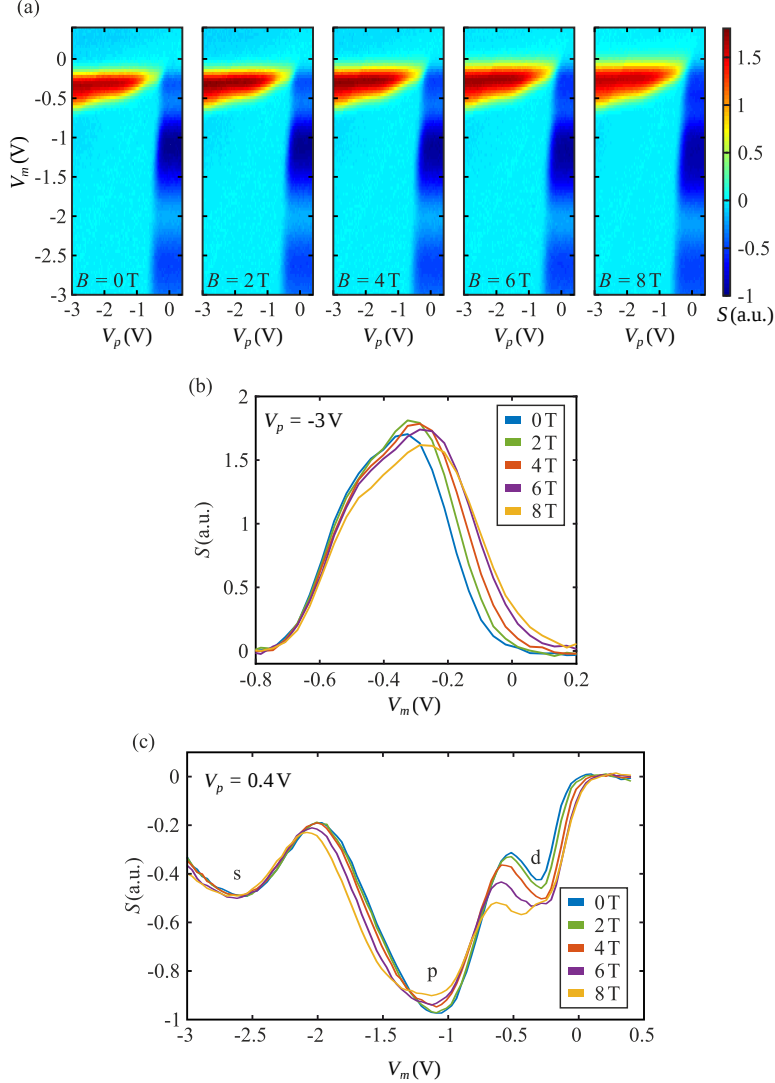


Figure 4: (a) Evolution of the color plots of the lock-in signals  $S(V_p, V_m)$  under various perpendicular magnetic fields. All data has been recorded at a temperature of  $T = 5\text{ K}$  and with a time window of  $P = 450\text{ ms}$ . (b) lineouts of these functions taken at  $V_p = -3\text{ V}$ . (c) Lineouts  $S(V_m)$  at  $V_p = 0.4\text{ V}$  where only emission takes place. The minima of  $S$  corresponding to emission from the s, p- and d-levels are labeled accordingly. There is essentially no shift of the s-states, while the p- and d- states broaden and shift to lower  $V_m$  as  $B$  increases. These shifts reflect the changes in the emission time averaged over the four p-states and the occupied d-states, respectively, while the broadening originates from the splitting of the levels in magnetic fields according to the Fock-Darwin model.

## V. Capture current at higher temperatures

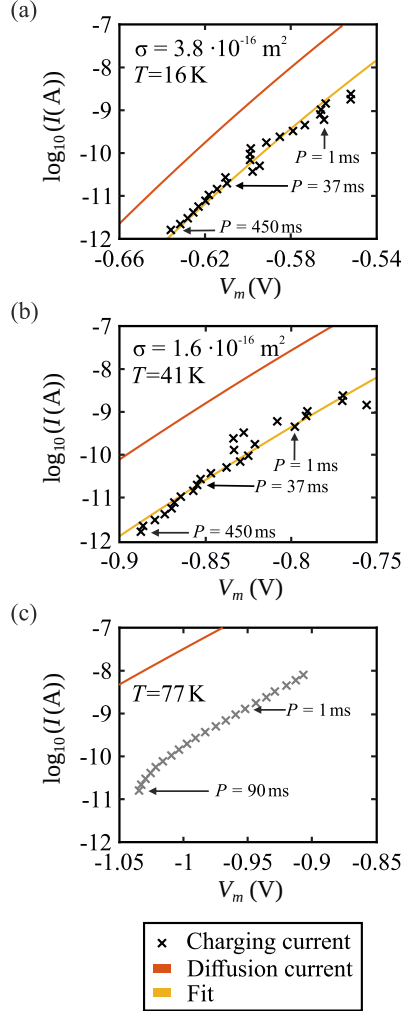


Figure 5: Comparison between current due to charging into the s-states and the diffusion current at the remaining temperatures under study, namely (a) 16 K, (b) 41 K and (c) 77 K. For 77 K, the fit is omitted due to the inseparability of capture and emission processes.



---

## Chapter 5

# Electrostatic inter-layer coupling between self-assembled quantum dots

Devices utilising the properties of SAQDs often incorporate multiple layers of them to enhance their functionality, such as LEDs [53], lasers [54] or solar cells [55]. An understanding of the inter-layer interactions is therefore crucial, especially with regard to the occupation dynamics. Notable interactions between quantum dots include the wave function hybridisation for distances below 10 nm [58–60], or correlated growth, up to layer distances of 50 nm [56, 57]. A Coulomb interaction has been reported on a distance of 20 nm [62]. *Paper III* explores an interdependence of two layers of SAQDs separated by a distance of 200 nm, one order of magnitude larger than previously reported. A detailed description of the sample was given in section 2.2.2. Isothermal DLTS was carried out at a temperature of 77 K, in a bias voltage region where capture and emission of both layers are observable and separable. The interaction arises because the charge in one layer modifies the occupation dynamics in the other layer. Charge in one layer generates both an electric field as well as it reduces the density of the free electrons in its surrounding. Another layer of SAQDs experiences this shift and the capture and emission rates adjust accordingly. Experimental evidence for this interdependence is presented. The bias voltage dependent occupation dynamics were successfully reproduced by a rate equation model.

---

## 5.1 Paper III

### Reference

L. Berg, L. Schnorr, T. Heinzl, C. Rothfuchs-Engels, N. Barth, A. Ludwig, and A. D. Wieck, "Electrostatic inter-layer coupling between self-assembled quantum dots". *Submitted*.

### Copyright statement

The author has the right to use the article or a portion of the article in a thesis or dissertation without requesting permission from APS, provided the bibliographic citation and the APS copyright credit line are given on the appropriate pages.

### Contributions

I planned and conducted all of the experiments and analysed all data. I processed the sample. I contributed to manuscript writing.



# Electrostatic inter-layer coupling between self-assembled quantum dots

L. Berg <sup>1</sup>, L. Schnorr <sup>1</sup>, C. Rothfuchs-Engels <sup>2</sup>, N. Bart <sup>2</sup>, A. Ludwig <sup>2</sup>, A. D. Wieck <sup>2</sup> and T. Heinzel <sup>1,\*</sup>

<sup>1</sup>*Solid State Physics Laboratory, Heinrich-Heine-Universität Düsseldorf, 40204 Düsseldorf, Germany*

<sup>2</sup>*Lehrstuhl für Angewandte Festkörperphysik, Ruhr-Universität Bochum, 44780 Bochum, Germany<sup>†</sup>*

(Dated: July 24, 2024)

Electrostatic coupling between self-assembled quantum dots in different layers separated by approximately 200 nm is studied by transient capacitance spectroscopy. This coupling manifests itself via interdependent electron capture and emission transients, which include a counter-intuitive transient period in time where the quantum dots are filled in response to a depleting voltage pulse. A rate equation model combined with self-consistent band calculations explains the observation quantitatively in terms of a field effect that depends on the occupancy of the layers.

Self-assembled quantum dots (SAQDs) are quasi-zero dimensional semiconductor islands embedded in a semiconductor host crystal with a significantly different band structure, leading to charge confinement in the quantum dots.[1, 2] The energy spectra of such *artificial atoms* have been studied in great detail, both by optical as well as by electronic measurements, and the squared wave functions of the most relevant s - and p - states have been mapped out. Beyond fundamental research, [3–8] SAQDs have also found their way into significant applications,[9] in particular in single photon sources [10], light-emitting diodes [11]and, most prominently, as lasers in the telecom window.[12, 13]. Furthermore, their potential as memory cells [14–16] and in memristors [17] has been elucidated. In all these studies, the coupling of SAQD states to their environment is a key point, comprising, for example, coupling to photons, strong coupling to cavities in Rabi oscillators, or coupling to a reservoir via elastic tunneling. Also, quantum couplings between different SAQDs have been studied. For distances below  $\approx 10$  nm, quantum mechanical coupling can lead to the formation of artificial molecules [18–25] with the potential to enable quantum computation concepts.[26, 27]. At somewhat larger distances between SAQDs in two layers separated by  $\approx 20$  nm, electrostatic coupling between the dots has been reported, which can be described by a Coulomb blockade term.[28]

Here, we report the observation of electrostatic inter-dot coupling between SAQDs in adjacent layers with a large spatial separation of  $\approx 200$  nm, such that both correlated growth across the layers [29, 30] as well as electron tunneling between the dots [18–25] can be safely excluded. Since the layer spacing is also large compared to the intralayer spacing of SAQDs, the coupling has a different character as compared to those reported earlier and can be described by a mean field model. Large SAQD layer distances are present in a variety of structures like light-emitting diodes [31, 32], quantum dot lasers [33, 34] or solar cells[35, 36]. The interdot interaction is detected via modified capacitance transients which are no longer exponential. Based on a rate equation model, this coupling is interpreted in terms of an electric field at the site

of one layer, generated by the occupancy of the other layer.

The sample used in our study is depicted in Fig. 1. The relevant structure was grown on top of a GaAs single crystal substrate by molecular beam epitaxy. A 20 period GaAs/AlAs short-period superlattice (SPS) prevents diffusion of defects from the substrate into the critical structure and is followed by 50 nm undoped GaAs. A degenerately Si - doped (doping density  $2 \cdot 10^{18} \text{ cm}^{-3}$ ) layer of GaAs acts as back electrode and electron reservoir. On top of this layer, a 938 nm GaAs layer with a doping density of  $n_D = 7.0 \cdot 10^{15} \text{ cm}^{-3}$  is grown. Herein, two layers of InAs SAQDs are embedded at distances of 232 nm and 436 nm below the sample surface, which we denote by *top layer T* and *bottom layer B*. Each SAQD layer is surrounded by an undoped GaAs layer of 26 nm width. The SAQDs have a sheet number density of  $n_{QD} = 10^{14} \text{ m}^{-2}$ , which corresponds to approximately  $9 \times 10^6$  quantum dots in each layer underneath the active area of 0.3 mm x 0.3 mm, defined by a Cr/Au top electrode.

The experimental setup used for the transient capacitance spectroscopy has been described in detail elsewhere.[37] In brief, an AC test voltage with an amplitude of 10 mV and a frequency of 28 MHz was created by a HF2LI lock-in amplifier (Zurich Instruments), superimposed to a DC bias voltage (source: Keithley 3390) and applied to the top gate with respect to the back electrode, which was kept at virtual ground via a HF2TA transimpedance amplifier with  $Z = 1 \text{ k}\Omega$  (Zurich Instruments). Its out-of-phase voltage was read out from the lock-in amplifier via an oscilloscope, allowing a temporal resolution of the capacitance of 10  $\mu\text{s}$ . The sample was mounted into a liquid nitrogen cryostat, allowing measurements at a temperature of 77 K.

We study the capacitance transients in response to DC voltage steps, composed of a preparation voltage  $V_p$  of 10 ms duration, followed by a measurement voltage  $V_m$ , also applied for 10 ms. All combinations of  $V_m$  and  $V_p$  in the range  $V_{p,m} \in [-3.0 \text{ V}, 0.4 \text{ V}]$  are measured in steps of 40 mV. For each such combination of  $V_p$  and  $V_m$ , the capacitance transient is recorded during  $V_m$  and the *lock-in*

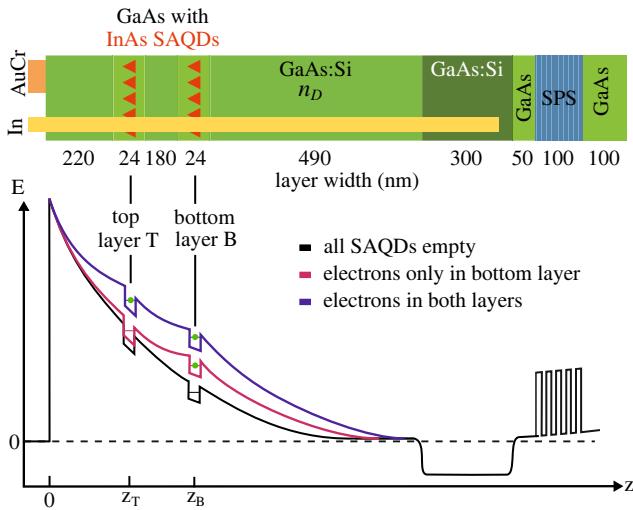


FIG. 1. Sketch of the sample layout (top) and schematic conduction band profile for various SAQD layer occupancies (bottom, the full green circles denote electrons). The dashed line denotes the Fermi level in the back contact.

signal, defined as

$$S = \frac{1}{P} \left( \int_0^{P/2} C(t) dt - \int_{P/2}^P C(t) dt \right) \quad (1)$$

is calculated, where  $P \leq 10$  ms is the rate window, i.e. the interval over which the transient is evaluated. In comparison to other evaluation technique, the lock-in deep level transient spectroscopy (DLTS) signal provides an excellent compromise between the required resolution and the measurement time in our experiments.

In Fig. 2 (a),  $S(V_p, V_m)$  as measured on the double layer sample at a temperature of 77 K is shown. Two narrow positive peaks are observed at  $V_m \approx -1.1$  V for preparation voltages below  $-1.2$  V and at  $V_m \approx +50$  mV for  $V_p \leq 0$  V. They correspond to capture of electrons in the bottom and the top layer, respectively, appearing in the half-plane  $V_m < V_p$ . In the regime  $V_m < -1.1$  V and  $V_p > -1.2$  V a broad negative signal is visible, which can be attributed to emission from the bottom layer, as been explained in detail elsewhere in terms of the voltage-dependent capture and emission rates which determine the measured time constants.[37] The capture signal from the top layer can be expected to be, to a first approximation, a replica of that one from the bottom layer, displaced along both voltage axes due to the different location of the layer. While the coarse appearance meets this expectation, pronounced deviations are visible: The emission extends over a larger  $V_m$  interval and does not show the characteristic fade-out as  $V_m$  decreases. Rather,  $S$  shows an approximately constant value for  $V_m \in [-1.5$  V,  $0.3$  V], interrupted by two minima of  $|S|$  centered at  $V_m = -0.3$  V and  $V_m = -0.9$  V. Some insight into the origin of this

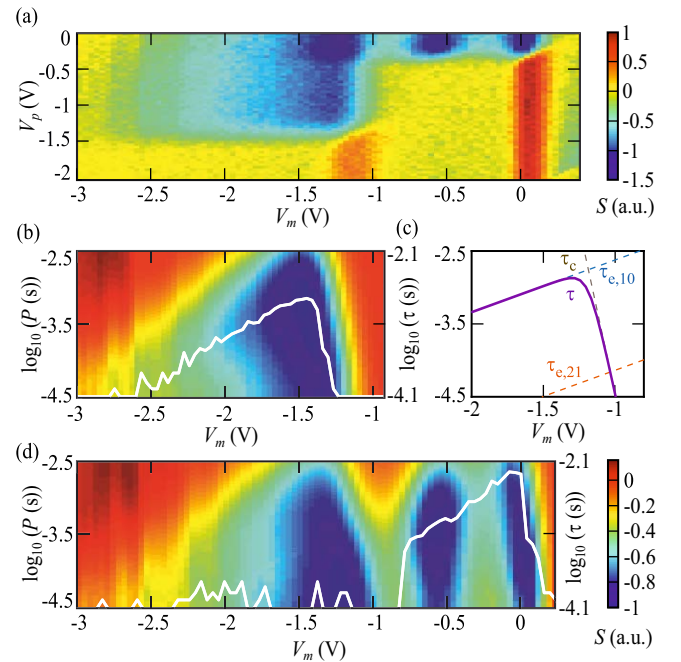


FIG. 2. (a) Color plot of the lock-in DLTS measurement at a temperature of 77 K at  $P = 1$  ms. (b) Lock-in DLTS data of the transients at  $V_p = -0.5$  V. The minima in  $S(\log(P))$  correspond to the decay time  $\tau$ , shown as a gray line. This represents the charge transfer dynamics of the bottom layer only, since the top layer has been prepared in an empty state. In (c), the composition of  $\tau(V_m)$  from the individual transfer time constants is shown. (d)  $S(V_m, \log(P))$  of the transients at  $V_p = 0.4$  V and the extracted values for  $\tau$ .

modulation can be obtained by studying the decay time  $\tau$  of the transients, which follows from the minimum of the lock-in DLTS signal as a function of the rate window  $P$ , i.e.  $P(S_{min}) = 0.398\tau$  as illustrated in Figs. 2 (b,c). In the emission regime of the bottom layer, as  $V_m$  is decreased below  $-1$  V after preparation at  $V_p = -0.5$  V,  $\tau$  increases sharply between  $-1.1$  V and  $-1.3$  V and then drops monotonously with decreasing measurement voltage, Fig. 2 (b). This well-understood behavior results from a sharp increase of the capture time in combination with weakly decreasing emission time as a function of decreasing  $V_m$ . [37] These relations are illustrated in the right part of Fig. 2 (b).

Applying this consideration to the emission from the top layer after preparation at  $V_p = 0.4$  V, see Fig. 2 (c), one observes that  $\tau$  follows the same behavior across the first minimum of  $|S|$  at  $V_m = -0.3$  V, but drops sharply to values below our time resolution (of about  $30 \mu\text{s}$ ) at the second minimum. This indicates that for  $V_m \in [-0.8$  V,  $0.3$  V] the modulation of  $S$  originates from a change of the capacitive sensitivity  $dC/dV$  rather than from a modification of the capture and emission rates. As will be shown below, the sharp drop of  $\tau$  between  $V_m = -0.8$  V and  $-1$  V originates from interlayer

coupling mediated by Coulomb interaction and is thus at our focus in the following. We note that a coupling by tunneling can be safely excluded considering the large distance as well as the greatly differing energies of the bound states.

In order to see how the occupation dynamics of the two layers contribute to the capacitance transients, a rate equation model is conceived. In accordance with results reported earlier, a maximum occupancy of two electrons per dot is considered, occupying the s-levels s1 and s2, with state-specific emission rates and a single capture rate, since capture into s1 and s2 cannot be resolved at 77 K. [37] The bias voltage dependence of all emission and capture rates  $e_{k,ij}$  and  $c_k$  have been modeled empirically by exponential functions,[37]

$$\begin{aligned} e_{k,ij}(V) &= \exp(\alpha_{k,ij} \cdot V + \beta_{k,ij}) s^{-1} \\ c_k(V) &= \exp(\gamma_k \cdot V + \chi_k) s^{-1} \end{aligned} \quad (2)$$

with the parameters  $\alpha_{k,ij}$  and  $\beta_{k,ij}$  for emission and  $\gamma_k$  as well as  $\chi_k$  for capture. Here, the index  $k \in \{T, B\}$  denotes the layer and  $i, j \in \{0, 1, 2\}$  are the corresponding occupation numbers of one SAQD.

The occupation dynamics of each layer in response to a bias pulse can be obtained by solving the corresponding system of rate equations,

$$\begin{aligned} \dot{n}_{k,0} &= -c_k \cdot n_{k,0} + e_{k,10} \cdot n_{k,1} \\ \dot{n}_{k,1} &= -c_k \cdot n_{k,1} + e_{k,21} \cdot n_{k,2} + c_k \cdot n_{k,0} - e_{k,10} \cdot n_{k,1} \\ \dot{n}_{k,2} &= c_k \cdot n_{k,1} - e_{k,21} \cdot n_{k,2} \end{aligned} \quad (3)$$

Here,  $n_{k,j}$  denote the densities of SAQDs in layer  $k$  with the occupation number  $j$ , and the dot denotes the derivative with respect to time. The parameters of the bottom layer are obtained by a least square fit of the analytic  $S(V_p, V_m)$  to the measured lock-in DLTS signal for  $V_p \leq -0.5$  V, where influences of the top layer are absent. In this regime, the top layer is empty and has no influence on the bottom layer. The fit results agree very well with those of a reference sample with identical layout,[37] except that the top layer is not embedded. For the top layer without interlayer coupling, we assume that the shape of  $S(V_p, V_m)$  is qualitatively identical and determine the corresponding parameters to match the positions of the capture peak and the onset of emission.

To incorporate electrostatic interlayer coupling into the model, we include the effect of a charge density  $\rho$  in one layer on the electric field in growth direction  $F(z)$  at the location of the other layer, see Fig. 3 (a). Addition of electrons to the SAQDs in the top layer increases  $|F(z_B)|$  as well as  $z_{dep}$ , the width of the space charge region. Therefore, the tunnel barrier of the bottom layer with an approximately triangular shape gets thinner and its emission rates increase. The capture, on the other hand, is dominated by diffusion of electrons from the

Layer	$\alpha_{10}[\text{V}^{-1}]$	$\beta_{10}$	$\alpha_{21}[\text{V}^{-1}]$	$\beta_{21}$	$\gamma[\text{V}^{-1}]$	$\chi$
t	-1.67	5.18	-1.41	8.35	21.02	7.19
b	-1.67	3.51	-1.41	6.94	21.02	28.21

TABLE I. Fit parameters obtained from the two single layers.

back contact.[38] The increased depletion region and the larger electric field correspond to a higher bottom layer potential, leading to a decrease of the capture rate. Since such a charge-induced shift  $\Delta F$  can be compensated by the bias voltage, we expect a displacement of the lock-in DLTS signal along the  $V_m$  axis without qualitative changes of its shape. Quantitatively, the transfer rates in layer  $k$  with the coupling to layer  $\ell$  taken into account is described by replacing the voltage  $V$  in Eqns.2 by  $V + \frac{dV}{d\rho_\ell} \cdot \rho_\ell$  with the charge density  $\rho_\ell$  in layer  $\ell$ . The coupling constant  $\frac{dV}{d\rho_\ell}$  is estimated with the help of a Poisson Schrödinger solver [39] to  $\pm \approx 50 \frac{\text{mV}}{\rho_\ell}$ , with "+" for  $\ell = B$  and "-" for  $\ell = T$ .

The system comprising the two coupled sets of rate equations were solved with the help of a Markov chain (see Ref. 37 for details). The capacitance transient is then calculated by

$$C(V, t) = \frac{\epsilon_r \epsilon_0 A \sqrt{q n_D}}{\sqrt{2[\epsilon_r \epsilon_0 (V_{bi} - V) - \rho_T(t) z_T - \rho_B(t) z_B]}} \quad (4)$$

The fit parameters are shown in Table I, and the fit results are summarized in Fig. 3.

As the top layer discharges in response to setting, for example,  $V_m$  to  $-1$  V after initializing the layers with  $V_p = +0.4$  V, the electric field  $F$  at the bottom layer drops and  $z_{dep}$  is reduced, see Fig. 3 (a). As a consequence, the capture rate of the bottom layer is increased, while its emission rates drop slightly (Fig. 3 (b)). Fig. 3 (c) shows the corresponding evolution of the layer occupancies. At the beginning of the relaxation,  $F(z_B)$  is larger as compared to the case of independent layers. Therefore, the emission rates of  $B$  are large and capture is suppressed. This causes a faster reduction of  $N_B$ . As the top layer empties, the rates of the bottom layer approach those in the decoupled case, which includes a time interval in which  $N_B$  increases despite the bias voltage pulse step towards depletion ( $t \approx 80 \mu\text{s}$  to  $\approx 500 \mu\text{s}$  in Fig. 3 (c)). In this time window, the decrease of  $F(z_B)$  by the depletion of the top layer dominates the transfer rates of the bottom layer over their still ongoing, transient response to the preceding bias voltage step. This leads to the computed overshoot in the time-dependence of  $N_B$ , the occupancy of the bottom layer. A similar line of arguing can be made for the influence of  $N_B(t)$  on  $N_T(t)$ . For comparison, the calculated exponential functions  $N_B(t)$  and  $N_T(t)$  in the absence of the interlayer coupling are shown in Fig. 3 (c) as well. Apparently, the emission from the top layer remains monotonous but is

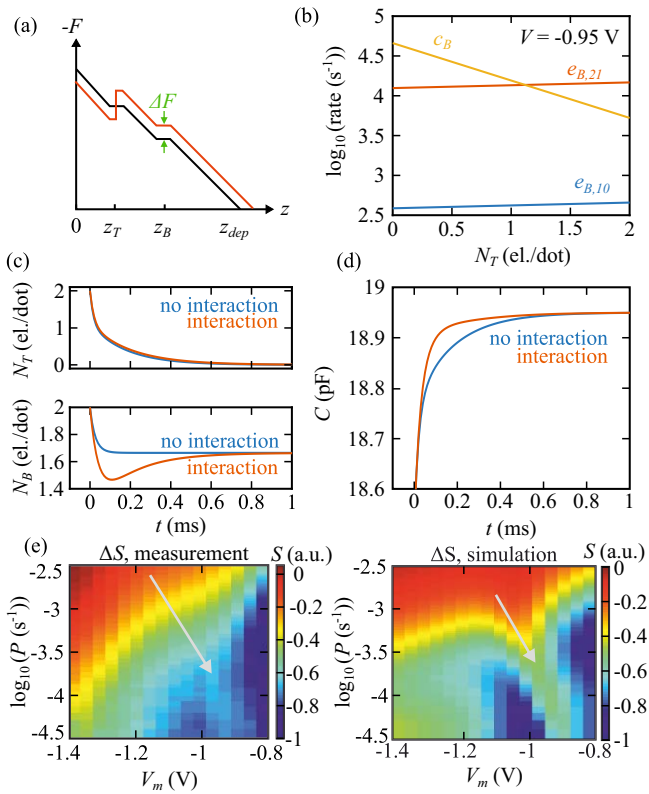


FIG. 3. (a) Sketch of the electric field distribution across the depletion layer for the occupied (red) and empty (black) top layer. The depletion of the top layer decreases  $F$  at  $z_B$ , which leads to faster capture due to the smaller activation energy and a somewhat slower emission as a consequence of the broader tunnel barrier (b). In (c), the calculated occupancy transients of both SAQD layers are shown after a preparation voltage of  $V_p = +0.4$  V at  $V_m = -1$  V. With the interlayer interaction disregarded, both layers show an exponential decay of the occupancy. The interaction causes  $N_B(t)$  to traverse a minimum at ( $t \approx 80 \mu\text{s}$ ), and  $N_T(t)$  to slow down slightly. Correspondingly, the capacitance transient decay faster with the interaction included (d). (e): Measured (left) and simulated (right) structure in  $S(V_m, P)$  for  $V_p = +0.4$  V. The interlayer interactions cause the minimum in  $S$  close to  $V_m = -1$  V which shifts to lower  $V_m$  as the rate window is increased.

decelerated somewhat by the interaction. This coupled SAQD depletion translates to a superexponential capacitance transient as shown in Fig. 3 (d), which can no longer be characterized by a single, effective time constant. However, the faster decay of  $C$  causes the amplitude of the lock-in DLTS signal to decrease, which generates the minimum in  $|S|$ . This structure in the  $(V_m, P)$  - plane is well reproduced by the model calculations, as shown in Fig. 3 (e), where the lock-in DLTS signal has been determined from the computed capacitance transients as they emerge from the rate equations, like the ones shown in Fig. 3 (d).

The visibility of this coupling depends sensitively on the

selected parameter values. As  $V_m$  is further decreased, for example, the interaction-induced suppression of the lock-in DLTS signal vanishes since the larger emission rates drive the overshooting transient of  $N_B(t)$  into a regime below our time resolution. Likewise, the location and the separation of the SAQD layers have a strong influence on the time scales and the amplitudes of the coupling effects. A systematic tuning of the transfer rates is possible by varying the temperature, which is however beyond our scope here.

The features of the lock-in DLTS signal at larger measurement voltages in the range of emission form the top layer originate from the flat band region approaching the bottom layer as  $V_m$  is increased. As detailed in the Supplement, this causes a pronounced increase of the capacitive sensitivity  $dC/dV_m$  which translates into an increasing lock-in DLTS signal that is neither related to the interlayer coupling nor to a non-monotonous evolution of the time constant. [40]

To conclude, the occupancy of self-assembled quantum dots may be felt by dots in layers at distances as large as 200 nm via Coulomb coupling. This manifests itself in modifications of the transients in response to bias voltage pulses, which can lead to unexpected behavior, in particular to transient periods of level filling after a pulse that empties the SAQDs. The capacitance transients develop a nonexponential shape which may approach faster their new stationary state. The time scale in which these effects are visible depends sensitively on the sample design as well as on the applied electric field. Experiments at lower temperatures and in optimized samples, which shed light on more advanced aspects like energy level-resolved contributions or elastic tunneling dominated emission, are a task for the future.

C.R.-E., S.S., A.D.W., and A.L. gratefully acknowledge the support of TRR 160/2-Project No. B04, Deutsche Forschungsgemeinschaft Grant No. 383065199, BMBF QR.X 16KISQ009 and the Deutsch-Französische Hochschule Grant No. CDEA-05-06.

\* thomas.heinzel@hhu.de

† Present address: DESY, Notkestr. 85, 22607 Hamburg, Germany

- [1] D. Leonard, M. Krishnamurthy, C. M. Reaves, S. P. Denbaars, and P. M. Petroff, Direct formation of quantum-sized dots from uniform coherent islands of In[Ga]As on GaAs surfaces, *Appl. Phys. Lett.* **63**, 3203 (1993).
- [2] P. M. Petroff, A. Lorke, and A. Imamoglu, Epitaxially Self-Assembled Quantum Dots, *Phys. Today* **54**, 46 (2001).
- [3] P. Michler, A. Kiraz, C. Becher, W. V. Schoenfeld, P. M. Petroff, L. Zhang, E. Hu, and A. Imamoglu, A quantum dot single-photon turnstile device, *Science* **290**, 2282 (2000).
- [4] M. Kroutvar, Y. Ducommun, D. Heiss, M. Bichler,

- D. Schuh, G. Abstreiter, and J. J. Finley, Epitaxially Self-Assembled Quantum Dots, *Nature* **432**, 81 (2004).
- [5] C. L. Salter, R. M. Stevenson, I. Farrer, C. Nicoll, D. A. Ritchie, and A. J. Shields, An entangled-light-emitting diode, *Nature* **465**, 594 (2010).
- [6] A. Faraon, A. Majumdar, D. Englund, E. Kim, M. Bajcsy, and J. Vuckovic, Integrated quantum optical networks based on quantum dots and photonic crystals, *New J. Phys.* **13**, 055025 (2011).
- [7] E. Waks, K. Inoue, C. Santori, D. Fattal, J. Vuckovic, G. S. Solomon, and Y. Yamamoto, Quantum cryptography with a photon turnstile, *Nature* **420**, 762 (2002).
- [8] J. Nilsson, R. M. Stevenson, K. H. A. Chan, J. Skiba-Szymanska, M. Lucamarini, M. B. Ward, A. J. Bennett, C. L. Salter, I. Farrer, D. A. Ritchie, and A. J. Shields, Quantum teleportation using a light-emitting diode, *Nature Photonics* **7**, 311 (2013).
- [9] D. J. Mowbray and M. S. Skolnick, New physics and devices based on self-assembled semiconductor quantum dots, *J. Phys. D: Appl. Phys.* **38**, 2059 (2005).
- [10] S. Buckley, K. Rivoire, and J. Vučković, Engineered quantum dot single-photon sources, *Rep. Prog. Phys.* **75**, 126593 (2012).
- [11] I. L. Krestnikov, N. A. Maleev, A. V. Sakharov, A. R. Kovsh, A. E. Zhukov, A. F. Tsatsulnikov, V. M. Ustinov, Z. I. Alferov, N. N. Ledentsov, D. Bimberg, and J. A. Lott, 1.3  $\mu\text{m}$  resonant-cavity InGaAs/GaAs quantum dot light-emitting devices, *Semicond. Sci. Technol.* **16**, 8844 (2001).
- [12] V. M. Ustinov, N. A. Maleev, A. E. Zhukov, A. R. Kovsh, A. Y. Egorov, A. V. Lunev, B. V. Volovik, I. L. Krestnikov, Y. G. Musikhin, N. A. Bert, P. S. Kopev, and Z. I. Alferov, InAs/InGaAs quantum dot structures on GaAs substrates emitting at 1.3  $\mu\text{m}$ , *Appl. Phys. Lett.* **74**, 2815 (1999).
- [13] E. U. Rafailov, M. A. Cataluna, and W. Sibbett, Mode-locked quantum-dot lasers, *Nature Photonics* **1**, 395 (2007).
- [14] M. Geller, A. Marent, T. Nowozin, and D. Bimberg, Self-organized quantum dots for future semiconductor memories, *J. Phys. Cond. Mat.* **20**, 454202 (2008).
- [15] T. Nowozin, A. Marent, M. Geller, D. Bimberg, N. Akcay, and N. Öncan, Temperature and electric field dependence of the carrier emission processes in a quantum dot-based memory structure, *Appl. Phys. Lett.* **94**, 042108 (2009).
- [16] A. Marent, T. Nowozin, M. Geller, and D. Bimberg, The qd-flash: a quantum dot-based memory device, *Semicond. Sci. Technol.* **26**, 014026 (2011).
- [17] P. Maier, F. Hartmann, M. Emmerling, C. Schneider, M. Kamp, S. Hofling, and L. Worschech, Electro-photo-sensitive memristor for neuromorphic and arithmetic computing, *Phys. Rev. Appl.* **5**, 054011 (2016).
- [18] P. Boucaud, J. B. Williams, K. S. Gill, M. S. Sherwin, W. V. Schoenfeld, and P. M. Petroff, Terahertz-frequency electronic coupling in vertically coupled quantum dots, *Appl. Phys. Lett.* **77**, 4356 (2000).
- [19] M. Bayer, P. Hawrylak, K. Hinzer, S. Fafard, M. Korkusinski, Z. R. Wasilewski, O. Stern, and A. Forchel, Coupling and entangling of quantum states in quantum dot molecules, *Science* **291**, 451 (2001).
- [20] H. W. Ren, S. V. Nair, J. S. Lee, S. Sugo, and Y. Matsumoto, Photoluminescence of strain-induced coupled InGaAs/GaAs quantum-dot pairs, *J. Electron. Mat.* **29**, 529 (2000).
- [21] M. Korkusinski and P. Hawrylak, Electronic structure of vertically stacked self-assembled quantum disks, *Phys. Rev. B* **63**, 195311 (2001).
- [22] D. G. Austing, S. Tarucha, H. Tamura, K. Muraki, F. Ancilotto, M. Barranco, A. Emperador, R. Mayol, and M. Pi, Integer filling factor phases and isospin in vertical diatomic artificial molecules, *Phys. Rev. B* **70**, 045324 (2004).
- [23] P. Miska, J. Even, C. Panthoën, and O. Dehaese, Vertical electronic coupling between InAs/InP quantum-dot layers emitting in the near-infrared range, *Appl. Phys. Lett.* **86**, 111905 (2005).
- [24] F. Yuan, Z. Jiang, and F. Lu, Study of coupling effect in double-layer quantum dots by admittance spectroscopy, *Appl. Phys. Lett.* **89**, 072112 (2006).
- [25] S. M. Reimann and M. Manninen, Electronic structure of quantum dots, *Rev. Mod. Phys.* **74**, 1283 (2002).
- [26] D. Loss and D. P. DiVincenzo, Quantum computation with quantum dots, *Phys. Rev. A* **57**, 120 (1998).
- [27] O. Gywat, G. Burkard, and D. Loss, Biexcitons in coupled quantum dots as a source of entangled photons, *Phys. Rev. B* **65**, 205329 (2002).
- [28] R. J. Luyken, A. Lorke, M. Fricke, J. P. Kotthaus, G. Medeiros-Ribeiro, and P. Petroff, Coulomb-coupling in vertically aligned self-assembled InAs quantum dots, *Nanotechnology* **10**, 14 (1999).
- [29] G. Springholz, V. Holy, M. Pinczolits, and G. Bauer, Self-organized growth of three-dimensional quantum-dot crystals with fcc-like stacking and a tunable lattice constant, *Science* **282**, 734 (1998).
- [30] D. Grigoriev, M. Schmidbauer, P. Schäfer, S. Besedin, Y. I. Mazur, Z. M. Wang, G. J. Salamo, and R. Köhler, Three-dimensional self-ordering in an InGaAs-GaAs multilayered quantum dot structure investigated by x-ray diffuse scattering, *J. Phys. D: Appl. Phys.* **38**, A154 (2005).
- [31] Y. K. Su, S. J. Chang, L. W. Ji, C. S. Chang, L. W. Wu, W. C. Lai, T. H. Fang, and K. T. Lam, InGaN/GaN blue light-emitting diodes with self-assembled quantum dots, *Semicond. Sci. Technol.* **19**, 389 (2003).
- [32] J. Chen, Q. Zhao, B. Yu, and U. Lemmer, A Review on Quantum Dot-Based Color Conversion Layers for Mini/Micro-LED Displays: Packaging, Light Management, and Pixelation, *Adv. Opt. Materials* **12**, 2300873 (2023).
- [33] R. A. Abbas, Y. M. Sabry, H. Omran, Z. Huang, M. Zimmer, M. Jetter, P. Michler, and D. Khalil, Modelling and experimental characterization of double layer InP/AlGaInP quantum dot laser, *Opt. and Quant. Electron.* **65**, 205 (2024).
- [34] Q. Li, X. Wang, H. M. Chen, Y. Huang, C. Hou, J. Wang, R. Zhang, J. Ning, J. Min, C. C. Zheng, and Z. Zhang, Development of modulation p-doped 1310 nm InAs/GaAs quantum dot laser materials and ultrashort cavity Fabry-Perot and distributed-feedback laser diodes, *ACS Photonics* **5**, 1084 (2018).
- [35] T. Sugaya, O. Numakami, R. Oshima, S. Furue, H. Komaki, T. Amano, K. Matsubara, Y. Okano, and S. Niki, Ultra high stacks of InGaAs/GaAs quantum dots for high efficiency solar cells, *Energy Environ. Sci.* **5**, 6233 (2012).
- [36] S. M. Hubbard, C. D. Cress, C. G. Bailey, R. P. Raffaele, S. G. Bailey, and D. M. Wilt, Effect of strain compensation on quantum dot enhanced GaAs solar cells, *Appl. Phys. Lett.* **92**, 123512 (2008).

- [37] L. Schnorr, J. Labes, L. Kurten, T. Heinzl, C. Rothfuchs-Engels, S. Scholz, A. Ludwig, and A. D. Wieck, Electron capture and emission dynamics of self-assembled quantum dots far from equilibrium with the environment, *Phys. Rev. B* **104**, 035303 (2021).
- [38] L. Berg, L. Schnorr, J. Wilkens, T. Heinzl, C. Rothfuchs-Engels, S. Scholz, A. Ludwig, and A. D. Wieck, Electron capture dynamics into self-assembled quantum dots far from equilibrium with their environment, *Phys. Rev. B* **109**, 235433 (2024).
- [39] G. Snider, 1D Poisson-Schrödinger solver (2017), [Accessed on Sep 15<sup>th</sup>, 2017].
- [40] See Supplemental Material at [URL will be inserted by publisher] for details.

# Electrostatic inter-layer coupling between self-assembled quantum dots

L.Berg,<sup>1</sup> L. Schnorr,<sup>1</sup> T. Heinzl,<sup>1</sup> C. Rothfuchs-Engels,<sup>2</sup> N. Barth,<sup>2</sup> A. Ludwig,<sup>2</sup> and A. D. Wieck<sup>2</sup>

<sup>1</sup>*Solid State Physics Laboratory, Heinrich-Heine-Universität Düsseldorf, 40204 Düsseldorf, Germany*

<sup>2</sup>*Lehrstuhl für Angewandte Festkörperphysik, Ruhr-Universität Bochum, 44780 Bochum, Germany*

(Dated: July 24, 2024)

This supplement contains standard characterization measurements of the heterostructure that hosts the two layers of self-assembled quantum dots (IV- and CV - characteristics as well as the determination of the doping density). The plots of the fit function  $S(V_p, V_m)$  for the transfer dynamics of the bottom layer, which is used to obtain the parameters of the individual layers, are reproduced. Furthermore, the experimental evidence for the modified capacitive sensitivity at voltages around -550 mV is documented.

## CURRENT-VOLTAGE AND CAPACITANCE-VOLTAGE CHARACTERISTICS

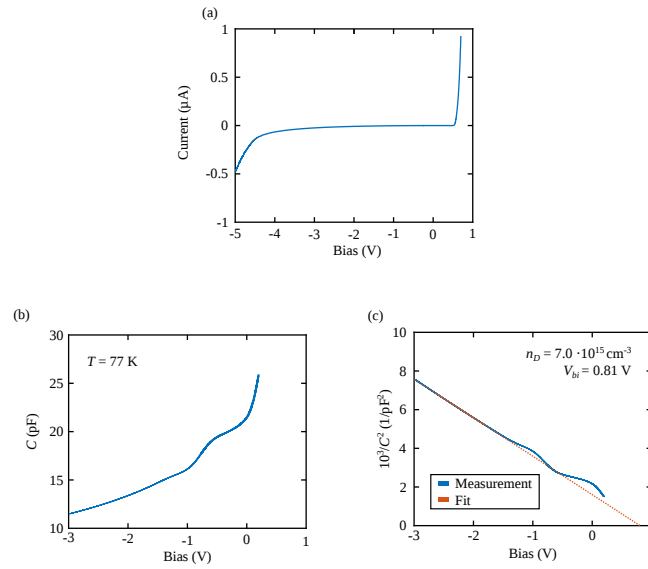


FIG. 1. Current-voltage (a) and capacitance-voltage (b) characteristics as obtained at 77 K. The SAQD layers are reflected in the two peaks in the CV trace, which are weak at the frequency of 28 MHz used here. The corresponding Mott-Schottky plot, reproduced in (c), gives the doping density  $n_D$  that has been used in the modeling of the sample. The built-in voltage of +0.81 V is found.



RATE EQUATION PARAMETER VALUES FOR THE BOTTOM LAYER

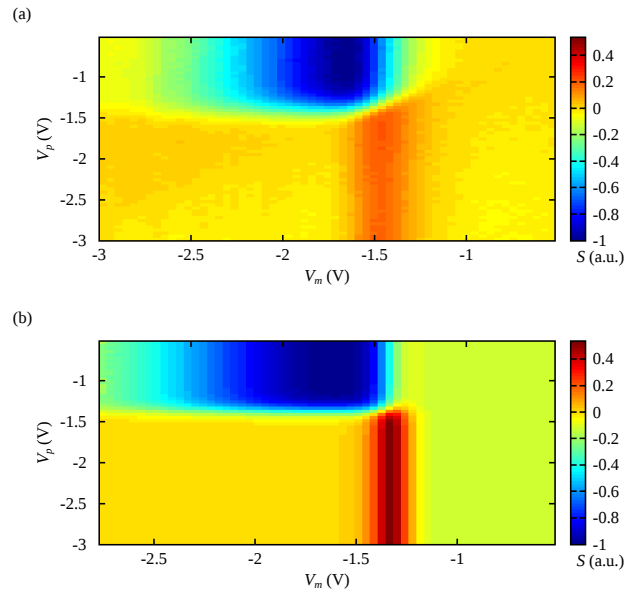


FIG. 2. (a) Measured DLTS lock-in signal of the top layer sample for low values of  $V_p$  where the top layer is empty. (b) Fit the measurement in (a), leading to the parameter values in the rate equations for the bottom layer.

For the bottom layer a least squares fit was carried out. Only the section where the top layer is empty was considered. A time window of  $P = 10$  ms was chosen. The result of the fit and the fit parameter values are shown in Fig. 2 and Table 1, respectively.

Layer	$\alpha_{10} [V^{-1}]$	$\beta_{10}$	$\alpha_{21} [V^{-1}]$	$\beta_{21}$	$\gamma [V^{-1}]$	$\chi$
b	-1.65	4.39	-1.65	7.7	21.62	31.289

TABLE I. Fit parameter values obtained for the bottom layer.

### RATE EQUATION PARAMETERS FOR THE TOP LAYER

For long rate windows, the visibility of the coupling effect is reduced and the sensitivity enhancement due to the bottom layer approaching the back electrode is reduced, as can be seen in Fig. 4. We therefore plot the lock-in signal of in the region where the top layer is active in Fig. 3 (a) for  $P = 10$  ms to estimate the parameter values for the top layer in the absence of interlayer coupling. The parameter values chosen are listed in Table 2 and result in the simulated lock-in signal shown in Fig. 3 (b).

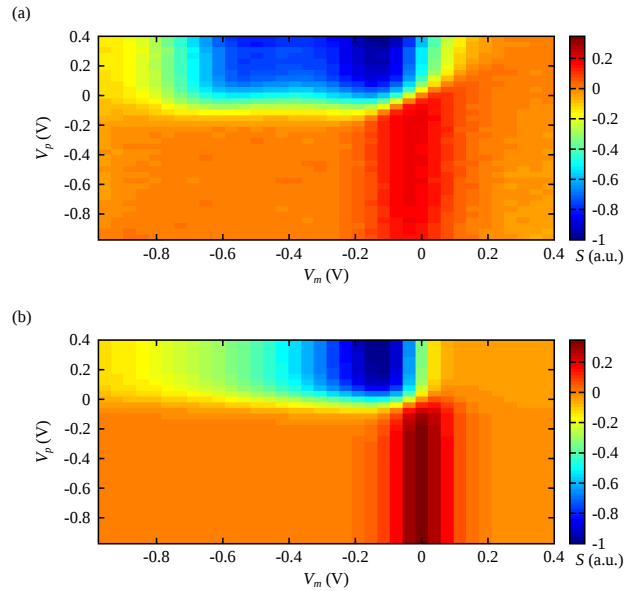


FIG. 3. (a)  $S(V_p, V_m)$  for high preparation voltages at a rate window of  $P = 10$  ms. (b) Simulated lock-in signal of this region for the estimated parameter values as given in Table 2.

Layer	$\alpha_{10}[\text{V}^{-1}]$	$\beta_{10}$	$\alpha_{21}[\text{V}^{-1}]$	$\beta_{21}$	$\gamma[\text{V}^{-1}]$	$\chi$
t	-1.65	7.03	-1.65	9.41	21.62	6.21

TABLE II. Estimated parameter values for the layer.

## DEPENDENCE OF $S$ ON THE RATE WINDOW OVER THE FULL PARAMETER RANGE

As pointed out in the main text, the visibility of the interlayer Coulomb interaction depends sensitively on the measurement parameters chosen. This becomes apparent in a study of the dependence of the lock-in signal on the rate window. Besides the interaction - induced structure close to  $V_m = -1V$  at small rate windows, the signal shows a pronounced structure at larger measurement voltages which does not correlate with the decay time of the transient and is attributed to an enhancement of the capacitive sensitivity in the main text as well as below.

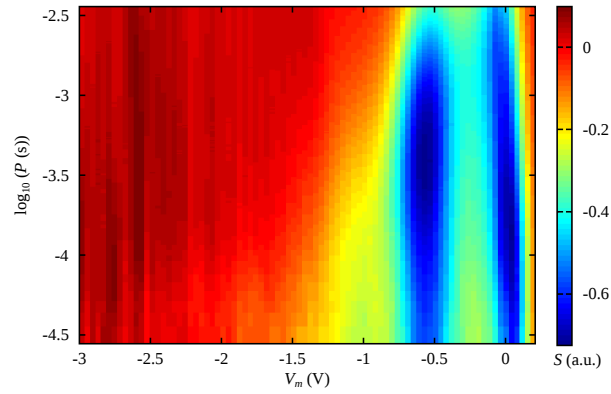


FIG. 4.  $S(V_m, P)$  after preparing the sample at  $V_p = +0.4V$ .

NUMERICAL STUDY OF THE DEPLETION WIDTH AND THE INFLUENCE ON  $dC/dV$

In Fig. 5 (a), the change of the depletion width as a function of the bias voltage, as obtained from the Poisson-Schrodinger solver, is shown. It translates into the differential capacitance as reproduced in Fig. 5(b) and explains the negative peak in  $S$  around  $V_m = -0.6$  V as seen in Fig. 4.

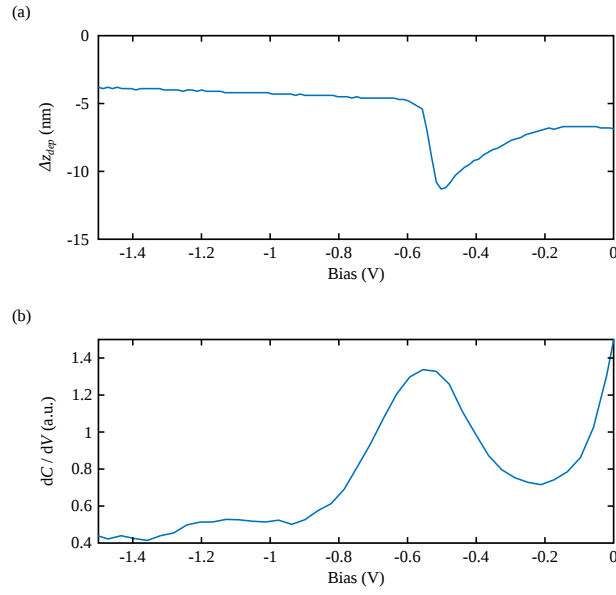


FIG. 5. (a) Computed change in the width of the depletion region and the corresponding structure of the thereby generated differential capacitance  $dC/dV$  (b).

---

## Chapter 6

# Deep level transient photocapacitance spectroscopy

DLTS is a powerful method for characterising deep level traps, as outlined in the chapter 3. However, DLTS is not suitable for all samples, in particularly those with significant recapture [65] or deep level traps that only thermally emit their charge carriers at high temperatures [63]. To address specific requirements, a variety of alternative techniques have been established [34, 63, 107, 171]. In *Paper IV* the deep level transient photocapacitance spectroscopy is presented. This is a method to extract the parameters of deep level traps from temperature dependent photocapacitance transients. In particular it is shown that the capture cross section can be extracted by an optical method. The oxygen vacancy of rutile  $\text{TiO}_2$  acted as a model trap for the development. An optical transparent rNM allowed for a high illumination rate. The rNM formed a  $\text{Au/TiO}_2$  Schottky junction, a detailed description of the sample can be found in section 2.2.3. The parameters have been extracted by fitting to a set of rate equations. The fit gives information about the binding energy, the capture cross section, the optical emission rate as well as information about the capture process. The extracted values are consistent with those obtained from DLTS.

---

## 6.1 Paper IV

### Reference

Reproduced from [Berg, L. and Schnorr, L and Merces, L and Bettini, J and Bof Bufon, CC and Heinzl, T, "Transient photocapacitance spectroscopy on Au/TiO<sub>2</sub> Schottky diodes with rolled-up nanomembrane electrodes", Journal of Applied Physics **133**, 065704 (2023) <https://doi.org/10.1063/5.0132445>], with the permission of AIP Publishing

### Copyright statement

Authors do not need permission from AIP Publishing to reuse your own AIP Publishing article in your thesis or dissertation.

### Contributions

I planned and conducted most of the experiments and analysed most of the data. I contributed to manuscript writing.

---

# Transient photocapacitance spectroscopy on Au/TiO<sub>2</sub> Schottky diodes with rolled-up nanomembrane electrodes

Cite as: J. Appl. Phys. **133**, 065704 (2023); <https://doi.org/10.1063/5.0132445>

Submitted: 28 October 2022 • Accepted: 24 January 2023 • Published Online: 14 February 2023

 L. Berg,  L. Schnorr,  L. Mercas, et al.



View Online



Export Citation



CrossMark

## ARTICLES YOU MAY BE INTERESTED IN

[Influence of boron implantation induced defects on solar cells: Modeling the process defects](#)

Journal of Applied Physics **133**, 065703 (2023); <https://doi.org/10.1063/5.0130315>

[Polarized emission from hexagonal-silicon-germanium nanowires](#)

Journal of Applied Physics **133**, 065702 (2023); <https://doi.org/10.1063/5.0135215>

[Impedance modeling for excluding contact resistance from cross-plane electronic conductivity measurement of anisotropic two-dimensional Ti<sub>3</sub>C<sub>2</sub>T<sub>x</sub> MXenes](#)

Journal of Applied Physics **133**, 065304 (2023); <https://doi.org/10.1063/5.0138387>



Time to get excited.  
Lock-in Amplifiers – from DC to 8.5 GHz

Find out more

Zurich Instruments

# Transient photocapacitance spectroscopy on Au/TiO<sub>2</sub> Schottky diodes with rolled-up nanomembrane electrodes

Cite as: J. Appl. Phys. 133, 065704 (2023); doi: 10.1063/5.0132445

Submitted: 28 October 2022 · Accepted: 24 January 2023 ·

Published Online: 14 February 2023



L. Berg,<sup>1</sup> L. Schnorr,<sup>1</sup> L. Mercas,<sup>2</sup> J. Bettini,<sup>3</sup> C. C. Bof Bufon,<sup>4</sup> and T. Heinzl<sup>1,a)</sup>

## AFFILIATIONS

<sup>1</sup>Solid State Physics Laboratory, Heinrich-Heine-Universität Düsseldorf, 40204 Düsseldorf, Germany

<sup>2</sup>Material Systems for Nanoelectronics, Chemnitz University of Technology, 09107 Chemnitz, Germany and “Gleb Wataghin” Institute of Physics, University of Campinas, 13083-859 Campinas, SP, Brazil

<sup>3</sup>Brazilian Nanotechnology National Laboratory, Brazilian Center for Research in Energy and Materials, 13083-100 Campinas, SP, Brazil

<sup>4</sup>Mackenzie Presbyterian Institute, Mackenzie Institute for Research in Graphene and Nanotechnologies—MackGraphe, 01302-907 São Paulo, SP, Brazil

<sup>a)</sup>Author to whom correspondence should be addressed: [thomas.heinzl@hhu.de](mailto:thomas.heinzl@hhu.de)

## ABSTRACT

Rolled-up nanomembrane electrodes are used to prepare optically transparent Au/TiO<sub>2</sub> Schottky diodes suitable for deep level transient photocapacitance spectroscopy. It is demonstrated that both the binding energy and the capture cross section of the oxygen vacancy can be extracted from the photocapacitance transients using a rate equation model. The values are consistent with those obtained from conventional deep level transient spectroscopy, taken from the same sample. Furthermore, information about the capture process can be extracted.

Published under an exclusive license by AIP Publishing. <https://doi.org/10.1063/5.0132445>

## I. INTRODUCTION

Deep level transient spectroscopy (DLTS)<sup>1</sup> has proven to be a useful technique for determining parameters of traps in insulators, such as binding energies, cross sections, or number densities of the charge traps. Striking results have been obtained in the fields of doped or irradiated semiconductors, solar panels, or self-assembled quantum dots, to name just a few.<sup>2–15</sup> Since the first appearance of DLTS, almost 50 years ago, a large number of related methods have been developed extending the range of applications and taking into account the specific requirements of the material under study. The concept has been, for example, extended to conductivity experiments,<sup>16,17</sup> inverse Laplace transformations of the transients,<sup>18</sup> or to capacitance transients under optical excitations,<sup>19–21</sup> which are particularly suited for levels deep inside the bandgap with small thermal activation rates. However, not all quantities of interest are accessible by each measurement concept, and the versatility of one method depends on the set of quantifiable parameters. Here, using the well-known oxygen vacancy in rutile titanium dioxide as a model trap, we show that the electron capture cross section can be

determined by optical methods as well, namely, by deep level transient photocapacitance spectroscopy (DLTPCS) in combination with a rate equation model. The extracted parameter values are in agreement with those obtained by conventional lock-in DLTS.<sup>22,23</sup> This comparison is made possible by using *rolled-up nanomembrane* (rNM) electrodes,<sup>24–26</sup> which act as optically transparent gates<sup>27</sup> of the Au/TiO<sub>2</sub> Schottky diodes.

## II. SAMPLE PREPARATION, EXPERIMENTAL METHODS, AND CHARACTERIZATION

Rolled-up nanomembrane (rNM) vertical junctions were fabricated on SiO<sub>2</sub>-coated (2 μm thick), 8 × 8 mm<sup>2</sup> Si (100) substrates. The device fabrication relies on photolithography, thin-film deposition, and etching methods, as recently reported elsewhere.<sup>25,26</sup> The preparation procedure is depicted in Fig. 1.

The vertical junctions are composed of a patterned Ni bottom electrode, a TiO<sub>2</sub> thin film playing the role of active material, and an rNM Au top electrode. The Ni and Au electrodes were deposited by electron-beam evaporation in an AJA International system



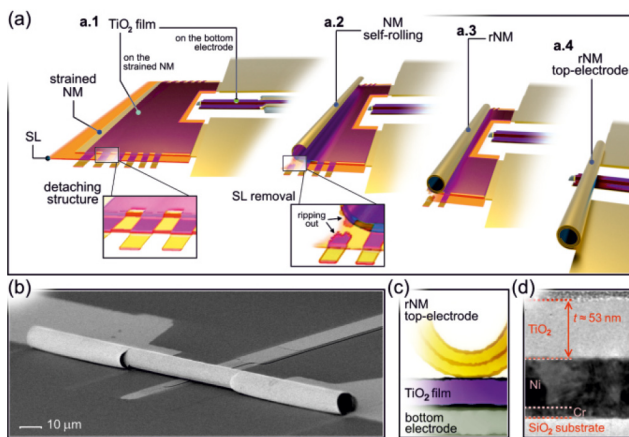


**FIG. 1.** Device architecture and electron microscopy images. (a) Schematics of (a.1) device patterning, (a.2) NM release from the substrate, (a.3) an rNM micro-tubular shape, and (a.4) an rNM-based vertical junction. The zoom-in insets, a.1 and a.2, illustrate the TiO<sub>2</sub> detaching structure and its ripping out, respectively, during the SL removal. (b) SEM image of the as-fabricated device. (c) Illustration of the rNM device cross-sectional view, showing the Cr/Ni bottom electrode, the TiO<sub>2</sub> film, and the Au-covered rNM top electrode. (d) Cross-sectional TEM image of the Cr/Ni/TiO<sub>2</sub> structure, which the rNM electrode is going to land on top. The TEM image was acquired from a lamella sample prepared using FIB.

in high vacuum ( $\approx 10^{-7}$  Torr) and with substrates kept at room temperature. The TiO<sub>2</sub> film was grown by atomic layer deposition (ALD) on the patterned Ni bottom electrode. The ALD process was carried out using a calibrated Oxford OpAL reaction chamber with titanium (IV) isopropoxide (TTIP) and H<sub>2</sub>O as a precursor. The substrate was kept at 150 °C during the TiO<sub>2</sub> deposition. This material was selected for our experiment since it contains a well-known deep level originating from a single oxygen vacancy, labeled as  $V_O$ . Such a level has a binding energy around 800 meV and acts predominantly as an electron emitter.<sup>28–30</sup> It is, thus, sufficiently deep for an unambiguous detection by optical spectroscopy but still accessible by conventional DLTS. To pattern the TiO<sub>2</sub> films (viz. on the bottom electrode and the strained nanomembrane), we employed reactive-ion etching (RIE), using a Plasma Pro NGP80 (Oxford Instruments). After the TiO<sub>2</sub> thin-film patterning, the roll-up process was carried out to form Ni/TiO<sub>2</sub>/Au vertical junctions. The interface at the bottom has an area of  $80 \times 10 \mu\text{m}^2$ , while the contact area of the interface at the top is  $10 \mu\text{m}$  times the contact length of the rolled-up electrode, which has previously been estimated to  $\approx 0.1 \mu\text{m}$ .<sup>31</sup> To a good approximation, both the top and bottom electrodes form a parallel plate capacitor with the TiO<sub>2</sub> layer as the dielectric material, arranged in parallel to the capacitance from the junction.

The roll-up process employed here is a controlled release of a Cr/Ti strained nanomembrane (NM) from the SiO<sub>2</sub> substrate by means of the GeO<sub>x</sub> sacrificial layer (SL) removal,<sup>25</sup> as illustrated by the sequential sketches in Fig. 1. The strained NM was patterned together with an Au thin film that is going to play the role of a top

electrode after the roll-up process. On the top of the strained NM, a TiO<sub>2</sub> detaching structure was patterned to direct the NM release from the substrate. Within this framework, the SL selective removal triggers the strained NM release, which is directed by the detaching structure ripping out [Fig. 1(a)]. The strained NM proceeds curling itself up until forming a rolled-up Au-coated microtube. Still, the Au-coated microtube continues to roll until the rNM lands on the TiO<sub>2</sub> thin film, providing a reliable electrical top-contact for the vertical junction. Figure 1(b) shows a scanning electron microscope (SEM) image of the device architecture in which the rNM is contacting the TiO<sub>2</sub> film from the top, forming a cross-wire-like junction with the Ni layer as a bottom electrode. The reasons an rNM was chosen over a conventional flat wire contact lie in its optical properties. Incident photons are guided alongside the outer wall of the rNM all the way to the back of the microtube where they illuminate the oxide directly underneath the metal,<sup>25,26</sup> thus resembling a whispering gallery mode.<sup>32</sup> After device manufacturing, the rNM vertical junctions were stored in a high vacuum (base pressure  $\approx 10^{-5}$  Torr) for at least 24 h to remove any water residue incorporated during the fabrication.

The sample morphology was characterized using optical and electron microscopy techniques. The optical microscopy images were acquired using a Nikon Eclipse ME600 microscope. The SEM images were acquired using an FEI Inspect F50 (viz. for imaging the entire device architecture). Transmission electron microscopy (TEM), annular dark field scanning transmission electron microscopy (ADF-STEM), and energy dispersive spectroscopy (EDS) were employed to elucidate the device morphology. The TEM and ADF-STEM images were acquired using a JEOL JEM 2100F. The EDS maps were obtained using an OXFORD EDS System with a 100 mm<sup>2</sup> SDD coupled to the electron microscope. The lamella samples were prepared by a focused ion beam (FIB) using a HELIOS NanoLab 660, and Au thermally evaporated electrodes were employed to guarantee reproducibility in both FIB preparation and TEM imaging. These studies have revealed that our TiO<sub>2</sub> films crystallize in the rutile structure and have a thickness of  $(53 \pm 2)$  nm (see the supplementary material). The layer sequence is expected to form an n-type Schottky diode since the Ni/TiO<sub>2</sub> interface is known to form an Ohmic contact,<sup>33</sup> while the Au/TiO<sub>2</sub> interface forms a Schottky barrier for sufficiently low defect densities.<sup>34</sup>

The sample was mounted into a liquid nitrogen cryostat (Linkam HFS 600 with cooling unit LNP 95), which enables a temperature range from 150 K to 450 K. A dry nitrogen atmosphere is established by a constant flow of nitrogen gas via a gas flow controller (Bronkhorst EL-Flow series).

The capacitance of the sample was measured with the setup shown in Fig. 2(a). An AC excitation voltage with an amplitude of 100 mV and a frequency of approximately 28 MHz was generated by a HF2LI Zürich Instruments Lock-in amplifier and superimposed to the output of an arbitrary waveform generator (AWG, Keithley 3390). This relatively high frequency was used in order to obtain an acceptable signal-to-noise ratio for subsequent data analysis. The corresponding implications for the measured values of the Schottky barrier height and the doping density, both of which enter only qualitatively in our analysis, are discussed in the supplementary material. The bias voltage was applied to the top

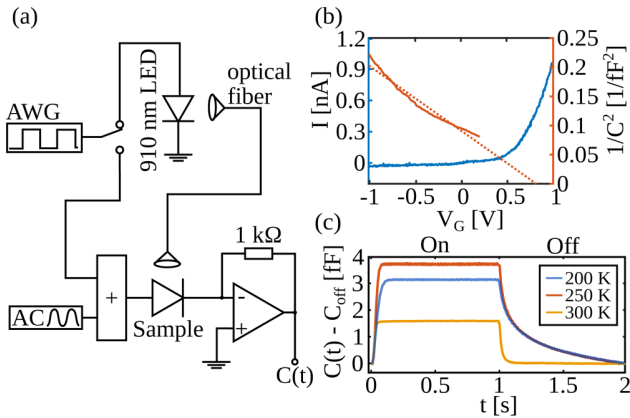


**FIG. 2.** (a) Scheme of the capacitance measurement setup. The rectangular pulse train emitted by the arbitrary wave form generator (AWG) is applied either directly to the gate electrode of the sample or to the LED, and the current with a phase shift of  $\pi/2$  with respect to the excitation is measured with a transimpedance amplifier. (b) DC current (blue) and squared inverse capacitance (full red) of the structure as a function of the gate voltage (Mott-Schottky plot) and the corresponding linear fit (dashed red line). (c) Transient capacitance response of the sample to the onset and the shut-off of the illumination for three different temperatures.

electrode with respect to the Ni electrode, grounded virtually via the HF2TA transimpedance amplifier. The out-of-phase signal, measured with the lock-in amplifier, represents the capacitance, which can be measured with a time resolution of  $10\mu\text{s}$ . A Picoscope 5444B digital oscilloscope was used to measure and average the transients.

For the conventional DLTS measurements, a rectangular bias pulse with a frequency of 1 Hz and an amplitude of 1 V was applied. In a temperature range from 200 to 350 K, the capacitance transients were recorded during the emission state, defined by the bias voltage level of  $-1\text{ V}$ , using a heating rate of  $2\text{ K min}^{-1}$ . Each transient was averaged over 50 individual traces, leading to an acceptable signal-to-noise ratio. The data were processed using the lock-in DLTS function  $S(P, T)$  given by<sup>23</sup>

$$S(P, T) = \frac{1}{P} \left( \int_0^{P/2} C(t) dt - \int_{P/2}^P C(t) dt \right), \quad (1)$$

where  $C$  denotes the differential capacitance and  $P$  is the time interval over which the transient is evaluated, varying from  $500\mu\text{s}$  to 1 s. Its maximum value is linked to the lifetime of the transient by the relation  $\tau = 0.398P$ .

To characterize the junction, current-voltage as well as capacitance-voltage measurements were carried out using the setup as exemplified in Fig. 2(b). The current-voltage characteristic reveals a rectifying relation. At applied voltages above 0.5 V, the trace is approximately linear, corresponding to the case that the current flow is limited by the bulk resistance rather than the rectifying junction. The resistivity is  $1.1 \times 10^5 \Omega\text{m}$ , orders of magnitude

below the value for intrinsic rutile, indicating a large doping density, but still small enough to form a Schottky barrier. To a reasonable approximation, the rolled-up nanomembrane electrode and the Ni layer form a parallel plate capacitor with the  $\text{TiO}_2$  layer as the dielectric material. The capacitance contribution of the sample can be estimated to 13 fF. This corresponds, for an estimated dielectric constant of 80, to an effective contact width of  $\approx 100\text{ nm}$ . The built-in potential as determined from the Mott-Schottky analysis amounts to  $V_{bi} \approx 0.89\text{ V}$  (see the supplementary material), using an effective electron mass of  $m_{\text{rutile}}^* = 20 m_e$ ,<sup>35</sup> where  $m_e$  denotes the free electron mass. The doping density is found to be  $n_D \approx 4.2 \times 10^{19} \text{ cm}^{-3}$ . The traces are consistent with the picture of an n-type Schottky junction, even at the selected measurement frequency.

In Fig. 3, the lock-in DLTS function  $S(P, T)$  according to Eq. (1) is plotted vs the temperature in a color scale representation. A single peak is visible in the spectrum. Its positive amplitude indicates that here, majority carriers are emitted from an n-type trap.<sup>1</sup> A fit of the data in the form of an Arrhenius plot according to the Richardson equation

$$e_{th} = \frac{2\sqrt{3}(2\pi)^{1.5} m_{\text{rutile}}^* \sigma_c (k_B T)^2 \exp\left(\frac{-E_b}{k_B T}\right)}{h^3}, \quad (2)$$

where  $\sigma_c$  denotes the capture cross section and  $e_{th}$  is the thermal emission rate, gives a binding energy of  $E_b = 898 \pm 20 \text{ meV}$  and a relatively large capture cross section of  $\sigma_c = (7.8 \pm 4.2) \cdot 10^{-16} \text{ m}^2$ . We attribute this deep level to the oxygen vacancy  $V_O$ , the most prominent defect state in pristine rutile crystals with reported binding energies between 750 meV and 1.18 eV,<sup>28-30</sup> in agreement with numerical simulations.<sup>36</sup>

For subsequent photocapacitance experiments, the sample was illuminated with a Thorlabs 910E LED (emission maximum at a wavelength of 910 nm at 300 K), controlled by a Keithley 3390 arbitrary waveform generator; see Fig. 2(a). Rectangular pulses with a frequency of 1 Hz were applied to the LED, switching it on and off. The LED was mounted outside the cryostat to keep it at room

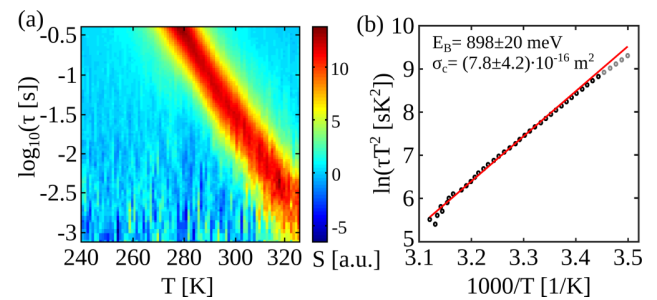


**FIG. 3.** (a) Measured time constant distribution as a function of the temperature for the conventional DLTS experiment, according to Eq. (1). (b) Arrhenius plot of the data (open circles) from (a) with the fit values for the binding energy of the deep level and its capture cross section as obtained from Eq. (2). Here, the data points represented by gray circles are excluded from the fit since at low temperatures, the DLTS data are significantly influenced by electron capture.

temperature, and the emitted light was guided by an optical fiber into the cryostat. In order to eliminate influences from the initial experimental conditions on the transients, the first four illumination cycles are excluded from the data analysis. In these experiments, the applied DC voltage was zero.

### III. EXPERIMENTAL RESULTS

Typical photocapacitance transients are represented in Fig. 2(c) for three different temperatures. Apparently, the capacitance increases under illumination and decreases toward its initial value after the light has been switched off. The saturated capacitance change  $\Delta C(T)$  and the time constants  $\tau_{\text{on/off}}(T)$  of the transients show non-monotonous evolution as the temperature  $T$  is increased. Furthermore, the time constants in response to illumination are markedly shorter than those observed after the light has been switched off.

This behavior is tentatively interpreted in terms of photoionization of deep donor levels inside the depletion region of the Schottky contact. After the photoemission of a trapped electron into the conduction band, the charge density inside the depletion region and, thus, the capacitance increases. The time constant of this process is determined by the difference between the emission and capture rates, the latter of which dominates the duration of the transient after the light has been turned off. We cross-checked this interpretation by measuring the photocapacitance under illumination with light of a wavelength larger than 1550 nm and could not detect a response. This simple picture will be substantiated by the rate equation model described below.

The photocapacitance transients have been measured in a temperature range from 185 to 340 K with a heating rate of 2 K min<sup>-1</sup>. For each temperature step, 30 individual transients were recorded and averaged. The data were processed using the lock-in weight function, Eq. (1), and are shown in Figs. 4(a) and 4(c) for the response after the light has switched on and off, respectively.

The capacitance change in response to the illumination, see Fig. 4(a), is positive, indicating electron emission from the traps. As the temperature is increased from 180 to  $\approx 280$  K,  $\tau_{\text{on}}$  decreases, while the amplitude  $S$  of the lock-in signal increases. For  $T \gtrsim 280$  K, the photocapacitance vanishes, with a cut-off time constant that decreases as  $T$  is increased, as visible in the temperature range between  $\approx 260$  and 300 K.

The transients observed after the illumination has been turned off, see Fig. 4(c), are negative and, thus, indicative of trap repopulation. The observed time constants  $\tau_{\text{off}}$  are significantly larger than  $\tau_{\text{on}}$  for all temperatures and get smaller as the temperature is increased, with a larger temperature dependence. The capacitive response is strongly suppressed around 300 K, and a sharp cutoff can be observed toward longer time constants in the interval  $270 \text{ K} \lesssim T \lesssim 320 \text{ K}$ , which coincides with the thermal emission time obtained from the conventional DLTS experiment [dashed white lines in Figs. 4(a) and 4(c)]. Furthermore, the distribution of the time constants during capture is much broader as compared to the emission scenario.

For an explanation of this behavior, note that the measured time constants and amplitudes of the transients reflect the influences of up to three simultaneous contributions, namely, electron

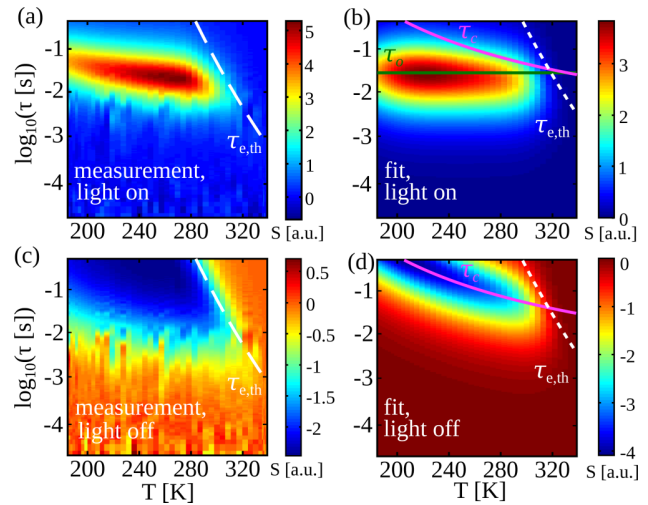


**FIG. 4.** Measured temperature dependence of the time constant distribution observed for the photocapacitance transients in response to the light being turned on (a) and off (c). The dashed white lines denote the thermal capture time as a function of  $T$ , as determined from the conventional DLTS experiment (Fig. 3). In (b) and (d), the corresponding fit results obtained from the rate equation model are represented. Here, the pink line gives the capture time as a function of  $T$ , while the horizontal green line corresponds to the optical emission time constant, and the dotted line shows the measured thermal emission time.

capture as well as thermal emission and, in the case of illumination, photoemission. In Sec. IV, we show how these influences can be disentangled and described by their characteristic quantities with the help of a rate equation model.

### IV. RATE EQUATION MODEL FOR ELECTRON EMISSION AND CAPTURE

In this section, a system of coupled rate equations is used to determine the binding energy  $E_B$  of the deep level, its optical cross section  $\sigma_o$ , as well as the optical emission rate  $e_o$ . We do not use the information obtained from the conventional DLTS measurements in this sample characterization since it is not *a priori* known that the optically active trap is identical to that one dominating the thermionic emission. It could be, for example, a level with a significantly larger binding energy inaccessible to conventional DLTS.

The optical emission rate is given by<sup>19</sup>

$$e_o = \sigma_o \Phi, \quad (3)$$

where  $\Phi$  denotes the photon flux density in the TiO<sub>2</sub>, which is not known. Therefore,  $e_o$  is determined within the model described below. The total emission rate equals the sum of both individual emission rates, following Matthiessen's rule,<sup>1</sup>

$$e = e_{th} + e_o. \quad (4)$$

To the best of our knowledge, there is no corresponding expression available for the electron capture, reflecting the fact that

the underlying physics is less clear. In the experimental results shown in Fig. 4, we observed a slight shift of the capture lifetime toward shorter values under increasing temperature. Hence, we assume a phenomenologically motivated capture rate originating from a thermally activated process, i.e., of the form

$$c = c_0 \exp(-\varepsilon_c/k_B T) \quad (5)$$

like Eq. (2), with the parameters  $\varepsilon_c$  and  $c_0$ , which can be interpreted as a characteristic energy of the electron capture and a measure of the capture rate at  $\varepsilon_c/T \rightarrow 0$ , respectively. The origin of the temperature dependence of the capture rate is presently unclear. We speculate that it may indicate that traps inside the space charge layer contribute to the capture, which requires thermal activation of the electrons to access the trap location, a process that would be properly reflected by Eq. (5). For a model calculation on the influence of different capture rates on the DLTPCS spectrum, see the [supplementary material](#).

The occupancies, i.e., the fractions of the empty and the occupied traps, are denoted as  $n_0$  and  $n_1$ , respectively. We assume that a trap can host no more than one electron and neglect any processes involving holes. Under an external, thermal, or optical excitation, the dynamics of these occupancies can be modeled by the set of rate equations

$$\dot{n}_0 = -c \cdot n_0 + e \cdot n_1, \quad (6)$$

$$\dot{n}_1 = c \cdot n_0 - e \cdot n_1. \quad (7)$$

Here, the electron source for capture is assumed to have the character of an electron reservoir. Analytic solutions for the system can be found, which read as

$$n_1 = \frac{(n_0^0 + n_1^0)e}{c + e} - \left( \frac{n_0^0 c + n_1^0 e}{c + e} \right) \exp(-t(c + e)), \quad (8)$$

where  $e$  and  $c$  are functions of the temperature, and

$$n_0 = 1 - n_1, \quad (9)$$

where  $n_0^0$  and  $n_1^0$  denote the initial occupations at  $t = 0$  s. The corresponding capacitance is proportional to the density of the filled traps, i.e.,

$$\Delta C(t) \propto n_1(t). \quad (10)$$

The parameters determining the kinetics of the system can be obtained by a least-square fit of the analytic solution to the measured data in Fig. 4, with the conditions of a constant  $e_0$  under illumination and  $e_0 = 0$  in the dark. In each iteration step, the transients for all observed temperatures are calculated. We assume that prior to the first illumination cycle, all traps are occupied; i.e.,  $n_0^0 = 0$ ,  $n_1^0 = 1$ . The lock-in signals of the resulting transients, computed according to Eq. (1) on the same time grid as in the measured data, are represented in Figs. 4(b) and 4(d). The resulting fit parameters amount to  $E_b = (928 \pm 16)$  meV and

TABLE I. Parameters obtained from the least-square fits shown in Figs. 3 and 4.

Technique	$E_b$ (meV)	$\sigma_c$ ( $10^{-16}$ m <sup>2</sup> )	$\varepsilon_c$ (meV)	$c_0$ (s <sup>-1</sup> )	$e_0$ (s <sup>-1</sup> )
DLTPCS	$928 \pm 16$	$4.4 \pm 2.6$	$125 \pm 5$	$2748 \pm 780$	$35.7 \pm 1.7$
DLTS	$898 \pm 20$	$7.8 \pm 4.2$	n.a.	n.a.	n.a.

$\sigma_c = (4.4 \pm 2.6) \times 10^{-16}$  m<sup>2</sup>. Table I compares these fit parameters to those obtained from the conventional DLTS.

These values for the binding energy and the capture cross section are, within the error bars, the same as those obtained from the conventional DLTS. This finding provides strong evidence that the deep level traps we observe in the optical experiments are the same as the ones seen in the conventional DLTS measurement. Furthermore, the optical responses are well reproduced by the fit parameters for both photoemission and capture, see the full lines in Figs. 4(b) and 4(d), which represent the fit values.

We emphasize that hereby, a technique has been demonstrated that enables the determination of the electron capture cross section of deep traps from transient photocapacitance spectroscopy in combination with a suitable rate equation model. This may be particularly useful in samples where substantial recapture during emission is present. Experimentally, recapture could be suppressed by a high reverse bias voltage. This, on the other hand, is not possible in all samples and, furthermore, provides an additional source of electrons that may get captured, namely, from the leakage current.<sup>37</sup> Therefore, having the option to include capture during emission in the model is essential. We note, furthermore, that an extension to more complicated systems with several trap species along the lines of Ref. 38 is straightforward. Since each trap has its own characteristic time constant, the presence of multiple traps would be manifested in a corresponding number of peaks in the lock-in signals, which can be attributed to the traps by an adapted rate equation model.

## V. DISCUSSION

We proceed with a discussion of the physics behind the observed phenomenology and begin with the capture process; see Figs. 4(c) and 4(d).

Below  $\approx 280$  K, the measured time constants show a broad distribution, with a mean value that decreases approximately exponentially with increasing  $T$ . This dependence is in accordance with the *ad hoc* assumption of thermally activated capture, as expressed in Eq. (5). This suggests the following capture process. After emission (either thermally or by optical excitation), the electrons in the conduction bands drift toward the Ni back electrode in the built-in electric field. Recapture into a trap located at a certain position requires kinetic energy, which allows the electron to reach again this uphill location. The characteristic energy  $\varepsilon_c$  introduced in Eq. (5) is, therefore, a measure for the energy difference between the conduction band edge at the trap location and the flat-band region, which equals the quasi-Fermi level at the back contact. It represents possibly a non-trivial average of a form to be determined in future work. Within this picture, the broad distribution of capture times reflects the capture in a certain interval of the space



charge region, starting from the onset of the depletion region and extending toward the rNM electrode, where  $E_b$  is referred to the local, varying conduction band bottom. Relating  $\varepsilon_c$  to the conduction band profile, we can estimate that the electrons are captured within an interval  $\Delta z \approx 5$  nm from the onset of the depletion region. Due to the stronger temperature dependence of the thermal emission rate in comparison with the capture rate, the two rates cross each other as  $T$  is increased. For  $\tau_c \gg \tau_{e,th}$ , the traps are essentially empty and  $\Delta C$  vanishes. Thus,  $\tau_{e,th}(T)$  represents a transition line above which  $\Delta C$  is suppressed.

With this interpretation at hand, we move on to a discussion of the photocapacitance transients measured in response to illumination; see Figs. 4(a) and 4(b). Below  $\approx 280$  K, the measured time constant of the transients decreases approximately exponentially with increasing  $T$ , while its amplitude increases. Since the optical emission rate should, to a first approximation, be temperature independent, one is tempted to attribute this decrease to a thermal contribution, according to Eq. (3). Note, however, that  $\tau_{e,th} \gg \tau_{e,o}$  in this temperature range. Heating of the sample by the light is an unlikely explanation, considering that  $T$  should increase by as much as  $\approx 100$  K. Also, we exclude enhanced emission via tunneling after photon absorption since the photon energy (1.37 eV) is significantly larger than  $E_b$ . Whether the optical cross section or the intensity of the light coupled into the junction via the rNM gate, do have a temperature dependence, is an open issue to be addressed in future studies. Likewise, the technique can be readily extended to determine the temperature dependence of the optical cross section<sup>19,39</sup> as well as Franck-Condon shifts by frequency-dependent photocapacitance measurements.<sup>39,40</sup> As soon as the thermal emission rate becomes the dominant term at larger temperatures, however, the photocapacitance gets suppressed because the photons meet essentially empty traps. Furthermore, both emission processes are expected to show no pronounced dependence on the trap location. This explains why the emission time constants show a much sharper distribution than the capture time, which reflects the distribution of the traps in the accessible energy interval of the space charge region. Finally, we comment on the increase of the emission amplitude with increasing  $T$ . It has its origin in the decreasing capture time as  $T$  increases. Hence, photons find more traps occupied, and a larger transient amplitude emerges.

## VI. CONCLUSION

It has been demonstrated how the capture cross section of a deep trap can be determined by deep level optical spectroscopy, which works also for traps deep inside the bandgap and, thus, inaccessible by transport spectroscopy. This was exemplified on the well-known oxygen vacancy in rutile, which is deep enough for optical spectroscopy and at the same time still accessible by conventional DLTS. Using a Schottky contact formed by a rolled-up nanomembrane allowed us to couple the light with sufficiently high intensity into the space charge region of the corresponding Schottky barrier. The conventional DLTS and the DLTPCS methods in combination with a suitable rate equation model gave identical quantitative results within the error bars. Furthermore, the combination of these methods allows an unprecedented interpretation of the measured time constants and their temperature

dependence. In particular, the measurements contain information regarding the capture process, for which an *ad hoc* model has been developed. Further work may comprise the application of DLTPCS to deep traps, which are inaccessible for pure transport techniques, the simultaneous determination of the optical cross section, and the Franck-Condon shift by looking at the photocapacitance as a function of the light energy,<sup>40</sup> depth-resolved measurements,<sup>41</sup> or determination of the dependence of the capture cross section on the applied electric field.

## SUPPLEMENTARY MATERIAL

The preparation of the rolled-up nanomembrane electrode is described in more detail in the [supplementary material](#). Furthermore, a schematic illustration of the electron capture and emission processes is given, and the influence of the frequency dependence of the transient capacitance on the analysis is discussed.

## AUTHOR DECLARATIONS

### Conflict of Interest

The authors have no conflicts to disclose.

## Author Contributions

**L. Berg:** Data curation (equal); Investigation (lead); Visualization (equal); Writing – original draft (supporting); Writing – review & editing (supporting). **L. Schnorr:** Data curation (equal); Software (lead); Writing – original draft (supporting). **L. Mercès:** Investigation (equal); Methodology (equal). **J. Bettini:** Investigation (equal); Resources (supporting). **C. C. Bof Bufon:** Conceptualization (equal); Project administration (equal); Resources (equal); Writing – original draft (supporting). **T. Heinzl:** Conceptualization (equal); Funding acquisition (equal); Project administration (lead); Resources (equal); Supervision (equal); Validation (equal); Writing – original draft (lead).

## DATA AVAILABILITY

The data that support the findings of this study are available from the corresponding author upon reasonable request.

## REFERENCES

- 1D. V. Lang, *J. Appl. Phys.* **45**, 3023–3032 (1974).
- 2C. Hurtes, M. Boulou, A. Mitonneau, and D. Bois, *Appl. Phys. Lett.* **32**, 821–823 (1978).
- 3S. Pantelides, *Rev. Mod. Phys.* **50**, 797–858 (1978).
- 4K. Yamasaki, M. Yoshida, and T. Sugano, *Jpn. J. Appl. Phys.* **18**, 113–122 (1979).
- 5B. Clerjaud, *J. Phys. C: Solid State Phys.* **18**, 3615–3661 (1985).
- 6D. Pons and J. Bourgoïn, *J. Phys. C: Solid State Phys.* **18**, 3839–3871 (1985).
- 7S. Pearton, J. Corbett, and T. Shi, *Appl. Phys. A* **43**, 153–195 (1987).
- 8S. Weiss and R. Kassing, *Solid-State Electron.* **31**, 1733–1742 (1988).
- 9T. Dalibor, G. Pensl, H. Matsunami, T. Kimoto, W. Choyke, A. Schoner, and N. Nordell, *Phys. Status Solidi A* **162**, 199–225 (1997).
- 10L. Storasta, J. Bergman, E. Janzen, A. Henry, and J. Lu, *J. Appl. Phys.* **96**, 4909–4915 (2004).

- <sup>11</sup>S. W. Lin, A. M. Song, M. Missous, I. D. Hawkins, B. Hamilton, O. Engström, and A. R. Peaker, *Mater. Sci. Eng. C* **26**, 760 (2006).
- <sup>12</sup>M. Meneghini, C. De Santi, I. Abid, M. Buffolo, M. Cioni, R. A. Khadar, L. Nela, N. Zagni, A. Chini, F. Medjdoub, G. Meneghesso, G. Verzellesi, E. Zanoni, and E. Matioli, *J. Appl. Phys.* **130**, 181101 (2021).
- <sup>13</sup>M. Sahu, V. R. M. Reddy, C. Park, and P. Sharma, *Sol. Energy* **230**, 13–58 (2021).
- <sup>14</sup>L. Schnorr, O. Khoukhi, L. Berg, T. Heinzl, C. Rothfuchs-Engels, S. Scholz, A. Ludwig, and A. D. Wieck, *Phys. Rev. B* **104**, 205310 (2021).
- <sup>15</sup>S. DasGupta, O. Slobodyan, T. Smith, A. Binder, J. Flicker, R. Kaplar, J. Mueller, L. Garcia Rodriguez, and S. Atcity, *Appl. Phys. Lett.* **120**, 053502 (2022).
- <sup>16</sup>B. Marquardt, M. Geller, A. Lorke, D. Reuter, and A. D. Wieck, *Appl. Phys. Lett.* **95**, 022113 (2009).
- <sup>17</sup>M. Geller, B. Marquardt, A. Lorke, D. Reuter, and A. D. Wieck, *Nanoscale Res. Lett.* **5**, 829 (2010).
- <sup>18</sup>L. Dobaczewski, P. Kaczor, I. D. Hawkins, and A. R. Peaker, *J. Appl. Phys.* **76**, 194–198 (1994).
- <sup>19</sup>A. Chantre, G. Vincent, and D. Bois, *Phys. Rev. B* **23**, 5335 (1981).
- <sup>20</sup>R. Zeisel, C. Nebel, M. Stutzmann, E. Gheeraert, and A. Deneuve, *Phys. Rev. B* **60**, 2476–2479 (1999).
- <sup>21</sup>O. Maida, D. Kanemoto, and T. Hirose, *Thin Solid Films* **741**, 139026 (2022).
- <sup>22</sup>G. L. Miller, D. V. Lang, and L. C. Kimerling, *Annu. Rev. Mater. Sci.* **7**, 377–448 (1977).
- <sup>23</sup>D. S. Day, M. Y. Tsai, and B. G. Streetman, *J. Appl. Phys.* **50**, 5093 (1979).
- <sup>24</sup>C. Bufon, J. C. Gonzalez, D. J. Thurmer, D. Grimm, M. Bauer, and O. G. Schmidt, *Nano Lett.* **10**, 2506 (2010).
- <sup>25</sup>L. Merces, G. Candiottio, L. M. M. Ferro, A. de Barros, C. Vinicius, S. Batista, A. Nawaz, A. Riul, Jr., R. B. Capaz, and C. C. B. Bufon, *Small* **17**, 2103897 (2021).
- <sup>26</sup>C. V. S. Batista, L. Merces, C. A. R. Costa, D. H. S. de Camargo, and C. C. B. Bufon, *Adv. Funct. Mater.* **32**, 2108478 (2022).
- <sup>27</sup>G. L. Pozzoli, L. Merces, E. Yassitepe, V. B. de Moraes, D. H. S. de Camargo, and C. C. B. Bufon, *ACS Appl. Nano Mater.* **3**, 3060 (2020).
- <sup>28</sup>D. C. Cronemeyer, *Phys. Rev.* **113**, 1222 (1959).
- <sup>29</sup>I. Nakamura, N. Negishi, S. Kutsuna, T. Ihara, S. Sugihara, and E. Takeuchi, *J. Mol. Catal. A* **161**, 205–212 (2000).
- <sup>30</sup>X. Pan, M.-Q. Yang, X. Fu, N. Zhang, and Y.-J. Xu, *Nanoscale* **5**, 3601–3614 (2013).
- <sup>31</sup>L. Merces, R. F. de Oliveira, and C. C. B. Bufon, *ACS Appl. Mater. Interfaces* **10**, 39168 (2018).
- <sup>32</sup>Y. Chen, L. Ma, and O. G. Schmidt, *Adv. Opt. Mater.* **9**, 2100143 (2021).
- <sup>33</sup>M. Zhong, H. Shima, and H. Akinaga, *Appl. Phys. Lett.* **96**, 042107 (2010).
- <sup>34</sup>D. B. Strukov, G. S. Snider, D. R. Stewart, and R. S. Williams, *Nature* **453**, 80 (2008).
- <sup>35</sup>H. Frederikse, *J. Appl. Phys.* **32**, 2211 (1961).
- <sup>36</sup>G. Mattioli, F. Filippone, P. Alippi, and A. A. Bonapasta, *Phys. Rev. B* **78**, 241201 (2008).
- <sup>37</sup>M. C. Chen, D. V. Lang, W. F. Dautremont-Smith, A. M. Sergent, and J. P. Harbison, *Appl. Phys. Lett.* **44**, 790 (1984).
- <sup>38</sup>L. Schnorr, J. Labes, L. Kurten, T. Heinzl, C. Rothfuchs-Engels, S. Scholz, A. Ludwig, and A. D. Wieck, *Phys. Rev. B* **104**, 035303 (2021).
- <sup>39</sup>M. Jaros, *Phys. Rev. B* **16**, 3694 (1977).
- <sup>40</sup>L. Lugani, M. A. Py, J.-F. Carlin, and N. Grandjean, *Appl. Phys. Lett.* **109**, 152012 (2016).
- <sup>41</sup>A. Hierro, D. Kwon, S. A. Ringel, S. Rubini, E. Pelucchi, and A. Franciosi, *J. Appl. Phys.* **87**, 730 (2000).

# Transient photocapacitance spectroscopy on Au/TiO<sub>2</sub> Schottky diodes with rolled-up nanomembrane electrodes

L. Berg, L. Schnorr, and T. Heinzel\*

*Solid State Physics Laboratory, Heinrich-Heine-Universität Düsseldorf, 40204 Düsseldorf, Germany*

L. Mercés

*Material Systems for Nanoelectronics, Chemnitz University of Technology, 09107 Chemnitz, Germany and  
"Gleb Wataghin" Institute of Physics, University of Campinas, 13083-859 Campinas-SP, Brazil*

J. Bettini

*Brazilian Nanotechnology National Laboratory, Brazilian Center for Research in Energy and Materials, 13083-100 Campinas-SP, Brazil*

C. C. Bof Bufon

*Mackenzie Presbyterian Institute, Mackenzie Institute for Research in Graphene  
and Nanotechnologies – MackGraphe, 01302-907, São Paulo/SP, Brazil*

(\*thomas.heinzel@hhu.de)

(Dated: January 23, 2023)

## I. I. VERTICAL-JUNCTION STACKING AND MORPHOLOGY

To verify the thickness  $t$  of the TiO<sub>2</sub> thin films employed as functional layer in our vertical devices, we employed FIB to prepare a lamella sample and image the bottom-electrode/TiO<sub>2</sub>-film stacking. Figure 1 (d) in the main text reproduces the cross-sectional TEM image of the Cr/Ni/TiO<sub>2</sub> structure, allowing us to measure  $t = (53 \pm 2)$  nm. The thor-

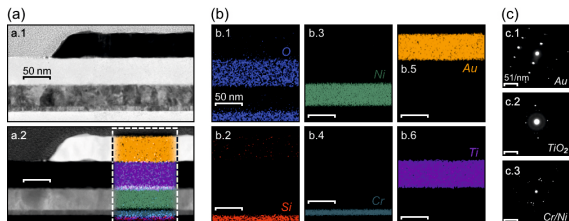


FIG. 1. Vertical junction morphology obtained through TEM. (a) Electron microscopy images of a lamella sample composed of an SiO<sub>2</sub> substrate and the Cr/Ni/TiO<sub>2</sub>/Au thin films: (a.1) TEM image, and (a.2) ADF-STEM image. Inside the dashed-line rectangle in (a.2) is the superposition of all EDS data. (b) EDS map of lamella sample: (b.1) O, (b.2) Si, (b.3) Ni, (b.4) Cr, (b.5) Au, and (b.6) Ti. (c) Diffraction images obtained from: (c.1) patterned Au-film thermally-evaporated on the TiO<sub>2</sub>, (c.2) TiO<sub>2</sub> film grown by ALD on the Cr/Ni, and (c.3) Cr/Ni film thermally evaporated on the SiO<sub>2</sub> substrate.

ough morphology evaluation of the lamella sample using TEM is exhibited in Figure 1. Figure 1 (a) shows TEM and ADF-STEM images that visualize all device layers. The image dissimilarity, when comparing Figure 1 (a.1) and Figure 1 (a.2), corresponds approximately to mass and diffraction contrasts. For example, notice that the top electrode (trapezoidal Au layer) displays the highest contrast difference, i.e., black in the TEM image and white in the ADF-STEM one. Inside

the dashed-line rectangle of Figure 1 (a.2) is the superposition of all EDS data. Single EDS maps are displayed in Figure 1 (b). The EDS maps show clear atomic layers, which can be associated either with the device interfaces or a few elements diffusion through the layers. Considering the diffraction images shown in Figure 1 (c), all device counterparts display polycrystalline arrangements. The Au top-electrode diffraction image in Figure 1 (c.1) shows strong spots, which can be correlated with polycrystalline grains displaying a ca. 100 nm size. The TiO<sub>2</sub> film diffraction image shows weak diffraction spots and some halos, which are associated with a poor single-crystalline arrangement. Finally, the Cr/Ni bottom-electrode film shows a clear polycrystalline pattern ascribed to many strong spots, which can be correlated with ca. 30 nm size grains.

## II. II. ELECTRON CAPTURE

In Figure 2, the capture and emission processes of relevance for the capacitance transients are illustrated.

## III. III. FREQUENCY DEPENDENCE OF THE CAPACITANCE

As mentioned in the main text, a modulation frequency for the capacitance measurement of  $f = 28$  MHz was chosen in order to obtain an acceptable noise level. Since the dielectric relaxation occurs at much lower frequencies (i.e., in our sample in the sub-MHz regime), the extracted values for the capacitance, and hence for the doping density as well, are not reliable. We emphasize that these values are irrelevant for our analysis. Nevertheless, the magnitude of these deviations has been estimated by measurements at much lower frequencies, namely at  $f = 1.5$  kHz, see Figure 3. These studies indicate that by our large frequency, the capacitance is underestimated by a factor of about 1.6, (Figure 3a), while the actual dop-

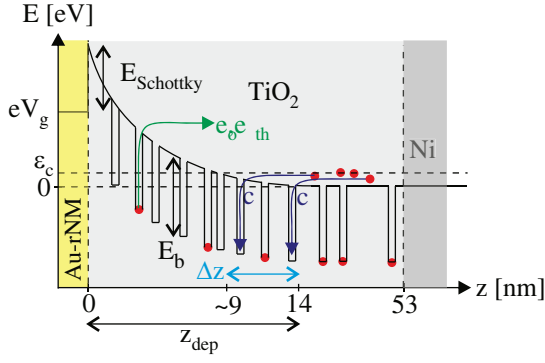


FIG. 2. Schematic illustration of the capture and emission processes. Electrons (red circles) are thermally or optically emitted from the deep levels (green arrow) and captured predominantly from the flat band region where they drift to after their emission (blue arrows). Capture occurs within  $\Delta z \approx 5$  nm from the edge of the space charge region at  $z_{dep} = 14$  nm, corresponding to a conduction band energy difference of roughly  $\varepsilon_c = 125$  meV. The black line denotes the conduction band edge and the deep level potentials.

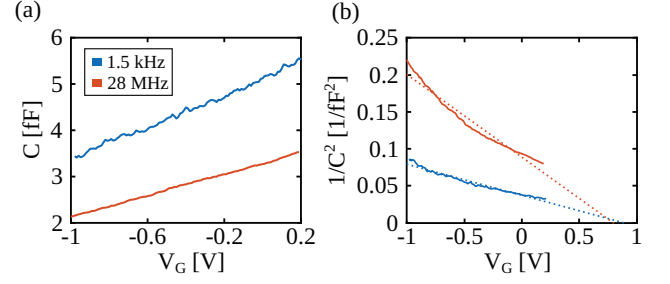


FIG. 3. Capacitance-voltage measurements (a) and the corresponding Mott-Schottky plots (b) for the data taken at  $f = 1.5$  kHz (blue lines) and at  $f = 28$  MHz (red lines). The dashed lines in (b) depict the linear fits, leading carrier densities of  $4.2 \times 10^{19} \text{ cm}^{-3}$  and  $1.6 \times 10^{19} \text{ cm}^{-3}$ , respectively. Schottky Barrier heights of 0.89 eV and of 0.79 eV are obtained.

ing density is larger by a factor of  $\approx 2.56$ , (Figure 3b). We note that the linearity, but also the signal-to-noise ratio, of the Mott-Schottky plot for the data taken at larger frequency is reduced. However, the values obtained for the Schottky barrier height from the condition  $1/C^2(V_G) = 0$  differ by approximately 10% on.

#### IV. MODEL CALCULATION FOR A SYSTEM WITH TWO TRAP ENERGIES

In case the time constants of the traps differ by more than the temporal resolution of the DLTS setup or the intrinsic width of the time constant distribution of the individual states, multiple traps could be detected by DLTCPS. This situation generates multiple peaks in the lifetime distribution of the traps, as exemplified for model parameters in Fig. 4).



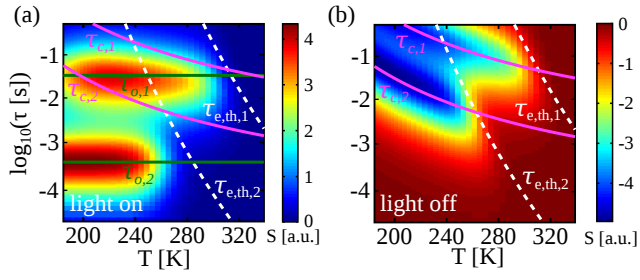


FIG. 4. Model calculation for a life time distribution measurement on a sample with two well-separated trap energies. The parameters used are: binding energies  $E_{b,1} = 928 \text{ meV}$ ,  $E_{b,2} = 724 \text{ meV}$ , with a capture cross section of  $\sigma = 7.65 \times 10^{-16} \text{ m}^2$ . The parameters  $e_0$  and  $c_0$  are set to  $5.4 \times 10^{-4} \text{ s}^{-1}$  and  $3 \times 10^3 \text{ s}^{-1}$ , respectively. The capture rates are assumed to obey eq. 5 in the main text. Two well-separated emission and capture peaks can be seen after the light has been turned on (a) or off (b). All symbols and the color scale agree with those in the main text.



---

# Chapter 7

## Conclusion and outlook

Within this thesis three projects on the occupation dynamics of self-assembled quantum dots and deep level traps have been conducted. The main findings are summarised and an outlook for potential future research projects is given here.

Starting point was the capture dynamics of electrons into a single layer of SAQDs that is far from its reservoir ( $> 100$  nm). Experiments were performed to isolate the capture rate from the capacitance transients, as a function of the applied bias voltage, the temperature and the magnetic field. The back contact was identified as the main dominant electron source. A model was established describing the capture mechanism to be dominated by diffusion and the electrostatic properties of the partially filled SAQDs. A tunneling mechanism was identified for suitable conditions with sufficiently low diffusion current, achievable by low temperatures or partially filled SAQDs. Furthermore, the capture and emission rates were used to set up a model describing the hysteretic capacitance-voltage curves of such structures.

As the diffusion current resembles a thermally activated process, it is possible to investigate the tunnelling contribution in more detail at lower temperatures. In the presented experiments the magnetic field was always applied perpendicular to the SAQDs layer, modifying the dots' energetic levels. However, the resolution was not sufficient to resolve the different energetic levels. High resolution Laplace DLTS [107] may be a tool to overcome this problem. Probing of the capture dynamics under different experimental conditions such as a magnetic field, applied in parallel to the SAQDs layer or illumination of the sample, could potentially reveal additional capture mechanisms.

The occupation dynamics of two layers of SAQDs at a distance of 200 nm, embedded in a Schottky junction, were investigated. The experiments were carried out at a temperature of 77 K, the rates were determined as a function of the bias voltage. An interdependence of each layers capture and emission rates on the other layers' occupation was found. This is due to the electric field generated by the electrons in each layer. The behavior was further modeled using a set of rate equations.

A promising outlook to future work is the utilisation of the electrostatic coupling. Many optoelectronic devices contain multiple layers of SAQDs, with similar layer

---

distances, the presented electrostatic interdependence could improve the efficiency of these devices. The interaction can further be studied at different temperature regimes, e.g. at lower temperatures where tunneling dominates the capture or emission. For a more detailed understanding, the occupation dynamics of a sample containing only the Top layer needs to be investigated. Optimising the interdependence with appropriate choices of distances and SAQD densities remains a task for the future.

Based on temperature dependent phot capacitance transients the deep level transient phot capacitance spectroscopy was developed. The oxygen vacancy of rutile  $\text{TiO}_2$  acted as a platform for the development. This method extracts the parameters of binding energy, capture cross section and optical emission rate from the transients with the help of a rate equation model. A rolled up nanomembrane allowed for a high illumination rate.

Future experiments could extend the developed method to account also for the Franck-Condon energy, by varying the photon energies. This approach could potentially also explain the observed temperature dependence of the optical emission rate, which was left unexplained in *Paper IV*. Furthermore,  $\text{TiO}_2$  is often used in the field of gas sensing. Two advantages of the rNM can be exploited here: First, the low area coverage of the rNM makes the  $\text{TiO}_2$  accessible to the gas, and second, the rNM with its dimensions can be used to locally heat up the substrate. Since it has two connections it can be heated with a current in order to enhance the reaction of the substrate with the surrounding gas, potentially leading to more sensitive and faster gas sensors.

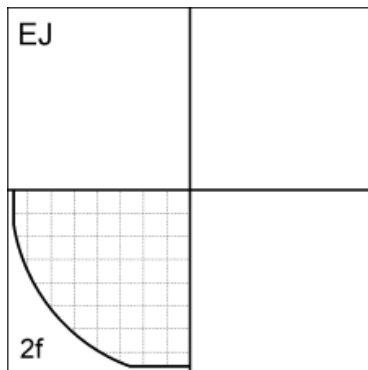
---

---

---

# Appendix A

## Growth protocol for sample #14691



Sample: **14691**  
 Material: GaAs  
 Orientation: (100)  
 Wafer: WV/23678/Un61  
 Rotation: 4  
 Pressure (Torr):  $4.2 \times 10^{-8}$   
 Date: 27.08.2015  
 File: 14691.csv

		300K	77K	4.2K	1K
dark	[cm <sup>2</sup> / Vs]				
	n [cm <sup>-2</sup> ]				
illum	[cm <sup>2</sup> / Vs]				
	n [cm <sup>-2</sup> ]				

Layer	Loop	T [°C]	Dur. [s]	Thickn. [nm]	Cells (°C)
GaAs		613.0	501.0	100	As-LF 357 °C
AlAs	Start: 20x	613.0	26.5	2.6	As-UF 700 °C
GaAs	End	613.0	13.0	2.6	Si(max) 1310 °C
GaAs		613.0	250.5	50	In-LF 725 °C
GaAs:Si		613.0	1503.0	2E18 cm <sup>-2</sup> -2300	In-UF 755 °C
GaAs:Si		613.0	2505.0	2E16 cm <sup>-2</sup> -2500	Ga-LF 1002 °C
GaAs		587.0	25.1	5	Ga-UF 850 °C
GaAs		613.0	25.1	5	Al 1177.5 °C
InAs	Do: 15x	530.0	4.0	0	
GaAs		505.0	40.1	8	
GaAs		525.0	25.1	5	
GaAs:Si		613.0	2004.0	2E16 cm <sup>-2</sup> -2400	
					<i>Comment</i>
					Quantum Dots
					DLTS
					Platen: -
					T(pyro) = 600°C
					As: 57,5%
					pF: 9.6e-8 Torr
					Tp = 498°C
					(Grown by S. Scholz)

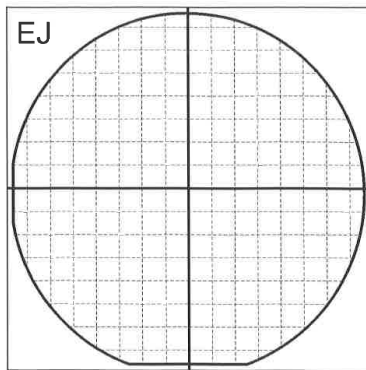


---

---

# Appendix B

## Growth protocol for sample #15070



Sample: **15070**  
 Material: GaAs  
 Orientation: (100)  
 Wafer: WV24428/Un14  
 Rotation: 4  
 Pressure (Torr):  $4.6 \times 10^{-8}$   
 Date: 30.01.2019  
 Hall Sample: N/A

		300K	77K	4.2K	1K
dark	$\mu$ [cm <sup>2</sup> / Vs]				
	n [cm <sup>-2</sup> ]				
illum	$\mu$ [cm <sup>2</sup> / Vs]				
	n [cm <sup>-2</sup> ]				

Layer	Loop	T [°C]	Dur. [s]	Thickn. [nm]	Cells (°C)
GaAs		654.0	501.8	100	As-LF 368 °C
AlAs	Start: 20x	654.0	25.9	2.6	As-UF 700 °C
GaAs	End	654.0	13.0	2.6	Si(max) 1290 °C
GaAs		654.0	250.9	50	In-LF 713 °C
Si-delta		654.0	128.0	0	In-UF 743 °C
GaAs:Si		654.0	5.0	1	Ga-LF 1002 °C
Si-delta		654.0	13.0	0	Ga-UF 850 °C
GaAs:Si		654.0	5.0	1	Al 1166 °C
Si-delta		654.0	3.0	0	
Si-delta		654.0	6.0	0	
GaAs:Si		654.0	5.0	1	
GaAs:Si		654.0	1475.2	294	<i>Comment</i>
GaAs		654.0	60.2	12	DTLS
GaAs:Si		654.0	2458.6	490	T(pyro) = 570°C
GaAs:Si		654.0	5.0	1	As = 73%
GaAs		629.0	25.1	5	pF = 9.6e-6 Torr
GaAs		654.0	25.1	5	1st QDs:
InAs	Do: 15x	572.0	4.0	0.1	15 cycles full rotation
GaAs		547.0	40.2	8	Tp(start) = 488°C
GaAs		562.0	15.1	3	Tp(end) = 480°C
Si-delta		592.0	30.0	0	2nd QDs:
GaAs:Si		654.0	60.2	12	15 cycles full rotation
GaAs:Si		654.0	837.9	167	Tp(start) = 486°C
GaAs		654.0	5.0	1	Tp(end) = 490°C

(Grown by N. Bart)





**Sample: 15070**

<i>Layer</i>	<i>Loop</i>	<i>T [°C]</i>	<i>Dur. [s]</i>	<i>Thickn. [nm]</i>
GaAs		629.0	25.1	5
GaAs		654.0	25.1	5
InAs	Do: 15x	572.0	4.0	0.1
GaAs		547.0	40.1	8
GaAs		562.0	15.1	3
Si-delta		592.0	30.0	0
GaAs:Si		654.0	60.2	12
GaAs:Si		654.0	1038.6	207
GaAs		654.0	5.0	1





---

# Bibliography

- [1] D. Leonard et al. “Direct formation of quantum-sized dots from uniform coherent islands of InGaAs on GaAs surfaces”. In: *Applied Physics Letters* **63.23** (1993), pp. 3203–3205.
  - [2] D. Bimberg, M. Grundmann, and N. N. Ledentsov. *Quantum dot heterostructures*. John Wiley & Sons, 1999.
  - [3] L. P. Kouwenhoven, D. Austing, and S. Tarucha. “Few-electron quantum dots”. In: *Reports on progress in physics* **64.6** (2001), p. 701.
  - [4] M. Grundmann, O. Stier, and D. Bimberg. “InAs/GaAs pyramidal quantum dots: Strain distribution, optical phonons, and electronic structure”. In: *Physical Review B* **52.16** (1995), p. 11969.
  - [5] R. J. Warburton et al. “Coulomb interactions in small charge-tunable quantum dots: A simple model”. In: *Physical Review B* **58.24** (1998), p. 16221.
  - [6] J. Nilsson et al. “Quantum teleportation using a light-emitting diode”. In: *Nature Photonics* **7.4** (2013), pp. 311–315.
  - [7] P. Michler et al. “A quantum dot single-photon turnstile device”. In: *science* **290.5500** (2000), pp. 2282–2285.
  - [8] I. L. Krestnikov et al. “1.3  $\mu\text{m}$  resonant-cavity InGaAs/GaAs quantum dot light-emitting devices”. In: *Semiconductor science and technology* **16.10** (2001), p. 844.
  - [9] N. Kirstaedter et al. “Low threshold, large To injection laser emission from (InGa) As quantum dots”. In: *Electronics Letters* **30.17** (1994), pp. 1416–1417.
  - [10] C. L. Salter et al. “An entangled-light-emitting diode”. In: *Nature* **465.7298** (2010), pp. 594–597.
  - [11] P. Lodahl, A. Ludwig, and R. J. Warburton. “A deterministic source of single photons”. In: *Physics Today* **75.3** (2022), pp. 44–50.
  - [12] Z. Lv et al. “Semiconductor quantum dots for memories and neuromorphic computing systems”. In: *Chemical reviews* **120.9** (2020), pp. 3941–4006.
  - [13] L. Schnorr et al. “Hysteretic capacitance-voltage characteristics of self-assembled quantum dots far from equilibrium with their environment”. In: *Physical Review B* **104.20** (2021), p. 205310.
-

- 
- [14] A. Marent et al. “The QD-Flash: a quantum dot-based memory device”. In: *Semiconductor Science and Technology* **26.1** (2010), p. 014026.
- [15] P. Maier et al. “Electro-photo-sensitive memristor for neuromorphic and arithmetic computing”. In: *Physical Review Applied* **5.5** (2016), p. 054011.
- [16] M. Kroutvar et al. “Optically programmable electron spin memory using semiconductor quantum dots”. In: *Nature* **432.7013** (2004), pp. 81–84.
- [17] L. Trifunovic et al. “Long-distance spin-spin coupling via floating gates”. In: *Physical Review X* **2.1** (2012), p. 011006.
- [18] O. Gywat, G. Burkard, and D. Loss. “Biexcitons in coupled quantum dots as a source of entangled photons”. In: *Physical Review B* **65.20** (2002), p. 205329.
- [19] A. Kurzman et al. “Electron dynamics in transport and optical measurements of self-assembled quantum dots”. In: *physica status solidi (b)* **254.3** (2017), p. 1600625.
- [20] B. Ohnesorge et al. “Rapid carrier relaxation in self-assembled  $\text{In}_x\text{Ga}_{1-x}\text{As}/\text{GaAs}$  quantum dots”. In: *Physical Review B* **54.16** (1996), p. 11532.
- [21] B. Marquardt et al. “Using a two-dimensional electron gas to study nonequilibrium tunneling dynamics and charge storage in self-assembled quantum dots”. In: *Applied physics letters* **95.2** (2009).
- [22] B. Marquardt et al. “Transport spectroscopy of non-equilibrium many-particle spin states in self-assembled quantum dots”. In: *Nature Communications* **2.1** (2011), p. 209.
- [23] R. J. Luyken et al. “The dynamics of tunneling into self-assembled InAs dots”. In: *Applied Physics Letters* **74.17** (1999), pp. 2486–2488.
- [24] H. Drexler et al. “Spectroscopy of quantum levels in charge-tunable InGaAs quantum dots”. In: *Physical review letters* **73.16** (1994), p. 2252.
- [25] O. S. Wibbelhoff et al. “Magnetocapacitance probing of the many-particle states in InAs dots”. In: *Applied Physics Letters* **86.9** (2005).
- [26] D. V. Lang. “Deep-level transient spectroscopy: A new method to characterize traps in semiconductors”. In: *Journal of applied physics* **45.7** (1974), pp. 3023–3032.
- [27] S. Ghosh et al. “Conduction band offset in InAs/GaAs self-organized quantum dots measured by deep level transient spectroscopy”. In: *Applied Physics Letters* **76.18** (2000), p. 2571.
- [28] V. V. Ilchenko et al. “Deep level transient spectroscopy characterization of InAs self-assembled quantum dots”. In: *Journal of Applied Physics* **89.2** (2001), pp. 1172–1174.
- [29] S. Anand et al. “Deep level transient spectroscopy of InP quantum dots”. In: *Applied physics letters* **67.20** (1995), pp. 3016–3018.
- [30] C. M. A. Kapteyn et al. “Electron escape from InAs quantum dots”. In: *Physical Review B* **60.20** (1999), p. 14265.
-

- 
- [31] S. W. Lin et al. “Coexistence of deep levels with optically active InAs quantum dots”. In: *Physical Review B—Condensed Matter and Materials Physics* **72.16** (2005), p. 165302.
- [32] S. Schulz et al. “Tunneling emission from self-assembled InAs quantum dots probed with capacitance transients”. In: *Physical Review B* **74.3** (2006), p. 033311.
- [33] M. Geller et al. “Tunneling emission from self-organized In(Ga)As/GaAs quantum dots observed via time-resolved capacitance measurements”. In: *Physical Review B* **73.20** (2006), p. 205331.
- [34] O. Engström et al. “Electron tunneling from quantum dots characterized by deep level transient spectroscopy”. In: *Applied Physics Letters* **91.13** (2007).
- [35] A. Schramm et al. “Electron emission from self-assembled quantum dots in strong magnetic fields”. In: *Applied physics letters* **88.21** (2006).
- [36] A. Schramm et al. “Suppression of competing tunneling processes in thermally-activated carrier emission on self-assembled InAs quantum dots”. In: *Physical Review B* **77.15** (2008), p. 153308.
- [37] A. Schramm et al. “Thermionic tunneling through Coulomb barriers in charged self-assembled quantum dots”. In: *Physical Review B* **80.15** (2009), p. 155316.
- [38] L. Berg et al. “Electron capture dynamics into self-assembled quantum dots far from equilibrium with their environment”. In: *Physical Review B* **109.23** (2024), p. 235433.
- [39] L. Berg et al. “Transient photocapacitance spectroscopy on Au/TiO<sub>2</sub> Schottky diodes with rolled-up nanomembrane electrodes”. In: *Journal of Applied Physics* **133.6** (2023).
- [40] V. M. Ustinov et al. “InAs/InGaAs quantum dot structures on GaAs substrates emitting at 1.3  $\mu\text{m}$ ”. In: *Applied physics letters* **74.19** (1999), pp. 2815–2817.
- [41] T. Nowozin et al. “Temperature and electric field dependence of the carrier emission processes in a quantum dot-based memory structure”. In: *Applied Physics Letters* **94.4** (2009).
- [42] A. Beckel et al. “Time-resolved transconductance spectroscopy on self-assembled quantum dots: Spectral evolution from single-into many-particle states”. In: *Physical Review B* **89.15** (2014), p. 155430.
- [43] C. Walther et al. “Non-exponential capture of electrons in GaAs with embedded InAs quantum dots”. In: *Physica B: Condensed Matter* **273** (1999), pp. 971–975.
- [44] Y. I. Mazur et al. “Tunneling-barrier controlled excitation transfer in hybrid quantum dot-quantum well nanostructures”. In: *Journal of Applied Physics* **108.7** (2010).
- [45] P. Miska et al. “Carrier relaxation dynamics in InAs/InP quantum dots”. In: *Applied Physics Letters* **92.19** (2008).
-

- 
- [46] S. Raymond et al. “State filling and time-resolved photoluminescence of excited states in  $\text{In}_x\text{Ga}_{1-x}\text{As}/\text{GaAs}$  self-assembled quantum dots”. In: *Physical Review B* **54.16** (1996), p. 11548.
- [47] L. Schnorr et al. “Electron capture and emission dynamics of self-assembled quantum dots far from equilibrium with the environment”. In: *Physical Review B* **104.3** (2021), p. 035303.
- [48] K. Koike et al. “Room-temperature operation of a memory-effect  $\text{AlGaAs}/\text{GaAs}$  heterojunction field-effect transistor with self-assembled  $\text{InAs}$  nanodots”. In: *Applied Physics Letters* **76.11** (2000), pp. 1464–1466.
- [49] M. Geller et al. “A write time of 6 ns for quantum dot-based memory structures”. In: *Applied physics letters* **92.9** (2008).
- [50] E. S. Kannan, G. Kim, and D. A. Ritchie. “Memory characteristics of  $\text{InAs}$  quantum dots embedded in  $\text{GaAs}$  quantum well”. In: *Applied Physics Letters* **95.14** (2009).
- [51] C. R. Müller et al. “Room temperature memory operation of a single  $\text{InAs}$  quantum dot layer in a  $\text{GaAs}/\text{AlGaAs}$  heterostructure”. In: *Applied Physics Letters* **93.6** (2008).
- [52] D. Nataraj et al. “Fabrication of one-dimensional  $\text{GaAs}$  channel-coupled  $\text{InAs}$  quantum dot memory device by selective-area metal-organic vapor phase epitaxy”. In: *Applied Physics Letters* **87.19** (2005).
- [53] Y. K. Su et al. “ $\text{InGaN}/\text{GaN}$  blue light-emitting diodes with self-assembled quantum dots”. In: *Semiconductor science and technology* **19.3** (2003), p. 389.
- [54] Q. Li et al. “Development of modulation p-doped 1310 nm  $\text{InAs}/\text{GaAs}$  quantum dot laser materials and ultrashort cavity Fabry–Perot and distributed-feedback laser diodes”. In: *Acs Photonics* **5.3** (2017), pp. 1084–1093.
- [55] T. Sugaya et al. “Ultra-high stacks of  $\text{InGaAs}/\text{GaAs}$  quantum dots for high efficiency solar cells”. In: *Energy & Environmental Science* **5.3** (2012), pp. 6233–6237.
- [56] Q. Xie et al. “Vertically self-organized  $\text{InAs}$  quantum box islands on  $\text{GaAs}$  (100)”. In: *Physical review letters* **75.13** (1995), p. 2542.
- [57] G. Springholz et al. “Self-organized growth of three-dimensional quantum-dot crystals with fcc-like stacking and a tunable lattice constant”. In: *Science* **282.5389** (1998), pp. 734–737.
- [58] M. Bayer et al. “Coupling and entangling of quantum states in quantum dot molecules”. In: *Science* **291.5503** (2001), pp. 451–453.
- [59] M. Korkusiński and P. Hawrylak. “Electronic structure of vertically stacked self-assembled quantum disks”. In: *Physical Review B* **63.19** (2001), p. 195311.
- [60] D. G. Austing et al. “Integer filling factor phases and isospin in vertical diatomic artificial molecules”. In: *Physical Review B* **70.4** (2004), p. 045324.
- [61] D. Loss and D. P. DiVincenzo. “Quantum computation with quantum dots”. In: *Physical Review A* **57.1** (1998), p. 120.
-

- 
- [62] R. J. Luyken et al. “Coulomb-coupling in vertically aligned self-assembled InAs quantum dots”. In: *Nanotechnology* **10.1** (1999), p. 14.
- [63] A. Chantre, G. Vincent, and D. Bois. “Deep-level optical spectroscopy in GaAs”. In: *Physical Review B* **23.10** (1981), p. 5335.
- [64] O. Maida, D. Kanemoto, and T. Hirose. “Characterization of deep interface states in SiO<sub>2</sub>/B-doped diamond using the transient photocapacitance method”. In: *Thin Solid Films* **741** (2022), p. 139026.
- [65] M. C. Chen et al. “Effects of leakage current on deep level transient spectroscopy”. In: *Applied physics letters* **44.8** (1984), pp. 790–792.
- [66] D. C. Cronemeyer. “Infrared absorption of reduced rutile TiO<sub>2</sub> single crystals”. In: *Physical review* **113.5** (1959), p. 1222.
- [67] I. Nakamura et al. “Role of oxygen vacancy in the plasma-treated TiO<sub>2</sub> photocatalyst with visible light activity for NO removal”. In: *Journal of Molecular Catalysis A: Chemical* **161.1-2** (2000), pp. 205–212.
- [68] X. Pan et al. “Defective TiO<sub>2</sub> with oxygen vacancies: synthesis, properties and photocatalytic applications”. In: *Nanoscale* **5.9** (2013), pp. 3601–3614.
- [69] C. C. Bof Bufon et al. “Self-assembled ultra-compact energy storage elements based on hybrid nanomembranes”. In: *Nano letters* **10.7** (2010), pp. 2506–2510.
- [70] O. G. Schmidt and K. Eberl. “Thin solid films roll up into nanotubes”. In: *Nature* **410.6825** (2001), pp. 168–168.
- [71] G. G. Stoney. “The tension of metallic films deposited by electrolysis”. In: *Proceedings of the Royal Society of London. Series A, Containing Papers of a Mathematical and Physical Character* **82.553** (1909), pp. 172–175.
- [72] V. Y. Prinz et al. “Free-standing and overgrown InGaAs/GaAs nanotubes, nanohelices and their arrays”. In: *Physica E: Low-dimensional Systems and Nanostructures* **6.1-4** (2000), pp. 828–831.
- [73] G. L. Pozzoli et al. “Charge transport and gradient doping in nanostructured polypyrrole films for applications in photocurrent generation”. In: *ACS Applied Nano Materials* **3.3** (2020), pp. 3060–3070.
- [74] S. M. Reimann and M. Manninen. “Electronic structure of quantum dots”. In: *Reviews of modern physics* **74.4** (2002), p. 1283.
- [75] T. Heinzl. *Mesoscopic electronics in solid state nanostructures*. John Wiley & Sons, 2008.
- [76] L. M. Maestro et al. “CdSe quantum dots for two-photon fluorescence thermal imaging”. In: *Nano letters* **10.12** (2010), pp. 5109–5115.
- [77] X. Xu et al. “Electrophoretic analysis and purification of fluorescent single-walled carbon nanotube fragments”. In: *Journal of the American Chemical Society* **126.40** (2004), pp. 12736–12737.
- [78] D. Bera et al. “Quantum dots and their multimodal applications: a review”. In: *Materials* **3.4** (2010), pp. 2260–2345.
-

- 
- [79] A. Bhati et al. “Sunlight-induced photocatalytic degradation of pollutant dye by highly fluorescent red-emitting Mg-N-embedded carbon dots”. In: *ACS Sustainable Chemistry & Engineering* **6.7** (2018), pp. 9246–9256.
- [80] S. Fasbender et al. “The low toxicity of graphene quantum dots is reflected by marginal gene expression changes of primary human hematopoietic stem cells”. In: *Scientific reports* **9.1** (2019), p. 12028.
- [81] M. Ciorga et al. “Addition spectrum of a lateral dot from Coulomb and spin-blockade spectroscopy”. In: *Physical Review B* **61.24** (2000), R16315.
- [82] J. M. Elzerman et al. “Single-shot read-out of an individual electron spin in a quantum dot”. In: *nature* **430.6998** (2004), pp. 431–435.
- [83] M. Pustilnik and L. Glazman. “Kondo effect in quantum dots”. In: *Journal of Physics: Condensed Matter* **16.16** (2004), R513.
- [84] S. G. J. Philips et al. “Universal control of a six-qubit quantum processor in silicon”. In: *Nature* **609.7929** (2022), pp. 919–924.
- [85] K. G. Günther. “Aufdampfschichten aus halbleitenden III-V-Verbindungen”. In: *Zeitschrift für Naturforschung A* **13.12** (1958), pp. 1081–1089.
- [86] K. E. Sautter, K. D. Vallejo, and P. J. Simmonds. “Strain-driven quantum dot self-assembly by molecular beam epitaxy”. In: *Journal of Applied Physics* **128.3** (2020).
- [87] F. C. Frank and J. H. van der Merwe. “One-dimensional dislocations. I. Static theory”. In: *Proceedings of the Royal Society of London. Series A. Mathematical and Physical Sciences* **198.1053** (1949), pp. 205–216.
- [88] M. Volmer and A. Weber. “Keimbildung in übersättigten Gebilden”. In: *Zeitschrift für physikalische Chemie* **119.1** (1926), pp. 277–301.
- [89] B. Junno et al. “A reflection high-energy electron diffraction and atomic force microscopy study of the chemical beam epitaxial growth of InAs and InP islands on (001) GaP”. In: *Applied physics letters* **72.8** (1998), pp. 954–956.
- [90] I. N. Stranski and L. Krastanow. “Zur Theorie der orientierten Ausscheidung von Ionenkristallen aufeinander”. In: *Monatshefte für Chemie und verwandte Teile anderer Wissenschaften* **71** (1937), pp. 351–364.
- [91] J. Stangl, V. Holý, and G. Bauer. “Structural properties of self-organized semiconductor nanostructures”. In: *Reviews of modern physics* **76.3** (2004), pp. 725–783.
- [92] N. Bart et al. “Wafer-scale epitaxial modulation of quantum dot density”. In: *Nature communications* **13.1** (2022), p. 1633.
- [93] B. D. Min et al. “Suppression of Ostwald ripening in  $\text{In}_{0.5}\text{Ga}_{0.5}\text{As}$  quantum dots on a vicinal (100) substrate”. In: *Physical Review B* **57.19** (1998), p. 11879.
- [94] W. Ostwald. “Studien über die Bildung und Umwandlung fester Körper: 1. Abhandlung : Übersättigung und Überkaltung”. In: *Zeitschrift für physikalische Chemie* **22.1** (1897), pp. 289–330.
-



- 
- [95] N. Moll, M. Scheffler, and E. Pehlke. “Influence of surface stress on the equilibrium shape of strained quantum dots”. In: *Physical Review B* **58.8** (1998), p. 4566.
- [96] G. Kim et al. “New approaches to produce large-area single crystal thin films”. In: *Advanced Materials* **35.4** (2023), p. 2203373.
- [97] W. Wu et al. “Atom-resolved scanning tunneling microscopy of vertically ordered InAs quantum dots”. In: *Applied physics letters* **71.8** (1997), pp. 1083–1085.
- [98] S. H. Xin et al. “Formation of self-assembling CdSe quantum dots on ZnSe by molecular beam epitaxy”. In: *Applied physics letters* **69.25** (1996), pp. 3884–3886.
- [99] K. L. Wang et al. “Ge/Si self-assembled quantum dots and their optoelectronic device applications”. In: *Proceedings of the IEEE* **95.9** (2007), pp. 1866–1883.
- [100] M. Pinczolits, G. Springholz, and G. Bauer. “Direct formation of self-assembled quantum dots under tensile strain by heteroepitaxy of PbSe on PbTe (111)”. In: *Applied physics letters* **73.2** (1998), pp. 250–252.
- [101] D. Leonard et al. “Structural and optical properties of self-assembled InGaAs quantum dots”. In: *Journal of Vacuum Science & Technology B: Microelectronics and Nanometer Structures Processing, Measurement, and Phenomena* **12.4** (1994), pp. 2516–2520.
- [102] A. Ludwig. “Elektrische Spininjektion in InAs-Quantenpunkte”. PhD thesis. Ruhr-Universität Bochum, Universitätsbibliothek, 2013.
- [103] V. Fock. “Bemerkung zur Quantelung des harmonischen Oszillators im Magnetfeld”. In: *Zeitschrift für Physik* **47.5** (1928), pp. 446–448.
- [104] C. G. Darwin. “The diamagnetism of the free electron”. In: *Mathematical Proceedings of the Cambridge Philosophical Society*. Vol. **27**. 1. Cambridge University Press. 1931, pp. 86–90.
- [105] O. Stier, M. Grundmann, and D. Bimberg. “Electronic and optical properties of strained quantum dots modeled by 8-band  $k \cdot p$  theory”. In: *Physical Review B* **59.8** (1999), p. 5688.
- [106] S. Schulz. “Kapazitäts- und Kapazitätstransientenspektroskopie an selbstorganisiert gewachsenen InAs-Quantenpunkten”. PhD thesis. Staats- und Universitätsbibliothek Hamburg Carl von Ossietzky, 2005.
- [107] L. Schnorr et al. “Laplace deep level transient spectroscopy on self-assembled quantum dots”. In: *Journal of Applied Physics* **124.10** (2018).
- [108] B. T. Miller et al. “Few-electron ground states of charge-tunable self-assembled quantum dots”. In: *Physical Review B* **56.11** (1997), p. 6764.
- [109] R. Seguin et al. “Size-dependent fine-structure splitting in self-organized InAs/GaAs quantum dots”. In: *Physical review letters* **95.25** (2005), p. 257402.
- [110] S. Tarucha et al. “Shell filling and spin effects in a few electron quantum dot”. In: *Physical Review Letters* **77.17** (1996), p. 3613.
-

- 
- [111] A. Patane et al. “Probing the quantum states of self-assembled InAs dots by magnetotunneling spectroscopy”. In: *Physical Review B* **65**.16 (2002), p. 165308.
- [112] R. J. D. Tilley. *Defects in solids*. John Wiley & Sons, 2008.
- [113] S. M. Sze. *Semiconductor devices: physics and technology*. John Wiley & Sons, 2008.
- [114] R. Sauer et al. “Dislocation-related photoluminescence in silicon”. In: *Applied Physics A* **36** (1985), pp. 1–13.
- [115] A. E. Chernyakov et al. “Nonradiative recombination dynamics in InGaN/GaN LED defect system”. In: *Superlattices and Microstructures* **45**.4-5 (2009), pp. 301–307.
- [116] S. Y. Karpov and Y. N. Makarov. “Dislocation effect on light emission efficiency in gallium nitride”. In: *Applied Physics Letters* **81**.25 (2002), pp. 4721–4723.
- [117] S. Pezzagna and J. Meijer. “Quantum computer based on color centers in diamond”. In: *Applied Physics Reviews* **8**.1 (2021).
- [118] L. Childress and R. Hanson. “Diamond NV centers for quantum computing and quantum networks”. In: *MRS bulletin* **38**.2 (2013), pp. 134–138.
- [119] K. W. Böer and U. W. Pohl. “Crystal Defects”. In: *Semiconductor Physics*. Springer, 2023, pp. 595–648.
- [120] J. C. Bourgoin, H. J. Von Bardeleben, and D. Stievenard. “Native defects in gallium arsenide”. In: *Journal of applied physics* **64**.9 (1988), R65–R92.
- [121] D. Pons and J. C. Bourgoin. “Irradiation-induced defects in GaAs”. In: *Journal of Physics C: Solid State Physics* **18**.20 (1985), p. 3839.
- [122] J. W. Farmer and D. C. Look. “Electron-irradiation defects in n-type GaAs”. In: *Physical Review B* **21**.8 (1980), p. 3389.
- [123] J. Bai and B. Zhou. “Titanium dioxide nanomaterials for sensor applications”. In: *Chemical reviews* **114**.19 (2014), pp. 10131–10176.
- [124] L. Schnorr et al. “Deep-level transient spectroscopy at platinum/titanium-dioxide hydrogen sensors”. In: *physica status solidi (b)* **253**.4 (2016), pp. 690–696.
- [125] S. Lany and A. Zunger. “Accurate prediction of defect properties in density functional supercell calculations”. In: *Modelling and simulation in materials science and engineering* **17**.8 (2009), p. 084002.
- [126] H. Seong and L. J. Lewis. “Tight-binding molecular-dynamics study of point defects in GaAs”. In: *Physical Review B* **52**.8 (1995), p. 5675.
- [127] E. Zielony et al. “Deep levels in the MBE ZnO: As/n-GaN diodes—Photoluminescence, electrical properties and deep level transient spectroscopy”. In: *Journal of Alloys and Compounds* **742** (2018), pp. 296–303.
- [128] D. B. Strukov et al. “The missing memristor found”. In: *nature* **453**.7191 (2008), pp. 80–83.
-

- 
- [129] A. Fujishima and K. Honda. “Electrochemical photolysis of water at a semiconductor electrode”. In: *nature* **238**.5358 (1972), pp. 37–38.
- [130] H. Sheng et al. “Activation of water in titanium dioxide photocatalysis by formation of surface hydrogen bonds: an in situ IR spectroscopy study”. In: *Angewandte Chemie International Edition* **54**.20 (2015), pp. 5905–5909.
- [131] J. Zhao et al. “The challenges and opportunities for TiO<sub>2</sub> nanostructures in gas sensing”. In: *ACS sensors* **9**.4 (2024), pp. 1644–1655.
- [132] Z. Li et al. “Resistive-type hydrogen gas sensor based on TiO<sub>2</sub>: A review”. In: *International Journal of Hydrogen Energy* **43**.45 (2018), pp. 21114–21132.
- [133] K. B. Chetry et al. “A comparison of the growth modes of (100)-and (110)-oriented CrO<sub>2</sub> films through the calculation of surface and interface energies”. In: *Journal of Applied Physics* **110**.11 (2011).
- [134] D. Kwon et al. “Atomic structure of conducting nanofilaments in TiO<sub>2</sub> resistive switching memory”. In: *Nature nanotechnology* **5**.2 (2010), pp. 148–153.
- [135] A. Sawa. “Resistive switching in transition metal oxides”. In: *Materials today* **11**.6 (2008), pp. 28–36.
- [136] M. K. Nowotny et al. “Defect chemistry of titanium dioxide. Application of defect engineering in processing of TiO<sub>2</sub>-based photocatalysts”. In: *The Journal of Physical Chemistry C* **112**.14 (2008), pp. 5275–5300.
- [137] G. Mattioli et al. “Ab initio study of the electronic states induced by oxygen vacancies in rutile and anatase TiO<sub>2</sub>”. In: *Physical Review B—Condensed Matter and Materials Physics* **78**.24 (2008), p. 241201.
- [138] T. S. Bjørheim, A. Kuwabara, and T. Norby. “Defect chemistry of rutile TiO<sub>2</sub> from first principles calculations”. In: *The Journal of Physical Chemistry C* **117**.11 (2013), pp. 5919–5930.
- [139] W. Shockley and W. T. Read. “Statistics of the recombinations of holes and electrons”. In: *Physical review* **87**.5 (1952), p. 835.
- [140] I. Magnúsdóttir et al. “One-and two-phonon capture processes in quantum dots”. In: *Journal of applied physics* **92**.10 (2002), pp. 5982–5990.
- [141] I. Magnúsdóttir et al. “Geometry dependence of Auger carrier capture rates into cone-shaped self-assembled quantum dots”. In: *Physical Review B* **67**.20 (2003), p. 205326.
- [142] P. Blood and J. W. Orton. “The electrical characterisation of semiconductors”. In: *Reports on Progress in Physics* **41**.2 (1978), p. 157.
- [143] A. R. Peaker, V. P. Markevich, and J. Coutinho. “Tutorial: Junction spectroscopy techniques and deep-level defects in semiconductors”. In: *Journal of Applied Physics* **123**.16 (2018).
- [144] J. Frenkel. “On pre-breakdown phenomena in insulators and electronic semiconductors”. In: *Physical Review* **54**.8 (1938), p. 647.
-

- 
- [145] E. N. Korol. “Ionization of impurity states in semiconductors by an electric field”. In: *Sov. Phys. Solid State* **19.8** (1977), p. 1327.
- [146] J. Smoliner. *Grundlagen der Halbleiterphysik*. Springer, 2018.
- [147] G. Vincent, A. Chantre, and D. Bois. “Electric field effect on the thermal emission of traps in semiconductor junctions”. In: *Journal of Applied Physics* **50.8** (1979), pp. 5484–5487.
- [148] D. Pons and S. Makram-Ebeid. “Phonon assisted tunnel emission of electrons from deep levels in GaAs”. In: *Journal de Physique* **40.12** (1979), pp. 1161–1172.
- [149] S. Makram-Ebeid and M. Lannoo. “Quantum model for phonon-assisted tunnel ionization of deep levels in a semiconductor”. In: *Physical Review B* **25.10** (1982), p. 6406.
- [150] G. Lucovsky. “On the photoionization of deep impurity centers in semiconductors”. In: *Solid State Communications* **3.9** (1965), pp. 299–302.
- [151] M. Jaros. “Wave functions and optical cross sections associated with deep centers in semiconductors”. In: *Physical Review B* **16.8** (1977), p. 3694.
- [152] A. Franceschetti and S. T. Pantelides. “Excited-state relaxations and Franck-Condon shift in Si quantum dots”. In: *Physical Review B* **68.3** (2003), p. 033313.
- [153] L. Lugani et al. “Photocapacitance spectroscopy of InAlN nearly lattice-matched to GaN”. In: *Applied Physics Letters* **109.15** (2016).
- [154] P. Lochner et al. “Internal photoeffect from a single quantum emitter”. In: *Physical Review B* **103.7** (2021), p. 075426.
- [155] A. Kurzmann et al. “Photoelectron generation and capture in the resonance fluorescence of a quantum dot”. In: *Applied Physics Letters* **108.26** (2016).
- [156] W. Schottky. “Vereinfachte und erweiterte Theorie der Randschicht-gleichrichter”. In: *Zeitschrift für Physik* **118.9** (1942), pp. 539–592.
- [157] G. Myburg et al. “Summary of Schottky barrier height data on epitaxially grown n-and p-GaAs”. In: *Thin solid films* **325.1-2** (1998), pp. 181–186.
- [158] G. Margaritondo. “Interface states at semiconductor junctions”. In: *Reports on Progress in Physics* **62.5** (1999), p. 765.
- [159] J. Bardeen. “Surface states and rectification at a metal semi-conductor contact”. In: *Physical review* **71.10** (1947), p. 717.
- [160] R. T. Tung. “Recent advances in Schottky barrier concepts”. In: *Materials Science and Engineering: R: Reports* **35.1-3** (2001), pp. 1–138.
- [161] G. Snider. “1D Poisson-Schrödinger solver”. In: (2017). [Accessed on Sep 15<sup>th</sup>, 2017]. URL: <https://www3.nd.edu/~gsnider/>.
- [162] C. R. Crowell and S. M. Sze. “Current transport in metal-semiconductor barriers”. In: *Solid-state electronics* **9.11-12** (1966), pp. 1035–1048.
- [163] F. A. Padovani and R. Stratton. “Field and thermionic-field emission in Schottky barriers”. In: *Solid-State Electronics* **9.7** (1966), pp. 695–707.
-

- 
- [164] R. Williams. “Determination of deep centers in conducting gallium arsenide”. In: *Journal of Applied Physics* **37.9** (1966), pp. 3411–3416.
- [165] Zurich Instruments. *HF2 User Manual*. [Accessed on Jun 30<sup>th</sup>, 2024]. URL: [https://docs.zhinst.com/pdf/ziHF2\\_UserManual.pdf](https://docs.zhinst.com/pdf/ziHF2_UserManual.pdf).
- [166] L. Schnorr. “Electron capture and emission dynamics of self-assembled quantum dots”. PhD thesis. Düsseldorf, Heinrich-Heine-Universität, 2022.
- [167] Y. Chen et al. “Recent progress on optoplasmonic whispering-gallery-mode microcavities”. In: *Advanced Optical Materials* **9.12** (2021), p. 2100143.
- [168] L. Mercas et al. “Reorganization Energy upon Controlled Intermolecular Charge-Transfer Reactions in Monolithically Integrated Nanodevices”. In: *Small* **17.45** (2021), p. 2103897.
- [169] C. V. S. Batista et al. “High-Performance Ultrathin Molecular Rectifying Diodes Based on Organic/Inorganic Interface Engineering”. In: *Advanced Functional Materials* **32.6** (2022), p. 2108478.
- [170] M. El Achhab and K. Schierbaum. “Gas sensors based on plasma-electrochemically oxidized titanium foils”. In: *Journal of sensors and sensor systems* **5.2** (2016), pp. 273–281.
- [171] K. H. Nicholas and J. Woods. “The evaluation of electron trapping parameters from conductivity glow curves in cadmium sulphide”. In: *British Journal of Applied Physics* **15.7** (1964), p. 783.
- [172] G. L. Miller, D. V. Lang, and L. C. Kimerling. “Capacitance transient spectroscopy”. In: *Annual Review of Materials Science* **7.1** (1977), pp. 377–448.
- [173] J. H. Warner et al. “A Deep Level Transient Spectroscopy Study of Electron and Proton Irradiated p<sup>+</sup>n GaAs Diodes”. In: *IEEE Transactions on Nuclear Science* **57.4** (2010), pp. 1940–1945.
- [174] M. Gonzalez et al. “Deep level defects in proton radiated GaAs grown on metamorphic SiGe/Si substrates”. In: *Journal of applied physics* **100.3** (2006).
- [175] C. Liu et al. “DLTS studies of bias dependence of defects in silicon NPN bipolar junction transistor irradiated by heavy ions”. In: *Nuclear Instruments and Methods in Physics Research Section A: Accelerators, Spectrometers, Detectors and Associated Equipment* **688** (2012), pp. 7–10.
- [176] Z. Wang et al. “Comprehensive characterization of efficiency limiting defects in the swirl-shaped region of Czochralski silicon”. In: *Solar Energy Materials and Solar Cells* **236** (2022), p. 111533.
- [177] Z. Zhang et al. “Deep level defects throughout the bandgap of (010)  $\beta$ -Ga<sub>2</sub>O<sub>3</sub> detected by optically and thermally stimulated defect spectroscopy”. In: *Applied Physics Letters* **108.5** (2016).
- [178] T. Nowozin et al. “800 meV localization energy in GaSb/GaAs/Al<sub>0.3</sub>Ga<sub>0.7</sub>As quantum dots”. In: *Applied Physics Letters* **102.5** (2013).
- [179] G. L. Miller, J. V. Ramirez, and D. A. H. Robinson. “A correlation method for semiconductor transient signal measurements”. In: *Journal of Applied Physics* **46.6** (1975), pp. 2638–2644.
-

- [180] D. S. Day et al. “Deep-level-transient spectroscopy: System effects and data analysis”. In: *Journal of Applied Physics* **50.8** (1979), pp. 5093–5098.
-

---

# Danksagung

Ich möchte mich bei allen bedanken, die mich während dieser Arbeit unterstützt haben.

Meinem Doktorvater Prof. Dr. Thomas Heinzl danke ich für die Möglichkeit in seiner Gruppe meine Doktorarbeit anfertigen zu können. Ich konnte stets auf Unterstützung für meine Anliegen sowie auf Freiräume für wissenschaftliche Kreativität zählen. Besonders dankbar bin ich für die Teilnahme an der APS-Konferenz in Las Vegas, einer unglaublich wertvollen Erfahrung.

Prof. Dr. Andreas Wieck und Dr. Arne Ludwig und ihrer gesamten Arbeitsgruppe von der Ruhr-Universität Bochum danke ich für die SAQDs Proben, die Sie für uns gewachsen haben sowie die ertragreichen Diskussionen zu den Projekten.

I would like to thank Prof. Dr. Carlos Cesar Bof Bufon and Dr. Leandro Mercês for the rolled-up nanomembrane samples, which they prepared during their time at the Brazilian Nanotechnology National Laboratory at the Brazilian Center for Research in Energy and Materials in Campinas in Brazil.

Ich danke Prof. Dr. Egger für die Mentorenschaft und Prof. Dr. Horbach für die Übernahme des Korreferats.

Bianka Lindenau danke ich für die zuverlässige Organisation aller administrativen Aufgaben.

Unserem Techniker Uwe für die Unterstützung bei den mechanischen Herausforderungen und für den Transport der zahlreichen Flüssigstickstoffkannen.

Der gesamten Arbeitsgruppe vom Lehrstuhl für Festkörperphysik danke ich für die immer sehr gute Atmosphäre, in der ich mich stets sehr wohl gefühlt habe. Der Kuchen war immer lecker. Ich danke meinen (ehemaligen) Kollegen Beate, Stefan, Jakob, Christian, Svenja, Cathrin, Carla und Frederick. Ein besonderer Dank gilt meinem Vorgänger an diesem Projekt, Laurin. Er hat mit seinen Ideen, Basteleien und Computerprogrammen sehr wahrscheinlich nicht nur mir sondern der ganzen Arbeitsgruppe geholfen. Während meiner Zeit als Master- und später als Promotionsstudent konnte ich mich immer auf sein Fachwissen verlassen. Special thanks to Mihai for introducing me to sample preparation and cryostats.

Herzlichen Dank auch an Jenny, Haris, Daniela, Ouafaa, Julia und Max, die ich während ihren Bachelor- oder Masterarbeiten betreuen durfte.

Vielen Dank an alle die meine Arbeit Korrektur gelesen haben!

---

Großer Dank geht an das Schwimmteam der Uni Düsseldorf dem ich während meiner Bachelor,- Master- und Promotionszeit angehört habe, die kühlen Trainingseinheiten und die spaßigen Wettkämpfe waren ein sehr guter Ausgleich. Großer Dank geht ebenfalls an die Katze Polly de Pollença für die große Unterstützung sowie die geteilten Dosen Thunfisch. Dem Jugendblasorchester der Clara-Schuhmann Musikschule danke ich ebenso für die vielen Konzerte an denen ich teilnehmen durfte.

Meinen Eltern und meiner Schwester danke ich für die Unterstützung. Meiner Schwester für die vielen Korrekturlesungen. Meiner Mutter danke ich, dass sie mir schon in frühen Jahren Sach- und Physikbücher nahe gebracht hat. Meinem Vater danke ich dafür, dass er mich für Bausets aus Lego, Magnetstäben oder Holz gefördert hat. Bei mathematischen aber auch bei sprachlichen Fragen konnte ich immer auf seine Hilfe zählen.

Zuletzt möchte ich mich besonders bei meiner Partnerin Joline bedanken, die mich über die gesamte Zeit meiner Promotion liebevoll unterstützt hat.

---